UNIVERSITÀ DI PARMA

UNIVERSITÀ DEGLI STUDI DI PARMA

Dottorato di ricerca in Fisica

Ciclo XXXIII

Gravitational wave signature of binary neutron star mergers

Coordinatore: Chiar.mo Prof. Stefano Carretta

Tutor: Chiar.mo Prof. Roberto De Pietri

Dottorando: Michele Pasquali

Anni Accademici 2017/2018 - 2019/2020

alle mie insicurezze

Abstract

This work is focused on the analysis of the gravitational-waves emitted by binary neutron star systems when they merge to form either a black hole or a remnant neutron star which will eventually collapse to a black hole in a delayed time. This research is based on the use of general relativistic numerical simulations that represent the only tool available to study the evolution of binary neutron star systems through all the phases of their dynamics from the coalescence to the merger and eventually the post-merger.

In particular, the effect of the equation of state, the total mass of the system and the mass ratio on the post-merger phase of the gravitational-waves signal has been analysed, evaluating the properties when the system lives long enough after the merger. The focus of this research is on binary neutron star systems which form a (hyper-)massive remnant after the merger that lives long enough (at least 5 ms) and eventually collapse to a black hole. The spectral features of the gravitational-wave signal in the post-merger phase have been deeply investigated and compared to the literature also using publicly available data from other groups.

Emphasis has been given to the models that have a longer post-merger phase where additional inertial modes may appear due to the presence of instabilities in the remnant depending on the equation of state of the neutron stars. For that purpose, different techniques of time-frequency analysis have been used in order to study the peculiarities of the gravitational wave signal during this phase of the evolution.

The main interest for this research comes from the fact that binary neutron star mergers are an important target for Earth-based interferometric detectors such as LIGO, Virgo and KAGRA. The detection of GW170817 and its electromagnetic counterpart has been widely recognised as the beginning of multimessenger astrophysics, providing key evidence to long-standing issues in relativistic astrophysics and adding stronger constraints on neutron stars parameters. Complementary information on the internal structure of neutron stars can be obtained through the observation of the post-merger GW signal, which is still an open problem in multimessenger astrophysics. For that purpose, numerical simulations of binary neutron star mergers are an essential tool in the recognition process of GW signal in the detectors.

This work has been performed only using publicly available codes such as `LORENE` for the initial data setup and the `Einstein Toolkit` for the system evolution in order to make all the results presented here reproducible.

Contents

Chapter 1

Introduction

The first direct detection of the merger of a binary black hole (BBH) system by the Advanced LIGO interferometers [1, 2] represented the start of the gravitational wave (GW) astronomy. The observations of BBH mergers that followed GW150914 until the very last reported in [3] (see reference therein for further information about the O3 run) were the natural consequence of the improvement of such instruments, which also led to the first direct detection of a binary neutron star (BNS) merger in GW170817 [4].

The first direct detection of a binary neutron star (BNS) merger in August 2017 represented a turning point in gravitational wave astrophysics, since BBHs had been the only source detected until that point, since the detection rate for such events at LIGO/Virgo design sensitivity was $0.2 - 200$ detection/year [5]. The joint detection of gravitational waves (GW) and the electromagnetic counterpart from the binary neutron star event GW170817 / GRB 170817A / AT 2017gfo is generally regarded as the start of multimessenger astrophysics (see [4] and references therein). This unique event has given the indication to address enduring issues in relativistic astrophysics such as the nature of gamma-ray bursts and kilonovae (KN), and the $r-$process mediated nucleosynthesis of heavy elements [6, 7, 8, 9]. Constraints on masses, radii, spins and the equation of state (EOS) has been derived from the GW signal in the inspiral phase in [10], and such information has been later improved in [11, 12]. These constraints are based on the analysis of the tidal interactions between the two stars during their inspiral. The post-merger GW signal is expected to be able to give complementary information on the internal structure of neutron stars through the application of an empirical relation between the $m = 2$ $f-$mode frequency and the neutron star radius (see [13, 14] and reference therein).

A reliable way of building theoretical models of post-merger GW emission is through nonlinear, general relativistic numerical simulations. A typical outcome of such numerical simulations of binary neutron star mergers shows that the model of the gravitational wave signal depends on the component masses and the EOS (see [15, 16, 17, 18] for reviews). If the initial masses of the two stars are sufficiently large, the system may promptly collapse to black hole, while a delayed collapse or even no collapse is produced otherwise, forming either a hypermassive neutron star (HMNS) [19] or a supramassive neutron star [20]. In order to investigate these systems, numerical simulations of such systems can be performed using numerical relativity codes, such as the `LORENE` library [21, 22] and the `Einstein Toolkit` [23], which were used in this thesis respectively for the generation of initial data and the time evolution of the system. These codes are publicly available and open source, which is an important feature for the reproducibility of the results and the fact that they can be enhanced by any contributors, which is what I did for some part of the code that was necessary for my project.

The GW signals originated by post-merger remnants are identified by high frequencies that are much more difficult to be detected by the current generation interferometers, such as the Advanced LIGO [24] and Virgo [25], than those produced during the inspiral, as the (quantum) shot-noise limits the sensitivity of the instruments above a few kHz. It is not surprising that the recent searches by the LIGO/Virgo collaboration have not revealed any sign of GWs from the post-merger remnant [26, 12, 27]. However, for events similar to GW170817 in terms of distance and amplitude, the GW signal seems to be within reach for future observing runs at higher sensitivity and the next generation of detectors.

Numerical simulations of the post-merger phase of BNS systems that end up forming a HMNS show the emission of a large amount of GWs at frequencies of a few kHz(e.g. [28, 29, 30, 31, 32, 33, 34]) with some contribution even at ~ 1 kHz, depending on the equation of state [14]. These simulations lasts up to a few tens of ms after the merger, which is long enough to observe that the GW emission is dominated by a main peak in the frequency range $\sim 2-4$ kHz, with secondary peaks on both sides of the main peak. It was found in [29], using a mode analysis technique, that the main post-merger peak is due to the excitation of the fundamental $m = 2$ $f-$mode. It is also shown that some combination of frequencies are present in models that are relatively close to threshold mass to collapse (high-mass/soft EOS models) [32]. Also, the spiral deformation of the remnant in the first moments after the merger can excite additional modes that are commonly called f_{spiral}.

This thesis has the following structure: the first chapter is an introduction to the neutron star physics, the equation of state of neutron stars and how it is treated numerically in the piecewise polytropic approximation. The second chapter is a review of the state-of-the-art of the numerical methods employed to solve Einstein's equations and the general relativistic hydrodynamics, as implemented by the `Einstein Toolkit`. This chapter is closed with a short description of the computational method adopted to extract the GW signal from BNS simulations, which is also presented in a more detailed way in [35]. The third chapter contains the analysis of the results that can be extracted by the BNS simulations of the relativity group of the University of Parma also presented in [36, 37, 38]. A particular focus has been put on the time-frequency analysis of the gravitational wave signal, which is mainly discussed in section 4.2.2, 4.2.3 and 4.2.4. In particular, in the second one, the continuous wavelet transform (CWT) [39] is proposed as a new method to perform time-frequency analysis of the GW signal of BNS. In the latter, this method is used to perform the analysis of the database of numerical simulations of BNS systems performed by the Parma group and an overview of all the features of the gravitational wave signal of such systems is presented.

All computations have been done in geometrical units (hereafter denoted as CU) in which $c = G = M_\odot = 1$, except where it is explicitly otherwise stated.

Chapter 2

Physical background: gravitational waves from binary neutron star systems

2.1 The physics of neutron stars

With the definition "neutron star" we usually refer to a star with mass M on the order of 1.5 solar masses ($M_\odot$), a radius of ~ 12 km and a central density which is 3 to 10 times the nuclear equilibrium density $n_0 = 0.16$ fm^{-3} [40]. The interior of neutron stars is, as suggested by the name, neutron-rich but a fraction of protons (and the corresponding quantity of electrons and/or muons to neutralize the matter) is still present, while the external layer, called "crust", can be formed by more complex nuclei, as well as other states like mesons, hyperons [41], and deconfined quarks [42] could be present in the inner core, when densities are above n_0.

Neutron stars are among the most dense objects that can be found in the universe. The strong gravitational field that holds together the matter of this kind of astrophysical bodies has to be treated taking into considerations general relativistic effects: a typical neutron star with mass 1.4 $M_\odot$and radius 10 km has 2.4 times the Schwarzschild radius of a non-rotating black hole with the same mass. Oppenheimer, Volkov [43] and Tolman [44] proved that the strong gravitational field of such objects cannot be compensated by the Fermi pressure of the free neutron gas since this would lead to a maximum mass of 0.7 $M_\odot$, while the sustain against gravitational collapse is given by the repulsive nuclear forces [45].

Neutron stars are formed in the aftermath of the gravitational collapse of the core of massive stars ($> 8\ M_\odot$and $< 25\ M_\odot$) at the end of their life. This generates the explosion of a type II supernovae, whose mechanism is still not completely understood [46] even if it is probable that neutrinos play an important role in this process. In effect, the gravitational binding energy released by the core-collapse of the progenitor star's dwarf-like core to a neutron star is about $\sim 3 \times 10^{53}$ erg, which is approximately 10% of its total mass energy. The expanding remnant has a kinetic energy of the order of 1×10^{51} up to 2×10^{51} erg, and the total energy radiated in photons is further reduced by a factor 100. This means that nearly all the energy is carried off by neutrinos and antineutrinos of all flavors.

When the inner density of the star reaches the nuclear equilibrium density value n_0, the stellar matter bounces back, forming a shock wave at the core's outer edge that travels for only 100 up to 200 km before stalling. The mechanism responsible for the reviving of the shock front is still not fully understood, however apparently, it is due to the neutrinos from the inner core that expel the stellar mantle assisted by rotation, convection and magnetic fields [47, 48, 49, 50, 51]. This process leaves a proto-neutron star remnant that, in the first ~ 10 ms, rapidly shrinks because of pressure losses from neutrino emission and, in some case, oscillational modes can be excited and cause the emission of gravitational waves [52, 53, 54, 55]. The neutrino emission is linked with electron captures, which deleptonize the star, becoming neutron-rich. The following phase is called "Kelvin-Helmholtz" phase: the proto-neutron star evolves in a quasi-stationary manner shrinking, cooling down, slowing down its rotation and becoming transparent to neutrinos [56, 57]. The collapse of the progenitor star causes the magnetic field to increase by several order of magnitude, mainly due to flux conservation, but also due to the winding linked with the star differential rotation. The magnetic field of regular neutron stars reaches values around $10^5 - 10^8$ Gauss. There is a special class of neutron stars, called "magnetars", where the magnetic field can reach values up to 10^{15} Gauss. The process linked to the formation of magnetars is still unknown, but it is believed to be related with magnetic instabilities which develop in the proto-neutron star after the stellar bounce [51].

The non-rotating equilibrium configuration of a neutron star is computed starting from the metric of a stationary, spherically symmetric space-time

$$\mathrm{d}s^2 = c^2 \mathrm{d}t^2 \mathrm{e}^{2\Phi} - \mathrm{e}^{2\lambda} \mathrm{d}r^2 - r^2 \left(\mathrm{d}\theta^2 + \sin^2\theta \mathrm{d}\phi^2 \right) \tag{2.1}$$

where t is the time-like coordinate, r the radial coordinate, θ and ϕ are the polar and azimuthal angles, respectively, whereas $\Phi = \Phi(r)$ and $\lambda = \lambda(r)$ are some functions of r, which are also defined in Chapter 6 of [58]. Solving the Einstein equations

$$R_{\mu\nu} - \frac{1}{2} g_{\mu\nu} R = \frac{8\pi G}{c^4} T_{\mu\nu} \tag{2.2}$$

where $R_{\mu\nu}$ is the Ricci curvature tensor, $R = R_\mu{}^\mu$ is the scalar curvature and $T_{\mu\nu}$ is the stress-energy tensor, one comes to the relativistic equations of hydrostatic equilibrium for a spherically symmetric neutron star

$$\frac{\mathrm{d}P}{\mathrm{d}r} = -\frac{G\rho m}{r^2}\left(1+\frac{P}{\rho c^2}\right)\left(1+\frac{4\pi P r^3}{mc^2}\right)\left(1-\frac{2Gm}{c^2 r}\right)^{-1}, \tag{2.3}$$

$$\frac{\mathrm{d}m}{\mathrm{d}r} = 4\pi r^2 \rho, \tag{2.4}$$

$$\frac{\mathrm{d}\Phi}{\mathrm{d}r} = -\frac{1}{\rho c^2}\frac{\mathrm{d}P}{\mathrm{d}r}\left(1+\frac{P}{\rho c^2}\right)^{-1}. \tag{2.5}$$

Equation (2.3) is called the Tolman-Oppenheimer-Volkov equation of hydrostatic equilibrium, equation (2.4) describes the mass balance, whereas equation (2.5) is a relativistic equation for the metric function described in (2.1). These equations should be supplemented by an equation of state (EOS), $P = P(\rho)$, in order to make equations (2.3), (2.4) and (2.5) a closed system of equations to be solved for $P(r)$, $\rho(r)$, $m(r)$ and $\Phi(r)$.

The conditions that allow equations (2.3)- (2.5) to be solved are that the pressure has to be positive, continuous and monotonically decreasing from the stellar center to the surface. In addition, one can introduce the equations for the number of baryons confined within a sphere of radius r as

$$\frac{\mathrm{d}a_b}{\mathrm{d}r} = \frac{4\pi r^2 n_b}{\sqrt{1-2Gm/(rc^2)}}, \tag{2.6}$$

where n_b is the baryon number density measured in a local reference frame. The set of equations (2.3)-(2.4) and (2.6) are usually integrated from the stellar center with the boundary conditions $P(0) = P_c$, $m(0) = 0$ and $a_b(0) = 0$. At the stellar surface $P(R) = 0$, so the presence of a thin atmosphere is usually neglected.

2.2 The equation of state of neutron stars

In the previous section it was mentioned that in order to solve the equations for hydrostatic equilibrium (see equations (2.3)- (2.5) and (2.6)) for a single, non-rotating neutron star, it is necessary to provide the equation of state (EOS) $P = P(\rho)$.

The first approximation is the one considering an EOS of cold matter in beta equilibrium, which is suitable to represent neutron stars at the end of the cooling process described in section 2.1. This is also the condition of neutron stars at the beginning of the merger simulation and during all the coalescence. EOS models can be developed employing different techniques, but in this section I will focus only on the models considered in chapter 4.

The equation of state model should be able to represent the nuclear matter in a very large density region, from the crust, whose density ρ is typically below the nuclear equilibrium density ρ_0 and the matter is composed only by neutrons, protons, electrons and simple atomic nuclei, up to the inner core, where ρ can even be bigger than $4\rho_0$ and non-nucleonic degrees of freedom can be present, such as hyperons, meson, condensates or deconfined quarks. Unfortunately, the exact calculation of the EOS, even for the crust case is not feasible due to the complexity of the many-body problem of heavy nuclei immersed in a neutron gas, as for the NS crust. For this reason, one common approach is that of using an effective hamiltonian in a mean-field scheme in order to include the effective two and three nucleon interactions. The large number of free parameters that is allowed by this approach is then fixed by fitting atomic nuclei properties measurements and the results of nucleon-nucleon scattering experiments, and extrapolated to higher densities, as in the interior of NSs.

In this work, we take into consideration five different EOS, namely **SLy** [59, 60], **APR4** [61], **H4** [41], **MS1** [62] and **SFHo** [63]. A brief review of the main properties and methods of the SLy, APR4, H4 and MS1 EOS can be found in [35] and in [64, 65, 66, 67, 36, 38] all four models have been used for numerical simulations of binary neutron star mergers. The SFHo EOS is based on the same relativistic mean field approach that has been applied to the H4 and MS1 ones, where a Lagrangian is build to describe the strong nuclear interactions as mesons exchange (scalar σ, vector ω, isovector ρ). The parameterization used for this EOS is that of [68] which is based on 17 parameters, one for the scalar-isoscalar meson, 6 for the standard non-linear Walecka couplings, two for the fourth-order vector meson couplings and 9 for the control of symmetry energy as a function of density. This model is built in order to fulfill all the observational constraints, in particular the fact that the maximum mass has to be larger than 1.93 $M_\odot$ [69], and the constraints of the matter near and below the saturation density (see [70, 71, 72, 73, 74, 75, 76, 77] for the details).

2.2.1 Piecewise polytropic approximation for BNS EOS

For numerical simulations of binary neutron star systems, it is a common choice to parametrize the EOS as a piecewise polytrope, following the work of [78]. This was also done by the Parma group in previous works (see [64, 65, 66, 67]) and discussed in the appendix C of [38]. The ideal fluid approximation for the thermal treatment of BNSs is also commonly used in numerical relativity. The energy momentum tensor is written as

$$T^{\mu\nu} = [\rho(1+\epsilon) + p]\, u^\mu u^\nu + p g^{\mu\nu} \tag{2.7}$$

where ρ is the baryon density, ϵ is the specific internal energy and p is the pressure and the energy density is given by

$$e = \rho(1+\epsilon)\,. \tag{2.8}$$

Using the ideal fluid approximation, we parametrized the SLy, APR4, H4 and MS1 EOS as seven-pieces piecewise polytropes, while for the SFHo EOS we used ten pieces, as described in [37]. The thermal treatment of the system is then described as:

$$\epsilon = \epsilon_{cold}(\rho) + \epsilon_{th} \tag{2.9}$$
$$p = p_{cold}(\rho) + (\Gamma_{th} - 1)\,\rho\epsilon_{th}, \tag{2.10}$$

where ϵ_{th} is an arbitrary function of the thermodynamical state that has the property of being zero at zero temperature. For a fixed number of fermions the volume (V) is defined as $V = (1/\rho)$ and the energy $E = e/\rho$, so that the first law of thermodynamics is:

$$\mathrm{d}Q = \mathrm{d}E + p\mathrm{d}V = T\mathrm{d}S. \tag{2.11}$$

If one assumes the thermodynamic consistency of Eq. (2.11), Frobenius theorem uniquely fixes the "temperature"-like and "entropy"-like functions, up to an arbitrary function $\Sigma(s)$ that gives other possible definition of "temperature" and "entropy" as $S = \Sigma(s)$ and $T = t/\left(\mathrm{d}\Sigma(s)/\mathrm{d}s\right)$. These functions are defined as:

$$T = (\Gamma_{th} - 1)\,\epsilon_{th}, \tag{2.12}$$
$$S = \log\left[\frac{(\epsilon_{th})^{1/(\Gamma_{th}-1)}}{\alpha\rho}\right], \tag{2.13}$$

where α is an arbitrary constant with the dimensions of the inverse of density. In order to convert the dimensionless "temperature"-like values ϵ_{th} and the real temperature T one has to consider the specific heat at constant volume and the function $\Sigma(s)$ as conversion factors. Choosing $\Sigma(s) = s$ corresponds to having the thermal behavior of an "ideal fluid", as also discussed in [79], and the dimension of the temperature T can be found by multiplying Eq. (2.12) by m/k_B, where m is the value of the baryon mass. The condition of thermodynamics consistency at $T = 0$ ($\mathrm{d}Q = 0$) determines the relation between $\epsilon_{cold}(\rho)$ and $p_{cold}(\rho)$, that reads

$$p_{cold}(\rho) = \rho^2 \frac{\mathrm{d}\epsilon_{cold}(\rho)}{\mathrm{d}\rho}. \tag{2.14}$$

The cold treatment (or zero-temperature) of the piecewise polytropic approximate EOS is then equivalent to the assumption that $p_{cold}(\rho)$ and $\epsilon_{cold}(\rho)$ are continuous polytropic functions of ρ. Therefore, locally, Eq. (2.14) and these conditions imply that for each piece of this approximation corresponds to a density interval $[\rho_i, \rho_{i+1}]$, so the pressure p and the specific energy density ϵ of a cold neutron star in beta equilibrium can be written as

$$p_{cold} = K_i \rho^{\Gamma_i} \tag{2.15}$$
$$\epsilon_{cold} = \epsilon_i + \frac{K_i}{\Gamma_i - 1}\rho^{\Gamma_i - 1}, \tag{2.16}$$

where K_i and Γ_i are the coefficients of the polytrope for the $i-$th piece. Once the set of polytropic indices Γ_i ($i = 0, ..., N-1$), the transition densities ρ_i ($i = 1, ..., N-1$) and K_0 are chosen, the N-piece piecewise polytropic EOS (with an "ideal fluid" thermal component) is defined. The parameters of the polytropic approximation of the five EOS considered in this work are summed up in Table 2.1, 2.3 and 2.2.

i	$\rho\ [g/cm^3]$	K_i	Γ_i
0	-	4.650×10^{-9}	1.584
1	2.440×10^{7}	5.706×10^{-6}	1.287
2	3.784×10^{11}	7.736×10^{-2}	0.622
3	2.628×10^{12}	8.758×10^{-6}	1.357

Table 2.1: Parameters of the low density part of the piecewise polytrope for SLy, APR4, H4 and MS1 EOS. This choice corresponds to the widely accepted SLy EOS modelling for the NS crust of [80], which is described by the Compressible Liquid Drop model. The parameterization is also in agreement with the one in [78]. The values of ρ_i and K_i are expressed in cgs units. Note that the units of K_i depends on Γ_i so they are not directly comparable in magnitude.

EOS	Γ_4	Γ_5	Γ_6	$\rho_4\ [g/cm^3]$
SLy	3.005	2.988	2.851	1.462×10^{14}
APR4	2.830	3.445	3.348	1.512×10^{14}
H4	2.909	2.246	2.144	0.888×10^{14}
MS1	3.224	3.003	1.325	0.942×10^{14}

Table 2.2: Parameters of the high density part of the piecewise polytrope for the all the EOS. ρ_4 is the density threshold between the crust (low-density) and the inner core (high density), which is chosen in order to match the two regions of the NS according to the different models of the EOS.

The specific enthalpy for a piecewise polytropic EOS becomes

$$\begin{aligned} h &= \frac{e+p}{\rho} = \frac{(1+\epsilon)\rho + p}{\rho} \\ &= 1 + (1-\Gamma_i)\epsilon_i + \Gamma_{th}\epsilon_{th} + \Gamma_i \epsilon_{cold}(\rho) \end{aligned} \tag{2.17}$$

and the relativistic speed of sound, which can be computed as

$$\begin{aligned} c_s^2 &= \frac{1}{h}\left(\frac{\mathrm{d}p}{\mathrm{d}\rho}\right)_s = \frac{1}{h}\left[\left(\frac{\partial p}{\partial \rho}\right)_\epsilon + \frac{\mathrm{d}\epsilon}{\mathrm{d}\rho}\left(\frac{\partial p}{\partial \epsilon}\right)_\rho\right] \\ &= \frac{1}{h}\left[\left(\frac{\partial p}{\partial \rho}\right)_\epsilon + \frac{p}{\rho^2}\left(\frac{\partial p}{\partial \epsilon}\right)_\rho\right], \end{aligned} \tag{2.18}$$

i	ρ $[g/cm^3]$	Γ_i
0	-	1.377
1	1.235×10^9	1.256
2	4.324×10^{11}	0.602
3	4.632×10^{12}	1.547
4	1.235×10^{14}	2.621
5	4.324×10^{14}	3.279
6	7.101×10^{14}	2.916
7	1.048×10^{15}	2.655
8	1.668×10^{15}	2.513
9	3.334×10^{15}	1.502

Table 2.3: Parameters of the piecewise polytrope for the SFHo EOS. The values of ρ_i are expressed in cgs units as in Table 2.1

takes the following form in the case of a piecewise polytropic EOS:

$$c_s^2 = \frac{\Gamma_{th}(\Gamma_{th}-1)\epsilon_{th} + \Gamma_i(\Gamma_i-1)(\epsilon_{cold}(\rho)-\epsilon_i)}{1+(1-\Gamma_i)\epsilon_i + \Gamma_{th}\epsilon_{th} + \Gamma_i\epsilon_{cold}(\rho)}. \tag{2.19}$$

Note that we imposed the condition that the pressure and energy density are continuous at the transition point, but that is not true in the case of the computation of the speed of sound, which, in general, can be discontinuous: $(c_s^2)_i(\rho_i) \neq (c_s^2)_{i+1}(\rho_i)$.

The adiabatic index (Γ_1) for adiabatic perturbations in a piecewise polytropic EOS becomes:

$$\begin{aligned} \Gamma_1 &= \frac{e+p}{p}\left(\frac{\mathrm{d}p}{\mathrm{d}e}\right)_s = \left(\frac{\mathrm{d}\ln p}{\mathrm{d}\ln\rho}\right)_s \\ &= \Gamma_{th} + (\Gamma_i - \Gamma_{th})\,\frac{K_i\rho^{\Gamma_i}}{p} \end{aligned} \tag{2.20}$$

where ϵ is the specific internal energy, K_i and Γ_i are the constant and the exponent in the i-th piece of the polytropic approximation of the EOS.

In [81] the same construction presented in this section, has been considered as a 2D equation of state. Their choice is that of assuming as the "entropy" the quantity s defined by $S = \Sigma(s) = 2/(\Gamma_{th}-1)\log(s)$ and fix the value of the constant α that was mentioned in Eq. (2.13) in order that $\epsilon_{th} \propto s^2\rho^{\Gamma_{th}-1}$. This choice may lead to convective instabilities for non-barotropic stellar configurations, which include binary neutron star merger remnants.

Another possibility is assuming the quantity s as the "entropy". It is defined by $S = \Sigma(s) = \log(s)$ and then one can compute all the thermodynamical variables as a function of ρ and s:

$$\epsilon = \epsilon_{cold}(\rho) + s^{\Gamma_{th}-1} \cdot (\alpha\rho)^{\Gamma_{th}-1} \tag{2.21}$$

$$p = p_{cold}(\rho) + (\Gamma_{th} - 1) \cdot \rho \cdot s^{\Gamma_{th}-1} \cdot (\alpha\rho)^{\Gamma_{th}-1} \tag{2.22}$$

$$t = (\Gamma_{th} - 1) \cdot s^{\Gamma_{th}-2} \cdot (\alpha\rho)^{\Gamma_{th}-1} . \tag{2.23}$$

The physical interpretation of the case $\Gamma_{th} = 2$ is quite difficult, since such value would imply that the density could be interpreted as the temperature of the system. One can write the "entropy" s and the temperature t in terms of the density and internal energy:

$$\epsilon_{th} = (\epsilon - \epsilon_{cold}(\rho)) \tag{2.24}$$

$$t = (\Gamma_{th} - 1) \cdot (\epsilon_{th})^{(\Gamma_{th}-2)/(\Gamma_{th}-1)} \cdot (\alpha\rho) \tag{2.25}$$

$$s = (\epsilon_{th})^{1/(\Gamma_{th}-1)} / (\alpha\rho) \tag{2.26}$$

$$t \cdot s = (\epsilon_{th}) . \tag{2.27}$$

This concludes the discussion on the equation of state of binary neutron star systems and the thermodynamics of the polytropic approximation that was used in this work. Additional information on the hydrodynamics of BNS in numerical relativity can be found in chapter 3, while the results of the simulations based on these EOSs will be discussed in chapter 4.

2.3 Gravitational waves

Gravitational waves are one of the predictions of Albert Einstein's theory of general relativity (GR), which was formulated in 1916, following the publication of the GR field equations [82]. Gravitational waves are a consequence of imposing a relativistic nature to gravitational interactions and consists in perturbations of the spacetime. They are generated by the motion of bulk massive sources, if they have a quadrupolar (or higher) component, propagating at the speed of light with their amplitude decaying like the inverse of the distance from the source. Electromagnetic waves, which are more familiar, instead are generated by the superposition of the motion of microscopic charges and have a dipolar nature.

In the late 60s the quest for the direct detection of gravitational waves began with the work of Joseph Weber, who made the first try to detect such phenomena using aluminum cylinders as antennae. The indirect proof of the existence of gravitational waves was found following the discovery of the pulsar B1913+16 by Hulse and Taylor in 1974 [83]. This binary system was then followed and precise timing measurements were made in the years after the discovery, showing an agreement between the orbital shrinking and the predictions from GR due to the emission of gravitational wave from a quadrupole. This scientific effort was finally rewarded on 14th September 2015, when the first gravitational wave signal from a binary black hole was detected by the LIGO interferometers [2] and then on 17th of August 2017 when the first signal from a BNS source was detected followed by its electromagnetic counterpart [4].

2.3.1 Gravitational waves in linearized gravity

In order to show the presence of gravitational radiation in GR, it is convenient to use the *linearized theory of gravity*. In effect, the spacetime $g_{\mu\nu}$ far from massive sources such as black holes or neutron stars can be considered

$$g_{\mu\nu} = \eta_{\mu\nu} + h_{\mu\nu}, \tag{2.28}$$

where $\eta_{\mu\nu}$ is the Minkowsky metric and $h_{\mu\nu}$ a small perturbation, such as $|h_{\mu\nu}| \ll 1$. The Einstein equations written in (2.2) can be written in terms of the tensor $G_{\mu\nu} = R_{\mu\nu} + \frac{1}{2} g_{\mu\nu} R$ as

$$G_{\mu\nu} = 8\pi T_{\mu\nu} \tag{2.29}$$

and in the linearized theory they become

$$\Box \bar{h}_{\mu\nu} - 2\partial_{(\mu}\partial^{\rho}\bar{h}_{\nu)\rho} + \eta_{\mu\nu}\partial^{\rho}\partial^{\sigma}\bar{h}_{\rho\sigma} = -16\pi T_{\mu\nu}. \tag{2.30}$$

In Eq. (2.30) it was introduced the trace-reversed metric perturbation:

$$\bar{h}_{\mu\nu} := h_{\mu\nu} - \frac{1}{2} h \eta_{\mu\nu}, \tag{2.31}$$

where $h = \eta^{\mu\nu} h_{\mu\nu}$ is the trace of the perturbation.

The metric introduced in (2.28) is not unique since one is free to perform an infinitesimal coordinate transformation $x^{\alpha} \to x^{\alpha} - \xi^{\alpha}$ that does not change (2.28). The linearized theory is then invariant under the gauge transformation

$$h_{\mu\nu} \to h_{\mu\nu} + 2\partial_{(\mu}\xi_{\nu)}, \tag{2.32}$$

meaning that (2.30) does not change under it. A viable choice in this case could be the Lorenz gauge

$$\partial^{\mu}\bar{h}_{\mu\nu} = 0. \tag{2.33}$$

This situation is similar to that of electromagnetism, where the Faraday tensor $F_{\mu\nu}$ is invariant under gauge transformations of the quadri-vector potential $A_{\mu} \to A_{\mu} + \partial_{\mu} B$, which allow the imposition of the Lorenz gauge $\partial^{\mu} A_{\mu} = 0$. This choice simplifies Maxwell's equations into the wave equation. Similarly, (2.33) allows the Einstein equations to become the wave equations

$$\Box \bar{h}_{\mu\nu} = -16\pi T_{\mu\nu} \tag{2.34}$$

for the quantity $\bar{h}_{\mu\nu}$, which travels at the speed of light.

Now we take the example of the wave equation for gravitational waves in vacuum, which are governed by the equation $\Box\bar{h}_{\mu\nu} = 0$. It is simple to show the presence of two distinct polarization of the gravitational radiation, starting from decomposing $\bar{h}_{\mu\nu}$ with a Fourier transform

$$\bar{h}_{\mu\nu} = \int A_{\mu\nu}(k)e^{ik_\rho x^\rho} d^4k \tag{2.35}$$

where $A_{\mu\nu}$ is the *amplitude* of the wave and k_μ the *wave vector*. The gauge condition in (2.33) does not fix uniquely the metric perturbations but leaves room for another gauge transformation, because any choice of ξ_μ which satisfies $\Box\xi_\mu = 0$ will preserve (2.33). This allows to fix the so-called "Transverse Traceless" (TT) gauge after selecting an observer with velocity u_μ, imposing the following conditions for the metric perturbation amplitude:

$$u^\mu A_{\mu\nu} = 0 \tag{2.36}$$
$$\eta^{\mu\nu} A_{\mu\nu} = 0. \tag{2.37}$$

The traceless condition $h = 0$ which implies also $\bar{h}_{\mu\nu} = h_{\mu\nu}$. In the TT gauge, in the rest frame of the observer with velocity u_μ, for a gravitational wave that propagates in the z direction one can write the metric perturbation as

$$h^{TT}_{\mu\nu} = \begin{pmatrix} 0 & 0 & 0 & 0 \\ 0 & h_+ & h_\times & 0 \\ 0 & h_\times & -h_+ & 0 \\ 0 & 0 & 0 & 0 \end{pmatrix} \tag{2.38}$$

where h_+ and $h_\times$ are the two independent polarization of the gravitational wave. Their names come from their interactions with matter: the "plus" polarization deforms a circle with the center at the center of a Cartesian coordinates system alternatively along the x and y axis, while the "cross" one alternatively along the bisectors of the two axis bisector.

Now taking into consideration the generation of gravitational waves from a generic source in the linearized theory approximation, one can just try to derive again the generated metric perturbation. The starting point is (2.34) and for each component $\bar{h}_{\mu\nu}(t, \vec{x})$, the linear equation can be solved using the retarded variable $t' := t - |\vec{x} - \vec{x'}|$, resulting in

$$\bar{h}_{\mu\nu}(t, \vec{x}) = 4 \int \frac{T_{\mu\nu}(t', \vec{x'})}{|\vec{x} - \vec{x'}|} d^3x'. \tag{2.39}$$

This expression can be simplified in the case of an emitted gravitational wave far from the source, so when $r = |\vec{x}| \gg R_{source}$ one can substitute in the denominator of (2.39) the expression $|\vec{x} - \vec{x'}| \simeq r$. Another possible approximation is the "slow source" one, considering that the wavelength λ associated with the characteristic source variation is much bigger than the source size, therefore $\lambda \gg R_{source}$. The "slow source" approximation allows to change also the numerator of (2.39), which becomes

$$\bar{h}_{\mu\nu} = \frac{4}{r} \int t_{\mu\nu}(t - r, \vec{x'}) d^3x'. \tag{2.40}$$

An important constraint to consider is the conservation of the energy-momentum tensor which, in the linearized gravity, is simply $\partial^\mu T_{\mu\nu} = 0$, without the covariant derivative that it is found in the full non-linear theory. If one considers a volume containing the source but with its boundary outside it, the time component of the $T_{\mu\nu}$ conservation can be written

$$\partial_0 T^{00} = -\partial_i T^{i0}. \tag{2.41}$$

Differentiating both sides of (2.41) respect to time, using the symmetry of $T_{\mu\nu}$ and then using the conservation of energy-momentum once again one can obtain

$$\partial_0^2 T^{00} = -\partial_0 \partial_i T i0 = \partial_i \partial_j T^{ij}. \tag{2.42}$$

Now multiplying both sides for $x^i x^j$ and integrating over the considered volume, the last term can be integrated by parts, because the source term will vanish due to the fact that the boundary is outside the source. With this process one obtains:

$$\int T^{ij} d^3x = \frac{1}{2}\partial_0^2 \int x^i x^j T^{00} d^3x \tag{2.43}$$

Applying this to (2.40) one comes to this result

$$\bar{h}_{ij}(t, \vec{x}) = \frac{2}{r} \ddot{I}_{ij}(t - r) \tag{2.44}$$

where I_{ij} is the second mass moment

$$I_{ij}(t) = \int \rho(t, \vec{X}) x_i x_j d^3x. \tag{2.45}$$

Projecting in the TT gauge, one finally obtains the famous formula for the quadrupole emission

$$h_{ij}^{TT}(t, \vec{x}) = \frac{2}{r} \Lambda_{ij,kl}(\vec{n}) \ddot{Q}_{ij}(t - r) \tag{2.46}$$

where $\Lambda_{ij,kl} = P_{ik}P_{jl} - \frac{1}{2}P_{ij}P_{kl}$ depends on the projection operator $P_{ij} = \delta_{ij} - n_i n_j$, with $\vec{n} = \vec{x}/r$, and Q_{ij} is the mass quadrupole moment, which is the traceless part of (2.45)

$$Q_{ij}(t) = \int \rho(t, \vec{x}) \left(x_i x_j - \frac{1}{3}|\vec{x}|^2 \delta_{ij} \right) \tag{2.47}$$

Another quantity that is related to the mass quadrupole moment Q is then the energy of the gravitational radiation and its power output. In chapter 36 of [84], the authors stress that the electromagnetic and gravitational theories have some similarities, which were also mentioned in this chapter, and point out that the power output for the quadrupole generated radiation behaves the same way. In effect, if $L_{\text{electric}} = \frac{1}{20}\dddot{\mathbf{Q}} \equiv \frac{1}{20}\dddot{Q}_{jk}\dddot{Q}_{jk}$ then the power output related to the mass quadrupole can be expressed as

$$L_{\text{mass quadrupole}} = \frac{1}{5}\langle\dddot{\mathbf{Q}}^2\rangle \equiv \frac{1}{5}\langle\dddot{Q}_{jk}\dddot{Q}_{jk}\rangle, \tag{2.48}$$

where the factor 1/5 comes from tensor calculations, instead of the 1/20 of the electromagnetic one, and has been averaged over several characteristic periods of the source due to the inability to localize the energy of the gravitational radiation inside a wavelength.

The expression in (2.48) can be rewritten in a more simple way for order-of-magnitude estimates. In effect,

$$Q_{jk} \sim \frac{MR^2}{T^3} \sim \frac{M(R/T)^2}{T} \sim \frac{\binom{\text{nonspherical part}}{\text{of kinetc energy}}}{T}$$

then

$$\dddot{Q}_{jk} \sim L_{\text{internal}} \equiv \begin{pmatrix}\text{power flowing from one} \\ \text{side of system to other}\end{pmatrix}. \tag{2.49}$$

It follows from (2.48) that the *luminosity* in gravitational waves is roughly the square of the internal power flow

$$L_{\text{GW}} \sim \left(L_{\text{internal}}\right)^2, \tag{2.50}$$

which seems not consistent, from a dimensional point of view, but it has to be noted that power is dimensionless in geometrized units, converting with

$$L_0 \equiv c^5/G = 3.63 \times 10^{59}\,\text{erg/s} = 2.03 \times 10^5\,\text{M}_\odot c^2/\text{s}. \tag{2.51}$$

Equation (2.50) does not consider all those internal power flows that cannot radiate gravitational waves, i.e. those that do not accompany a time-changing quadrupole moment. In a star, the internal power flows associated with spherical pulsation and axially symmetric rotation are the effects that do not contribute to L_{GW}.

2.3.2 Gravitational waves from astrophysical objects

Gravitational waves can be generated by a variety of highly dynamic astrophysical system, such as pulsating stars, rotating stars, collapsing stars or exploding stars. If the mass of the system is M and its size is R, then, according to the virial theorem, the kinetic energy is then $\sim M^2/R$. The time-scale for mass to move from one side of the system to the other is then

$$T \sim \frac{R}{\text{(mean velocity)}} \sim \frac{R}{(M/R)^{1/2}} = \left(\frac{R^3}{M}\right)^{1/2}, \tag{2.52}$$

which is similar to the time of free fall and the time to turn one radian in Kepler orbit. Therefore, the internal power flow is

$$L_{\text{internal}} \sim \frac{\text{(kinetic energy)}}{T} \sim \left(\frac{M^2}{R}\right)\left(\frac{M}{R^3}\right)^{1/2} \sim \left(\frac{M}{R}\right)^{5/2}. \tag{2.53}$$

The gravitational wave luminosity is computed as in (2.50), therefore

$$L_{\text{GW}} \sim \left(\frac{M}{R}\right)^5 L_0. \tag{2.54}$$

It's important to note that the maximum luminosity occurs when the system is near its gravitational radius and the maximum value corresponds to $\sim L_0 = 3.63 \times 10^{59}$ erg/s, regardless of the nature of the system. These equations uses approximations that break down near the gravitational radius: in effect, velocities small compared to c are required and nearly Newtonian fields are required for the virial theorem.

Gravitational collapse, black holes, supernovae and pulsars as gravitational wave sources

The most intense gravitational waves that can reach Earth come from dynamic deformed systems near their gravitational radius, as it is showed before. Also, it is important to note that in order to emit gravitational radiation, such systems must be far from any state of equilibrium, otherwise the radiation reaction will damp the internal motion and prevent the emission of gravitational waves.

One of the favorable sources for gravitational wave radiation is a star collapsing through its gravitational radius in a highly non-spherical manner. The end of the life of such a star could be a blast of gravitational waves which carry off a sizeable fraction of its rest mass. One can make an estimate of the order-of-magnitude:

$$\begin{aligned} E_{\text{radiated}} = \int L_{\text{GW}} dt \sim L_0 \cdot \begin{pmatrix} \text{time during which} \\ \text{peak luminosity occurs} \end{pmatrix} \\ \sim L_0 M = M. \end{aligned} \tag{2.55}$$

Another source of gravitational waves could be matter (*debris*) falling into a black hole. The infalling matter weakly radiate when it is far from the gravitational radius, but when it falls through $r \sim 4\text{M}$ and $r = 2\text{M}$ it should emit a strong burst. Consider m the mass of the falling matter and M the total mass of the black hole, then the energy radiated is

$$E_{\text{radiated}} \sim m^2/M \tag{2.56}$$

in a time $\sim M$ with a power output $L_{\text{GW}} \sim (m/M)^2 L_0$. In the case of $m \ll M$ one can perform the exact calculation of the spectrum and energy radiated by treating the matter and the waves as small perturbations of the Schwarzschild geometry.

Supernovae explosions can also be a source of gravitational radiation as the collapse itself and the subsequent motion of the collapsed core (neutron star) should produce a short but powerful burst of gravitational waves. So, assuming large departures from sphericity, the estimate on supernovae emission are

$$\begin{aligned} E_{\text{radiated}} &\sim \text{(neutron star binding energy)} \\ &\sim M^2/R \sim 0.1M \sim 10^{53}\,\text{erg} \\ \text{(mean frequency)} &\sim 1/T \sim (M/R^3)^{1/2} \sim 0.03M^{-1} \sim 3000\,\text{Hz} \\ \text{(power output)} &\sim (M/R)^5 L_0 \sim 10^{-5} L_0 \sim 3\times 10^{54}\,\text{erg/s}. \end{aligned} \tag{2.57}$$

The end of the process initiated by the supernovae collapse are neutron stars, as it was mentioned before. Long after the pulsations of the neutron star have been damped out by gravitational radiation reaction, the star will continue to rotate and it will beam out radio waves, light and x-rays due to its off-axis-pointing magnetic moment. This radiation is usually identified as "pulsar radiation". During this pulsar phase, gravitational radiation is important only if the star is somewhat deformed from axial symmetry, as a small deformation of the star's mass could radiate 10^{38} erg/s.

Gravitational waves from binary stars

The most numerous sources of gravitational waves are binary star systems. Two stars of masses m_1 and m_2 that circle each other with frequency ω and separation a are coupled each other according to Kepler's law

$$\omega^2 a^3 = m_1 + m_2 \equiv M. \tag{2.58}$$

The kinetic energy in this motion is

$$\text{(kinetic energy)} = -\frac{1}{2}\text{(potential energy)} = \frac{1}{2}\frac{m_1 m_2}{a}. \tag{2.59}$$

Therefore, the power radiated as gravitational waves can be estimated roughly as the square of the circulating power ($L \sim \omega\times$ (kinetic energy)) as

$$L_{\text{GW}} \sim \frac{\mu^2 M^3}{4a^5} L_0, \tag{2.60}$$

where $\mu = m_1 m_2/M$ is the reduced mass and $M = m_1 + m_2$ is the total mass of the system.

Based on eq. (2.48), a more accurate calculation can be done considering a system of semimajor axis a and eccentricity ε, resulting in

$$L_{\rm GW} = \frac{32}{5}\frac{\mu^2 M^3}{a^5} f(\varepsilon) L_0, \tag{2.61}$$

where $f(\varepsilon)$ is the dimensionless "correction function"

$$f(\varepsilon) = \left[1 + \frac{73}{24}\varepsilon^2 + \frac{37}{96}\varepsilon^4\right]\left[1-\varepsilon^2\right]^{-7/2}. \tag{2.62}$$

The system loses energy by gravitational radiation and the stars begin to spiral in toward each other as the gravitational binding increases. For circular orbits, the energy $E = -\frac{1}{2} m_1 m_2/a = -\frac{1}{2}\mu M/a$ decreases as

$$\begin{aligned} \mathrm{d}E/\mathrm{d}t &= 1/2\left(\mu M/a^2\right)(\mathrm{d}a/\mathrm{d}t) \\ &= -L_{\rm GW} = -\frac{32}{5}\frac{\mu^2 M^3}{a^5}. \end{aligned} \tag{2.63}$$

Therefore, the orbital radius evolves like

$$a = a_0\left(1 - t/\tau_0\right)^{1/4}, \tag{2.64}$$

where $a_0 = a_{\rm today}$ and

$$\tau_0 = \frac{1}{4}\left(\frac{-E}{L_{\rm GW}}\right)_{\rm today} = \frac{5}{256}\frac{a_0^4}{\mu M^2}. \tag{2.65}$$

Thus, the two stars will inspiral together in a *spiral* time τ_0, unless non-gravitational forces intervene and in the case of an elliptical orbit, also the eccentricity evolves.

Chapter 3

Numerical background: the numerical solution of Einstein equations and hydrodynamics

From a numerical point of view, the problem of solving PDEs on a computer, which is the case of the Einstein equations and the general relativistic (magneto-)hydrodynamics (GRMHD) ones has been addressed in the last 30 years. The starting point is that of representing continuous functions in time and space at several discrete steps in time and, at each time step, in a discrete spatial grid with a finite number of points, in order to apply discrete operations on spacetime fields, which is what computers are able of. The spatial grid, in particular a three dimensional Cartesian grid in our case, represents a finite region which we are interested to evolve in time. In the case of BNS, the initial grid is much bigger than the distance of the two stars, since it is necessary to extract the gravitational waves far from the source and avoid the interaction between the physical evolved fields and spurious matter and radiation infalling or bouncing back at the grid boundaries.

In order to be evolved in time on a machine, the equations must be written as a system of first order in time PDEs:

$$\partial_t U_i(t,\vec{x}) = RHS\left(U_i(t,\vec{x}), \partial_{\vec{x}} U_i(t,\vec{x}), \partial^2_{\vec{x}} U_i(t,\vec{x},t,\vec{x})\right) \tag{3.1}$$

where U_i is the vector of the evolved variables. The starting point is setting up the initial data in each grid point. The grid points, at each refinement level (it will be discussed later), are uniformly distanced with resolution Δx. The initial data are evolved starting from time t_n to the subsequent time $t_{n+1} = t_n + \Delta t$, using the so called *method of lines*, which is handled by the module `MoL` of the `Einstein Toolkit`. In the `MoL` thorn[1] the right hand side of equation (3.1) is computed approximating the spatial derivatives with appropriate methods that will be discussed later in this chapter. In this way,

[1]"Thorn" is the name of the modules of the code `Cactus`.

the fields U_i depend only on the time variable t in each grid point, leaving a system of ordinary differential equations. After this process, the system can be solved using standard numerical techniques, for instance the fourth-order Runge-Kutta method [85, 86], which is implemented in the `Einstein Toolkit` in order to evolve the solution at time t^n, called U_i^n, to time t^{n+1}, computing the subsequent solution U_i^{n+1} in four steps:

$$U_i^{(0)} = U_i^n \tag{3.2}$$

$$U_i^{(1)} = U_i^{(0)} + \frac{1}{2}\Delta t\, RHS\left(U_i^{(0)}\right) \tag{3.3}$$

$$U_i^{(2)} = U_i^{(0)} + \frac{1}{2}\Delta t\, RHS\left(U_i^{(1)}\right) \tag{3.4}$$

$$U_i^{(3)} = U_i^{(0)} + \frac{1}{2}\Delta t\, RHS\left(U_i^{(2)}\right) \tag{3.5}$$

$$U_i^{(4)} = \frac{1}{6}\left(-2U_i^{(0)} + 2U_i^{(1)} + 4U_i^{(2)} + 2U_i^{(3)} + \Delta t\, RHS\left(U_i^{(3)}\right)\right) \tag{3.6}$$

$$U_i^{n+1} = U_i^{(4)}. \tag{3.7}$$

The need to solve GR(M)HD[2] equations on both a very large grid (all the simulations considered in 4 are performed on a grid with half-edge of approximately 1063 km or 720 $M_\odot$in geometric units) and at the same time achieving a very high spatial resolution (low Δx), is one of the problems to address in order to be able to resolve all the hydrodynamical features and have low numerical dissipation. The solution to this problem was found by Berger and Oliger [87], who first presented the Adaptive Mesh Refinement (AMR) method, which is implemented in the `Einstein Toolkit` by the thorn `Carpet`. In BNS simulations, it is common to choose nested grids, one inside the other, such that each smaller grid has a resolution double to the parent level (meaning two times the density of points and half Δx). Here it is presented an example of how this method works, considering only two grids, one with resolution Δx and the other $2\Delta x$:

1. the coarser level, which also has a larger temporal resolution, evolves from time t to $t + 2\Delta t = t + 2\eta\Delta x$;

2. the *prolongation* method is applied at the fine level boundary: the coarser level points are interpolated in space (using a fifth order polynomial interpolation) and time (using a second order polynomial interpolation), in order to be used as boundary conditions for the fine level evolution;

3. the fine level is evolved two steps in time, so from t to $t + \Delta t$ and, after, from $t + \Delta t$ to $t + 2\Delta t$, to be aligned with the coarse one;

[2]GRHD = general relativistic hydrodynamics

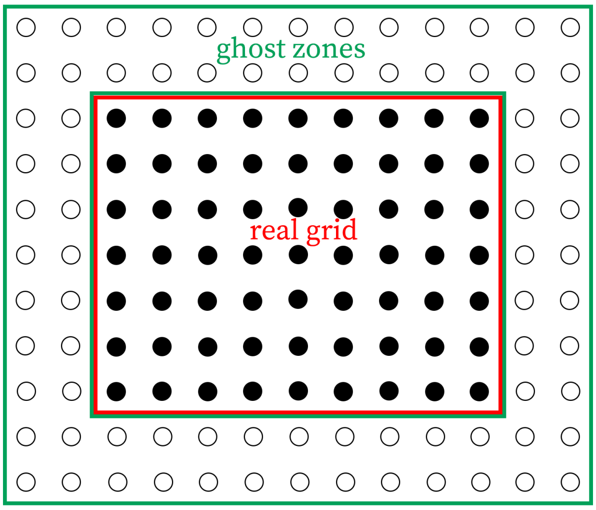

Figure 3.1: Example of grid with ghost zones. The solid black points in the red rectangle represent the points of the grid that contains the real data of the evolution, while the white points in the green rectangle represent the ghost zone. This figure is only representative of the computational process, it does not show the correct number of ghost zones, which is defined as three in the text.

4. the fields values that are positioned on the coarse level points in space that also coincides with a fine level point, are copied to the fine level (this step is called *restriction*). This step is possible without interpolation because the `Carpet` thorn uses a vertex centered grid, which means that where a grid point exists for the fine level, there is also a corresponding point with the same Cartesian coordinates for the coarser level.

The scheme that have been presented above, coupled with a multi-step time evolution like RK4, presents problems at refinement boundaries: boundary conditions, provided by the prolongation step, are needed by the fine grid evolution at each intermediate step of RK4. At the boundaries, this will reduce the convergence to first order [88] and the first BNS simulations, where this problem was not addressed with some additional technique, showed a great loss of accuracy globally. The solution implemented by the `Carpet` thorn is to use buffer zones at refinement boundaries, which means evolving 12 additional grid points for each edge of any refinement level (3 ghost points for each of the four RK4 sub-steps). This process is visually showed in figure 3.1, where the real grid is inside the red square, while the ghost zone is in the outer edge in the between the two green lines. Then at each RK4 step, a set of three points becomes invalid and it is not used anymore. These points are still evolved regularly like any other one instead of being filled with prolongation values, but they are used only as boundaries in order to correctly evolve the inner points in the finer level. This process, of course, leads to higher computational and memory costs, in particular in the case of a code that needs to scale on a high number of cores.

3.1 Curvature evolution

The numerical solution of Einstein's equations and, in particular, the chance of simulating long-term black holes has been a challenge for many years, until the success of the first many-orbits BBH merger simulations in 2005 [89, 90, 91].

In order to simulate the evolution of a system regulated by Einstein's equations, it is necessary to re-write them in the so-called *3+1 formulation*, separating the time coordinate from the spatial ones, which label the spatial grid at each time step. The first introduction of the 3+1 formulation is originally due to Darmois (1927), Lichnerowitz (1944) and Choquet-Bruhat (1952). Then Arnowitt, Deser and Misner used is for developing an Hamiltonian formulation of general relativity, known as the ADM formulation [92].

The first step in the direction of the ADM formulation, which will be the base of the entire section, is the foliation of the spacetime in spacelike hypersurfaces Σ_t as level functions of a scalar field t (the time coordinate). The timelike, future-directed unit normal to each surface n is linked with the field t by the relation

$$n^\mu := -\alpha \nabla^\mu t. \tag{3.8}$$

In equation (3.8) the lapse function α is defined as $\alpha = -\sqrt{\nabla^\mu t \nabla_\mu t}$ and this ensure that the vector n^μ has norm $n^\mu n_\mu = -1$. In the previous formulas, the metric $g_{\mu\nu}$ is implicitly used to lower the vector indexes, and to define the operator

$$\nabla_\mu = g_{\mu\nu} \nabla^\nu. \tag{3.9}$$

It is possible to select a privileged observer, called the *Eulerian observer*, which moves at four-velocity n^μ, meaning that its evolution is normal to Σ_t, that can be viewed as the set of events simultaneous for the Eulerian observer. The normal evolution vector is then defined starting from α as $m^\mu := \alpha n^\mu$ and

$$\nabla_m t = m^\mu \nabla_\mu t = 1, \tag{3.10}$$

which means that the vector $m^\mu \delta t$ carries the hypersurface Σ_t into $\Sigma_{t+\delta t}$. The spatial metric is finally defined on each hypersurface as

$$\gamma_{\mu\nu} := g_{\mu\nu} + n_\mu n_\nu. \tag{3.11}$$

Once the metric is defined, the next step is to decompose Einstein's equations, on each hypersurface, into a spatial part and a component orthogonal to the foliation. This can be done using projection operators:

$$\gamma^{\mu}_{\nu} = \delta^{\mu}_{\nu} + n^{\mu} n_{\nu} \tag{3.12}$$
$$\alpha^{\mu}_{\nu} = -n^{\mu} n_{\nu}, \tag{3.13}$$

where δ^{ν}_{μ} is the Euclidean metric.

After some calculation that can also be found in [93], it can be shown that the spatial projection o the Ricci tensor is:

$$\gamma^{\mu}_{\alpha}\gamma^{\nu(4)}_{\beta} R_{\mu\nu} = -\frac{1}{\alpha}\mathcal{L}_{\mathbf{m}} K_{\alpha\beta} - \frac{1}{\alpha} D_{\alpha} D_{\beta} \alpha R_{\alpha\beta} + K K_{\alpha\beta} - 2K_{\alpha\mu} K^{\mu}_{\beta}, \tag{3.14}$$

where $R_{\alpha\beta}$ is the spatial Ricci tensor on the hypersurface Σ_t, D_{μ} is the spatial covariant derivative computed with the metric $\gamma_{\mu\nu}$, and K is the trace of the extrinsic curvature $K_{\mu\nu}$, which is defined as

$$K_{\mu\nu} = -\gamma^{\mu}_{\alpha}\gamma^{\nu}_{\beta}\nabla_{(\mu} n_{\nu)} \tag{3.15}$$

The extrinsic curvature defined in equation (3.15) can be either seen as the projection on Σ_t of the gradient of its unit normal or the rate of change of the spatial metric. The energy-momentum tensor, instead, can be projected as

$$S_{\mu\nu} = \gamma^{\alpha}_{\mu}\gamma^{\beta}_{\nu} T_{\alpha\beta} \tag{3.16}$$
$$e = n^{\mu} n^{\nu} T_{\mu\nu} \tag{3.17}$$
$$j_{\mu} = -\gamma^{\alpha}_{\mu} n^{\beta} T_{\alpha\beta}, \tag{3.18}$$

where e can be interpreted as the energy density and j_{μ} as the momentum density measured by the Eulerian observer.

In order to come to the final ADM formulation, it is necessary to introduce a coordinate system, adopted to the foliation, to write the tensorial expression that have been shown before as a system of PDEs. First, one introduces the the coordinates x^i, $i \in [1, 3]$ on each hypersurface Σ_t. Then, it is defined a coordinate t, such as the vector ∂_t is tangent to the lines of constant spatial coordinates. The vector ∂_t is dual to the 1-form dt, just like the normal evolution vector $\mathbf{m}$ defined in equation (3.10). However, m^{μ} and ∂_t generally differ, and their difference is defined as the shift vector β:

$$\beta^{\mu} := \partial^{\mu}_{t} - m^{\mu}. \tag{3.19}$$

From this definition, taking into consideration equation (3.10), one can derive

$$\partial^{\mu}_{t} = -\alpha n^{\mu} + \beta^{\mu}, \tag{3.20}$$

and for the Lie derivatives,

$$\mathcal{L}_m = \mathcal{L}_{\partial_t} - \mathcal{L}_{\beta}. \tag{3.21}$$

The components of the normal unit vector n^μ and its dual 1-form n_μ can also be expressed as

$$n^\mu = \left(\frac{1}{\alpha}, -\frac{\beta^i}{\alpha}\right) \tag{3.22}$$

$$n_\mu = \left(-\alpha, \vec{0}\right). \tag{3.23}$$

This allows to decompose the four-dimensional metric $g_{\mu\nu}$ into a 3+1 form and write it respect to the chosen coordinate system:

$$\mathrm{d}s^2 = g_{\mu\nu}\mathrm{d}x^\mu \mathrm{d}x^\nu = -\left(\alpha^2 - \beta^i\beta_i\right)\mathrm{d}t^2 + 2\beta_i \mathrm{d}x^i \mathrm{d}t + \gamma_{ij}\mathrm{d}x^i \mathrm{d}x^j. \tag{3.24}$$

This opens up to the physical interpretation of the lapse, which represents a measure of the proper time for the Eulerian observer between two adjacent hypersurfaces:

$$\mathrm{d}\tau^2 = -\alpha^2(t, x^i)\mathrm{d}t; \tag{3.25}$$

and the shift vector, which represents the relationship between spatial coordinates of two adjacent hypersurfaces:

$$x^i_{t+\delta t} = x^i_t - \beta^i(t, x^i)\mathrm{d}t. \tag{3.26}$$

Both the lapse *alpha* and the shift vector β^i characterize the choice of the coordinate system for the time evolution and they are gauge variables whose evolution can be freely chosen. This choice is very important to guarantee numerical stability and will be discussed later in this chapter.

At this point, it is finally possible to derive the full set of ADM equations, projecting the Einstein's equations and writing them in the chose coordinate system. Applying the projection in the direction normal to Σ_t twice, one obtains:

$$R + K^2 - K_{ij}K^{ij} - 16\pi e = 0, \tag{3.27}$$

where $R = g_{\mu\nu}R^{\mu\nu}$ is the scalar curvature. This equation is called *Hamiltonian constraint*. Similarly, applying space and time projection, one obtains:

$$D_j K^j_i - D_i K - 8\pi j_i = 0, \tag{3.28}$$

which are called *Momentum constraint*. Equations (3.27) and (3.28) are elliptic equations, valid in each hypersurface Σ_t. Since solving elliptic equations numerically is computationally heavy, these four constraints are not solved in the numerical scheme implemented in the `Einstein Toolkit` but, instead, they are evolved in order to monitor if large violations occur due to numerical errors.

Projecting Einstein's equations two times on Σ_t, one obtains, starting from the expression in equation (3.14), and writing the equations as $R_{\mu\nu} =$

$8\pi\left(T_{\mu\nu} - \frac{1}{2}g_{\mu\nu}T\right)$, where T is the trace of the energy-momentum tensor, the evolution equation for the extrinsic curvature:

$$\begin{aligned}\partial_t K_{ij} = & -D_i D_j \alpha + \alpha\left(R_{ij} - 2K_{ik}K^{kj} + KK_{ij}\right) + \\ & -8\pi\alpha\left(R_{ij} - \frac{1}{2}\gamma_{ij}(S-e)\right) + \mathcal{L}_\beta K_{ij}.\end{aligned} \tag{3.29}$$

With equation (3.29) it is described how the spacetime geometry changes going from one hypersurface to the future adjacent one. These ten equations (six evolution equations for K_{ij} and four constraint equation) are supplemented by the relationship between the spatial metric and the extrinsic curvature, which, using equations (3.21) and (3.15), can be written as

$$\partial_t \gamma_{ij} = -2\alpha K_{ij} + \mathcal{L}_\beta \gamma_{ij}. \tag{3.30}$$

3.1.1 The BSSN formulation

Unfortunately, the ADM formulation of general relativity, presented in the evolution equations (3.29) and (3.30) and the constraint (3.27) and (3.28), cannot be used in practice for numerical simulations because it is only weakly hyperbolic and would quickly lead to numerical instabilities, causing the code to crash. A new formulation of Einstein's equation was developed in the late 1990s and early 2000s by Baumgarte, Shapiro, Shibata, Nakamura, and Oohara and Kojima and it is commonly known as BSSN-OK formulation [94, 95, 96].

The extrinsic curvature K_{ij} and the spatial metric γ_{ij} are not evolved, but new variables can be introduced and evolved separately. First, it is introduced a conformal spatial metric as

$$\tilde{\gamma}_{ij} := e^{-4\phi}\gamma_{ij}, \tag{3.31}$$

with the conformal factor ϕ

$$\phi := \log\left(\frac{1}{12}\det\gamma_{ij}\right) \tag{3.32}$$

as a new evolved variable. It is then introduced the conformal, trace-free extrinsic curvature as another new variable to be evolved:

$$\tilde{A}_{ij} := e^{-4\phi}\left(K_{ij} - \frac{1}{3}g_{ij}K\right), \tag{3.33}$$

with $K = g^{ij}K_{ij}$. The conformal metric $\tilde{\gamma}_{ij}$ is used to raise or lower the indexes of $\tilde{A}_{ij}$. Finally, it is introduced the conformal connection functions as

$$\tilde{\Gamma}^i := \tilde{\gamma}^{jk}\tilde{\Gamma}^i_{jk} = \partial_j - \tilde{\gamma}^{ij}, \tag{3.34}$$

where $\tilde{\Gamma}^i_{jk}$ are the Christoffel symbols of $\tilde{\gamma}_{ij}$. Separating the trace part and the trace-free part of the ADM formulation in equations (3.29) and (3.30), one can obtain the full BSSN system:

$$\begin{aligned}
\left(\partial_t - \beta^j\partial_j\right) K &= -\gamma^{ij}\tilde{D}_i\tilde{D}_j\alpha + \alpha\left(\tilde{A}^{ij}\tilde{A}_{ij} + \frac{1}{3}K^2\right) \\
&\quad + 4\pi(e + \gamma^{ij}S_{ij}) && (3.35) \\
\left(\partial_t - \beta^j\partial_j\right)\phi &= -\frac{1}{6}\left(\alpha K - \partial_k\beta^k\right) && (3.36) \\
\left(\partial_t - \beta^j\partial_j\right)\tilde{\Gamma}^i &= -2\tilde{A}^{ij}\partial_j\alpha + 2\alpha\left[\tilde{\Gamma}^i_{kl}\tilde{A}^{kl} + 6\tilde{A}^{ij}\partial_j\phi - \frac{2}{3}\tilde{\gamma}^{ij}\partial_j K\right] && (3.37) \\
&\quad - \tilde{\Gamma}^j\partial_j\beta^i + \frac{2}{3}\tilde{\Gamma}^i\partial_j\beta^j + \frac{1}{e}\tilde{\gamma}^{ik}\partial_j\partial_k\beta^j + \tilde{\gamma}^{jk}\partial_j\partial_k\beta^i - 16\pi\alpha\tilde{\gamma}^{ik}j_k \\
\left(\partial_t - \beta^j\partial_j\right)\tilde{\gamma}_{ij} &= -2\alpha\tilde{A}_{ij} + 2\tilde{\gamma}_{k(i}\partial_{j)}\beta^k - \frac{2}{3}\tilde{\gamma}_{ij}\partial_k\beta^k && (3.38) \\
\left(\partial_t - \beta^j\partial_j\right)\tilde{A}_{ij} &= e^{-4\pi}\left[\alpha\tilde{R}^{\phi}_{ij} - \tilde{D}_i\tilde{D}_j\alpha\right]^{TF} + && (3.39) \\
&\quad + \alpha K\tilde{A}_{ij} - 2\alpha\tilde{A}_{ki}\tilde{A}^k_j + 2\tilde{A}_{k(i}\partial_{j)}\beta^k - \frac{2}{3}\tilde{A}_{ij}\partial_k\beta^k \\
&\quad - 8\pi\alpha e^{-4\pi}S^{TF}_{ij},
\end{aligned}$$

where TF stands for "trace-free", $\tilde{D}_i$ is the covariant derivative associated with the conformal spatial metric. These equations have been derived using the Hamiltonian and momentum constraint that have been defined before. In particular, it is important to use the momentum constraint to eliminate the divergence of $\tilde{A}_{ij}$ from the evolution equations for $\tilde{\Gamma}^i$, in order to ensure numerical stability. In [97, 98], it was proven that this system of 17 PDEs is strongly hyperbolic, even if it is not easy to see it at first glance. At each evolution step, five additional constraints have been introduced in this formulation:

$$\det\left(\tilde{\gamma}_{ij}\right) = 1 \tag{3.40}$$

$$\mathrm{Tr}\left(\tilde{A}_{ij}\right) = 0 \tag{3.41}$$

$$\tilde{\Gamma}^i = \tilde{\gamma}^{jk}\tilde{\Gamma}^i_{jk}. \tag{3.42}$$

The first two constraints are actively enforced at each time step, while the third one is not, as for the case of the Hamiltonian and momentum constraint. However, the evolved $\tilde{\Gamma}^i$ are used only where their derivatives are needed, otherwise $\tilde{\gamma}^{jk}\tilde{\Gamma}^i_{jk}$ is used in order to help keeping its violation low.

As it was mentioned before, in addition to this system, a choice for the gauge variables $\alpha(t, x^i)$ and $\beta^j(t, x^i)$ is necessary. Simplistic choices like the geodesic slicing ($\alpha = 1$, $\beta^i = 0$) do not work since they are not singularity avoiding, causing code crash in BH simulations. Therefore, there is a need for a singularity avoiding condition in the choice of α. In effect, the lapse cannot be constant everywhere, but should be close to the Minkowski value of 1 in the asymptotic flat region near the grid outer boundaries and should become close to 0 in the vicinity of a black hole, in order to avoid reaching the singularity. This requirement causes the additional problem of time advancing "faster" in the outer regions and being almost frozen near the BH, resulting in the grid (or, more precisely, each hypersurface Σ_t) to get strongly distorted (*grid stretching*), with grid points falling inside the BH horizon, even if they are excised from the numerical evolution. This, of course, causes the code to crash due to the large gradients in the metric functions. In order to fix it, also the spatial condition for the shift vector β^i should be set so that it changes in space and time.

A common choice for the lapse is the *maximal slicing* condition $K = 0$, or the related *K-freezing* one $\partial_t K = 0$ (equivalent in the case of $K = 0$ set in the initial data). The latter, however, leads to the need of solving an elliptic equation for the lapse at each step, which is computationally expensive:

$$\Delta\alpha = \beta^i \partial_i K + \alpha K_{ij} K^{ij}. \tag{3.43}$$

An alternative solution, that would make the computation more efficient constructing an hyperbolic slicing condition, is called the $K-driver$ condition, making $\partial_t^2 \alpha$ proportional to $\partial_t K$ [99, 100]:

$$\partial_t \alpha - \beta^i \partial_i \alpha = -2\alpha K. \tag{3.44}$$

This condition is also known as *1+log slicing*. To avoid grid stretching one can also set a spatial gauge condition to the shift vector. A common choice is the so called *Gamma-freezing* condition $\partial_t \tilde{\Gamma}^i = 0$, which implies solving elliptic equations for β^i, or the dynamical *Gamma-driver* condition, which is hyperbolic instead, as implemented in the `Einstein Toolkit`:

$$\partial_t \beta^i - \beta_j \partial^j \beta^i = \frac{3}{4} B^i \tag{3.45}$$

$$\partial_t B^i - \beta_j \partial^j \beta^i = \partial_t \tilde{\Gamma}_i - \eta B^i. \tag{3.46}$$

Here an additional evolved variable B^i has been introduced. The factor η is called "Beta-driver" and works as a damping factor, driving B^i (and then $\partial_t \beta^i$) to zero, so the shift vector will tend to a constant in a stationary spacetime. Considering that η has dimensions $[1/T]$, it sets, depending on the numerical integration method a Courant-like limitation for the time step size, which is independent from the spatial resolution.

These BSSN-OK equations are implemented in the `McLachlan` thorn of the `Einstein Toolkit` [23, 101], auto-generated as highly efficient vectorized code from a Mathematica script written in tensorial notation with `Kranc` [102]. The spatial partial derivatives in the equations are computed with a fourth-order finite differencing representation. If f_n is the value of a function f in the n-th grid point in the x-direction, then its derivative is expressed as:

$$\partial_x f = \frac{1}{12} f_{n-2} - \frac{2}{3} f_{n-1} + \frac{2}{3} f_{n+1} - \frac{1}{12} f_{n+2}. \tag{3.47}$$

The advection terms $\beta^i \partial_i$ are computed using a fourth-order upwind scheme, instead of centered differences, in order to have a better numerical stability. Finally a Kreiss-Oliger fifth-order dissipation is applied to the evolved variables, with a strength of $\epsilon_{\text{diss}} = 0.01$, in order to damp high-frequency oscillations.

The BSSN-OK formulation must be supplemented by suitable boundary conditions at the external edges of the grid in order to obtain a stable evolution at the boundary, with constraint preservation and gravitational waves that propagate out of the grid and are not reflected back inside. In the `Einstein Toolkit` this *no-incoming radiation* boundary condition is imposed adopting Sommerfeld-type radiative boundary conditions [103]. For each evolved variable tensor component X, the main part of the boundary condition is

$$X = X_0 + \frac{u(r - v_0 t)}{r}, \tag{3.48}$$

which behaves like an outgoing radial wave with speed v_0. In equation (3.48), u is a spherically symmetric perturbation and X_0 the component value at spatial infinity. This takes the assumptions that the waves have a spherical wavefront at the boundary, which is true if the boundary is far enough from the source. This is obtained deriving it in time and obtaining the following differential equation, which is easier to impose in a finite-differencing code:

$$\partial_t X = -\frac{v_0 x^i}{r} \partial_i X - v_0 \frac{X - X_0}{r}. \tag{3.49}$$

The spatial derivatives are computed with second order central finite differencing when it is possible, with one-sided finite differencing otherwise. In order to account also those parts which do not behave like a pure outgoing wave, the time derivative term $\partial_t X$ is modified with:

$$(\partial_i X)^* = \partial_t X + \left(\frac{r}{r - n^i \partial_i r} \right)^p n^i \partial_i (\partial_t X), \tag{3.50}$$

where n^i is the unit normal vector of the considered boundary face. This correction decays with a power $p = 2$ of the radius in our simulations. These conditions are implemented in the thorn `newrad` of the `Einstein Toolkit`.

3.2 Matter evolution

In neutron stars simulations, the evolution of the spacetime, which was the topic of section 3.1, must be coupled with the (magneto-)hydrodynamical evolution for the matter. The framework for the hydrodynamics is still the 3+1 formulation with the spacetime metric of (3.24), which is supplemented by an additional important variable as the fluid four-velocity u^μ. This variable can be seen as the velocity of an Eulerian observer comoving with the fluid and has module $u^\mu u_\mu = -1$ like the Eulerian observer velocity n^μ. The equations of the GR(M)HD are written in the Eulerian observer reference frame, so it is important to consider the spatial projection v^i on the hypersurface Σ_t of the fluid four-velocity measured by the Eulerian observer. The projection is given by

$$v^i = \frac{\gamma^i_\mu u^\mu}{-w^\mu n_\mu} = \frac{1}{\alpha}\left(\frac{u^i}{u^0} + \beta^i\right). \tag{3.51}$$

If one takes this expression and chooses $\alpha = 1$ and $\beta^i = 0$ for the gauge variables, the special relativistic expression $v^i = \frac{\mathrm{d}x^i}{\mathrm{d}t} = \frac{u^i}{u^0}$, with $u^i = \frac{\mathrm{d}x^i}{\mathrm{d}t}$, is recovered. With some simple algebra and using the unitarity of the u^μ module, it can be shown that

$$\alpha u^0 = \frac{1}{\sqrt{1 - v_i v^i}} := W \tag{3.52}$$

where it is defined W as the Lorenz factor of the fluid.

Then we consider the ideal-fluid energy-momentum tensor:

$$T^{\mu\nu} = \rho h u^\mu u^\nu + p g^{\mu\nu}, \tag{3.53}$$

where ρ is the mass density, $h = 1 + \epsilon + \frac{p}{\rho}$ is the relativistic specific enthalpy, ϵ is the specific energy density and p is the pressure. The equation to solve for the hydrodynamics are

$$\nabla_\mu T^{\mu\nu} = 0 \tag{3.54}$$

$$\nabla_\mu(\rho u^\mu) = 0, \tag{3.55}$$

where equation (3.54) is the energy-momentum conservation and equation (3.55) is the baryon number conservation. This system of equations should be closed with the choice for the EOS, as discussed in section 2.2, in the form of $p = p(\rho, \epsilon, ...)$.

From a numerical point of view, the hydrodynamics is handled by the `GRHydro` thorn [104], which is the official, open source, GRHD module in the `Einstein Toolkit`, that uses the so called *Valencia formulation* of the GR(M)HD equations [105, 106, 107, 108, 109]. This is a conservative formulation where, instead of the natural *primitive* variables (ρ, ϵ, v^i), a set of derived *conserved* variables is evolved, in order to be able to write the hydrodynamics equation in the conservative form

$$\partial_t \mathbf{U} = \partial_i \mathbf{F}^{(i)}(\mathbf{U}) + \mathbf{S}(\mathbf{U}), \tag{3.56}$$

where $\mathbf{U}$ is the state vector containing the five conservative variables, $\mathbf{F}^i$ are the flux vectors and $\mathbf{S}$ is the source vector, which does not contain derivatives of the state vector variables. The conservative formulation, which is also strongly hyperbolic, for the evolution equations helps with the numerical implementation. In effect, any finite differences algorithm will automatically conserve the conserved variables in the theory and, moreover, the numerical solution will converge to a weak solution of the system, if the code is in a convergent regime. The conserved variables of the Valencia formulation are:

$$\begin{pmatrix} D = \sqrt{\gamma} W \rho \\ S_j = \sqrt{\gamma} \rho h W^2 v_j \\ \tau = \sqrt{\gamma}(\rho h W^2 - p) - D \end{pmatrix}. \tag{3.57}$$

The corresponding fluxes are:

$$F^i = \begin{pmatrix} D(\alpha v^i - \beta^i) \\ S_j(\alpha v^i - \beta^i) + p\delta^i_j \tau(\alpha v^i - \beta^i) + p v^i \end{pmatrix} \tag{3.58}$$

And the source terms:

$$S = \begin{pmatrix} 0 \\ T^{\mu\nu}\left(\partial_\mu g_{\nu j} + \Gamma^\sigma_{\mu\nu} g_{\sigma j}\right) \\ \alpha\left(T^{\mu 0}\partial_\mu \log \alpha - T^{\mu\nu}\Gamma^0_{\nu\mu}\right) \end{pmatrix}. \tag{3.59}$$

The convergence to the right physical solution and conservation in the numerical evolution of the physically conserved variables is the most important requisite for the formulation of the hydrodynamics, but the ability to treat consistently solutions with shocks is another important one. In effect, any nonlinear, hyperbolic PDE can develop shocks even starting from smooth initial data. Hence, it is necessary to have a numerical algorithm that could be able to capture efficiently those shocks without crashing the code or loosing accuracy. The starting point is a finite-volume scheme, which helps emphasizing the conservation properties of the system and dealing with discontinuities. The main point is evolving, instead of the point-valued conserved variables $\mathbf{U}$, their volume average in a numerical cell

$$\bar{U} = \frac{1}{\Delta V}\int_{x^1}^{x^1+\Delta x^1}\int_{x^2}^{x^2+\Delta x^2}\int_{x^3}^{x^3+\Delta x^3} U dx^1 dx^2 dx^3. \tag{3.60}$$

Integrating equation (3.56) in a spatial numerical cell and using Gauss divergence theorem, one obtains

$$\begin{aligned} \partial_t \bar{U}(\vec{x}, t) = &-\frac{1}{\Delta x^1}\left(\bar{F}_{23}(x^1 + \Delta x^1) - \bar{F}_{23}(x^1)\right) + \\ &-\frac{1}{\Delta x^2}\left(\bar{F}_{13}(x^2 + \Delta x^2) - \bar{F}_{13}(x^2)\right) + \\ &-\frac{1}{\Delta x^3}\left(\bar{F}_{12}(x^3 + \Delta x^3) - \bar{F}_{12}(x^3)\right) \end{aligned} \tag{3.61}$$

where $\bar{F}_{ij}$ is the surface average of the flux $\mathbf{F}$ on the i, j boundary face of the numerical volume, defined as

$$\bar{F}_{ij}(x^k) = \int_{x^i}^{x^i+\Delta x^i} \int_{x^j}^{x^j+\Delta x^j} F(\tilde{x}^i, \tilde{x}^j x^k) d\tilde{x}^i d\tilde{x}^j. \tag{3.62}$$

The key idea of the shock-capturing algorithm adopted in `GRHydro`, which is the so called "Godunov method" [110], can be expressed by integrating equation (3.61) also in time in the arbitrary interval $[t_n, t_{n+1}]$:

$$\begin{aligned} \bar{U}_{ijk}(t^{n+1}) = \bar{U}_{ijk}(t^n) + \frac{\Delta t}{\Delta x^i}\left(\hat{F}_{i+1/2jk} - \hat{F}_{ijk}\right) + \frac{\Delta t}{\Delta x^j}\left(\hat{F}_{ij+1/2k} - \hat{F}_{ijk}\right) + \\ + \frac{\Delta t}{\Delta x^k}\left(\hat{F}_{ijk+1/2} - \hat{F}_{ijk}\right) + \int S d^3x dt, \end{aligned} \tag{3.63}$$

where $\hat{F}_{ijk}$ is the *numerical flux function*:

$$\hat{F}_{ijk} = \frac{1}{\Delta t} \int_{t^n}^{t^{n+1}} \bar{F}_{ijk} dt. \tag{3.64}$$

The idea expressed in equation (3.63) is a recipe to evolve forward in time the hydrodynamical conserved variables, but it is not (yet) a numerical scheme, since it is just an analytical expression obtained without any approximation. In effect, one needs to know the time-averaged flux $\hat{F}$ on each surface of the considered cell boundary, which depends on the solution for conserved variables at times $t > t^n$. It is then necessary to have an approximation for $\hat{F}$, which is robust to the presence of shocks in the solution. The idea that can be found in Godunov's work is that of computing $\hat{F}$ using the solution of a one dimensional Riemann problem at each boundary in each Cartesian direction. The Riemann problem is given by a one dimensional conservation-form hyperbolic PDE similar to equation (3.56), but with no source terms. The initial conditions around the separation surface $x = x_0$ are:

$$\bar{U}(x, t_0 = 0) = \begin{Bmatrix} U_L & \text{if} & x < x_i \\ U_R & \text{if} & x > x_i \end{Bmatrix} \tag{3.65}$$

A characteristic of the Riemann problem is that it is invariant under similarity transformations:

$$(x, t) = (ax, at), \quad a > 0, \tag{3.66}$$

and its solution is self-similar and depends on the variable $\frac{x-x_0}{t-t_0}$.The typical solution of a Riemann problem for the hydrodynamics consists of constant states separated by rarefaction waves, shock waves (where all the hydrodynamical primitive variables are discontinuous) and contact discontinuities (where only the density is discontinuous, like at the neutron star surface). This imposes a Courant factor since the time step should be sufficiently small not to allow waves from neighbouring cells interfaces to interact:

$$\Delta t < \frac{\Delta x}{|v_{max}|}, \tag{3.67}$$

where v_{max} is the maximum wave speed in any point of the grid at a given time step. The original first-order Godunov's scheme used equation (3.63) for the time evolution using initial conditions given by a piecewise constant reconstruction.

However, in order to go beyond first-order convergence, it is necessary to adopt a *High Resolution Shock Capturing* scheme (HRSC). First, one can approximate cell volume averages $\bar{U}$ and face surface averages $\bar{F}$ with their point-values at the numerical grid cell and face centers. The error made with this approximation is proportional to $(\Delta x)^2$. All finite volume codes, which is also the case of `GRHydro`, uses this approach.

To increase the temporal resolution in HRSC schemes, it is used the Method of Lines (see the beginning of this chapter) starting from equation (3.61). The flux terms $\hat{F}$ are computed as solutions of a Riemann problem also in this case since they are guaranteed to be constant in time at the cell interface $x = x_0$. A common choice for the evolution of the hydrodynamical variables is the fourth order RK method, which also allow to have lower errors since it is the same method used for the spacetime.

Spatial resolution can be improved beyond first order using reconstruction methods that allow to compute the initial values U_L and U_R for the Riemann problem. The common strategy used by this methods is the reconstruction of the internal profile of primitive variables inside each numerical cell with a polynomial interpolation. From these profiles, one can calculate the limits at the cell boundaries P_L and P_R and from them also the corresponding conserved variables. The reconstructions are supplemented with some kind of limiter, which limits the reconstruction profile slope, reducing the method to first order near shocks. In this way, the limitations of Godunov's theorem, which states that any linear, higher than first order, reconstruction method may induce spurious oscillations near shocks, are overcome.

In particular, in this section we will discuss some of the reconstruction methods implemented by the `Einstein Toolkit`, which are the Piecewise Parabolic method (PPM) [111], third order convergent, the Monotonicity Preserving method (MP5) [112], fifth order, and the Weighted Essentially Non Oscillatory method (WENO) [113, 114], also fifth order. It was shown in [64] that the WENO reconstruction method is the best for achieving global second order convergence even at very poor resolutions.

To summarize this section, the evolution of the GR(M)HD equations in the `Einstein Toolkit` proceeds as follows:

1. Computation of the source terms from the primitive variables at the cells centers;

2. Reconstruction of the primitive variables to the left and right states near the cell faces;
3. Computation of the conserved variables from the reconstructed primitives with simple algebraic expressions;
4. The Riemann solver finds an approximate solution to the Riemann problem at each interface, using the conserved variables right and left as initial conditions. The Riemann problem is solved independently along each spatial directions, finding all flux components;
5. From the source and flux terms, the right hand sides for the `MoL` time evolution is build;
6. At the same time, the energy-momentum tensor is constructed from the primitive variables at the cell centers, which is the the starting point for computing the right hand sides of BSSN-OK evolution equations;
7. Evolution of both the hydrodynamical conserved variables and curvature variables with a fourth-order Runge-Kutta method;
8. Computation of the new time-step primitive variables from the cell centers values of the conserved variables, using a root-finding procedure.

3.2.1 Reconstruction methods

PPM

The PPM method is the first reconstruction method that was tried and it is a very common choice for numerical relativity codes, especially in single-star simulations. The original algorithm of the PPM method is slightly modified in the `GRHydro` thorn, where a formulation specialised to evenly-spaced grids is adopted, using the simplest dissipation algorithm and an approximated flatted algorithm which needs only three stencil points instead of four.

The base idea of the PPM reconstruction is the interpolation of the reconstructed primitive variable a with a quadratic polynomial:

$$a_{i+1/2} = \frac{1}{2}(a_{i+1} + a_i) + \frac{1}{6}(\delta a_i - \delta_{i+1}), \tag{3.68}$$

where δa_i is given by the approximation:

$$\delta a_i = \min\left(\frac{1}{2}|a_{i+1} - a_{i-1}|, 2|a_{i+1} - a_i|, 2|a_i - a_{i-1}|\right) \cdot \operatorname{sign}(a_{i+1} - a_{i-1}) \tag{3.69}$$

when

$$(a_{i+1} - a_i)(a_i - a_{i-1}) > 0 \tag{3.70}$$

and is zero otherwise.

After this step, the right and left states are equal $a_i^R = a_{i+1}^L = a_{i+1/2}$, and the solution will be third order convergent in space for smooth flows. However, this is not strictly monotonicity preserving since new extrema, that are not extrema of the original variable profile, can be created. In particular, this can happen when a_i is a local maximum or minimum or when it is close to one of the reconstructed face averages. In such cases, the variables are modified in this way:

$$a_i^L = a_i^R = a_i \quad \text{if} \quad (a_i^R - a_i)(a_i - a_i^L) \leq 0 \tag{3.71}$$

$$a_i^L = 3a_i - 2a_i^R \quad \text{if} \quad (a_i^R - a_i^L)\left(a_i - \frac{1}{2}(a_i^R + a_i^L)\right) > \frac{1}{6}(a_i^R - a_i^L)^2 \tag{3.72}$$

$$a_i^R = 3a_i - 2a_i^L \quad \text{if} \quad (a_i^R - a_i^L)\left(a_i - \frac{1}{2}(a_i^R + a_i^L)\right) < -\frac{1}{6}(a_i^R - a_i^L)^2. \tag{3.73}$$

Two additional steps may be applied before the monotonicity preserving procedure: the first step is the steepening of the contact discontinuities, in order to ensure sharp solution profiles; then a flattening procedure near shocks is applied to reduce the convergence in that case towards first order (locally), and avoid oscillations in the solution. Therefore, the reconstructed variables are modified as follows:

$$a_i^{L,R} = \nu_i a_i^{L,R} + (\nu_i) a_i, \tag{3.74}$$

where ν_i is an additional advection velocity that produces extra dissipation needed for avoiding oscillation near shocks. It is defined as:

$$\nu_i = \max\left(0, 1 - \max\left(0, \omega_2\left(\frac{p_{i+1} - p_{i-1}}{p_{i+2} - p_{i-2}} - \omega_1\right)\right)\right), \tag{3.75}$$

and, instead, $\nu_i = 1$ in smooth flows. The criteria for detecting shocks in this case are:

$$\omega_0 \min\left(p_{i-1}, p_{i+1}\right) < |p_{i+1} - p_{i-1}| \quad \textbf{and} \quad v_{i-1}^x - v_{i+1}^x > 0. \tag{3.76}$$

As mentioned before, this version is a bit different than the original one of [111], but requires only 3 stencil points instead of four, which would considerably increase the computational cost, especially when using mesh refinement.

MP5

Another reconstruction method that is often used in numerical simulations is the MP5 method. In the presentation paper of `GRHydro` [104], it was found that this method was the most accurate for a simple single TOV star test. MP5 is based on a fifth-order polynomial interpolation, followed by a limiter that allows to keep high order convergence also near solution extrema, distinguishing them from shocks, which is not possible in the PPM method. It does also preserve the monotonicity when adopting a Runge-Kutta scheme for the time evolution. The interpolation for MP5 is given by:

$$a^L_{i+1/2} = \frac{1}{60}(2a_{i-2} - 13a_{i-1} + 47a_i + 27a_{i+1} - 3a_i + 2). \tag{3.77}$$

If a limiter is applied, the condition is:

$$\begin{aligned} \left(a^L_{i+1/2} - a_i\right)\left(a_{i+1/2} - a^{\mathrm{MP}}\right) &\leq 0 & (3.78)\\ a^{\mathrm{MP}} &:= a_i + \mathrm{minmod}\left(a_{i+1} - a_i, \alpha(a_i - a_{i-1})\right), & (3.79)\end{aligned}$$

where $\alpha = 4$ is used. The minmod limiter function is given by:

$$\begin{aligned} \mathrm{minmod}(x, y) &= \frac{1}{2}\left(\mathrm{sign}(x) + \mathrm{sign}(y)\right)\min\left(|x|, |y|\right) & (3.80)\\ \mathrm{minmod}(w, x, y, z) &= \frac{1}{8}\left(\mathrm{sign}(w) + \mathrm{sign}(x)\right) \times & (3.81)\\ &\times \left|\left(\mathrm{sign}(w) + \mathrm{sign}(y)\right)\left(\mathrm{sign}(w) + \mathrm{sign}(z)\right)\right| \times \\ &\times \min\left(|w|, |x|, |y|, |z|\right). \end{aligned}$$

A limiter is applied, if equation (3.78) is satisfied. In order to set it, one builds four combination of the interpolated variable:

$$\begin{aligned} a^{\mathrm{AV}} &= \frac{1}{2}(a_i + a_{i+1}) & (3.82)\\ a_{\mathrm{UL}} &= a_i + \alpha(\alpha_i - a_{i+1}) & (3.83)\\ a_{\mathrm{MD}} &= a_{\mathrm{AV}} - \frac{1}{2}D^{\mathrm{M4}}_{i+1/2} & (3.84)\\ a_{\mathrm{LC}} &= a_i + \frac{1}{2}(a_i - a_{i-1}) + \frac{4}{3}D^{\mathrm{M4}}_{i-1/2}, & (3.85)\end{aligned}$$

where a^{AV} stands for **AV**erage, a^{UL} for **U**pper **L**imit, a^{MD} for **M**e**D**ian and a a^{LC} for **L**arge **C**urvature. $D^{\mathrm{M4}}_{i\pm1/2}$ are build starting from finite-difference expression of the second derivatives of the reconstructed fields:

$$\begin{aligned} D^-_i &= a_{i-2} - 2a_{i-1} + a_i & (3.86)\\ D^0_i &= a_{i-1} - 2a_i + a_{i+1} & (3.87)\\ D^+_i &= a_i - 2a_{i+1} + a_{i+2} & (3.88)\\ D^{\mathrm{M4}}_{i+1/2} &= \mathrm{minmod}(4D^0_i - D^+_i, 4D^+_i - D^0_i, D^0_i, D^+_i) & (3.89)\\ D^{\mathrm{M4}}_{i-1/2} &= \mathrm{minmod}(4D^0_i - D^-_i, 4D^-_i - D^0_i, D^0_i, D^-_i). & (3.90)\end{aligned}$$

Hence, the limited reconstructed variable can be written as

$$a^L_{i+1/2} = a^L_{i+1/2} + \mathrm{minmod}\left(a_{\min} - a^L_{i+1/2}, a_{\max} - a^L_{i+1/2}\right), \tag{3.91}$$

where

$$a_{\min} = \max\left(\min\left(a_i, a_{i+1}, a^{\mathrm{MD}}\right), \min\left(a_i, a^{\mathrm{UL}}, a^{\mathrm{LC}}\right)\right) \tag{3.92}$$
$$a_{\max} = \min\left(\max\left(a_i, a_{i+1}, a^{\mathrm{MD}}\right), \min\left(a_i, a^{\mathrm{UL}}, a^{\mathrm{LC}}\right)\right). \tag{3.93}$$

The variables at the right interface can be computed using the same algorithm but substituting $\{a_{i-2}, a_{i-1}, a_i, a_{i+1}, ai + 2\}$ with $\{a_{i+2}, a_{i+1}, a_i, a_{i-1}, a_{i-2}\}$.

WENO

The WENO reconstruction method is essentially an improvement on the Essentially Non Oscillatory (ENO) method. The original ENO method uses two interpolation polynomials with different stencils, then, based on the smoothness, one of the two are selected in order to avoid the one containing the discontinuous solutions near shocks. This allows to keep high order convergence even near shocks and local extrema, which is not possible when dealing with single stencil methods with limiters like PPM and MP5. The idea behind the WENO method is to combine all the possible ENO reconstruction stencils, each weighted accordingly, with weight that goes to zero in the case of a discontinuity present in the corresponding stencil:

$$a^{L,1}_{i+1/2} = \frac{3}{8}a_{i-2} - \frac{5}{4}a_{i-1} + \frac{15}{8}a_i \tag{3.94}$$
$$a^{L,2}_{i+1/2} = -\frac{1}{8}a_{i-1} + \frac{3}{4}a_i - \frac{3}{8}a_{i+1} \tag{3.95}$$
$$a^{L,3}_{i+1/2} = \frac{3}{8}a_i + \frac{3}{4}a_{i+1} - \frac{1}{8}a_{i+2}. \tag{3.96}$$

These approximations are all third-order convergent, but combining them in a appropriate way, spanning all the 5 point stencil from a_{i-2} to a_{i+2}, one obtains an object that is fifth-order convergent, when the weights w^i are all different to zero:

$$a^{L}_{i+1/2} = w^1 a^{L,1}_{i+1/2} + w^2 a^{L,2}_{i+1/2} + w^3 a^{L,3}_{i+1/2}. \tag{3.97}$$

WENO weights have sum one, since $\sum_i w^i = 1$ and are chosen from the so called *smoothness indicators* β^i:

$$\beta^1 = \frac{1}{3}\left(4a^2_{i-2} - 19a_{i-2}a_{i-1} + 25a^2_{i-1} + 11a_{i-2}a_i - 31a_{i-1}a_i + 10a^2_i\right) \tag{3.98}$$
$$\beta^2 = \frac{1}{3}\left(4a^2_{i-1} - 13a_{i-1}a_i + 13a^2_i + 5a_{i-1}a_{i+1} - 13a_i a_{i+1} + 4^2_{i+1}\right) \tag{3.99}$$
$$\beta^3 = \frac{1}{3}\left(10a^2_i - 31a_i a_{i+1} + 25a^2_{i+1} + 11a_i a_{i+2} - 19a_{i+1}a_{i+2} + 4a^2_{i+2}\right). \tag{3.100}$$

The weights are then obtained as follows:

$$w^i = \frac{\bar{w}^i}{\sum_i \bar{w}^i} \tag{3.101}$$

$$\bar{w}^i = \frac{\gamma^i}{(\epsilon + \beta^i)^2} \tag{3.102}$$

$$\gamma^i = \left\{ \frac{1}{16}, \frac{5}{8}, \frac{5}{16} \right\}. \tag{3.103}$$

The main issue with this weights is that ϵ is scale-dependent, and setting a fixed value for it could lead to problems in simulating physical systems with a large variation in relevant scales (such as problems with turbulence or instabilities). A solution that is adopted also in `GRHydro` is using modified smoothness indicators, which depend on the scale of the reconstructed field, measured by its L^2 norm in the considered stencil $\parallel a^2 \parallel$. The new indicators are:

$$\bar{\beta}^i = \beta^i + \epsilon \left(\parallel a^2 \parallel +1 \right). \tag{3.104}$$

The default value of ϵ in `GRHydro` is 1×10^{-26}. Before it was mentioned that a stencil weight will go to zero (and the corresponding smoothness indicator will tend to infinity) when a discontinuity in the reconstructed field is present in its points, reducing the convergence order adaptively when needed, but keeping at least third order convergence near shocks.

3.2.2 The Riemann solver

The simulations that will be presented in chapter 4 have been performed using the approximate Riemann solver from Harte, Lax, van Leer and Einfeldt (HLLE) [115, 116]. The advantage of this solver is that it is not computationally expensive, it is robust (in [117] a comparison between HLLE and Marquina is presented, showing that HLLE avoid constraint violations at the boundary of EOS polytropic pieces) and it is the only Riemann solver in `GRHydro` already extended for GRMHD evolution, making it easier to develop a follow-up project that includes magnetic fields. The approach of the HLLE Riemann solver is based on the use of two wave approximations, considering the maximum and minimum wave speeds V_+ and V_- at both sides of an interface, which generate a single state between them. For a conserved variable U in a point labelled by the variable $\xi = \frac{x - x_{\text{interface}}}{\Delta t}$, the Riemann problem is then:

$$U = \begin{cases} U_L & \text{if} \quad \xi < V_- \\ U^{\text{HLLE}} & \text{if} \quad V_- < \xi < V_+ \\ U_R & \text{if} \quad \xi < V_+ \end{cases} \tag{3.105}$$

The intermediate state U^{HLLE} can be computed starting from the one dimensional form of equation (3.63) in a control volume around the cell interface:

$$\int_{x_L}^{x_R} U(x,t+\Delta t)dx = \int_{x_L}^{x_R} U(x,t)dx + \int_{t}^{t+\Delta t} F(U(x_L,t'))dt' + \\ - \int_{t}^{t+\Delta t} F(U(x_R,t'))dt'. \quad (3.106)$$

Using the reconstructed variables U_L and U_R and the corresponding fluxes F_L and F_R one can evaluate the right hand side as:

$$\int_{x_L}^{x^R} U(x,t+\Delta t)dx = x_R U_R - x_L U_L + \Delta t(F_L - F_R). \quad (3.107)$$

However, the left hand side can be divided into three parts: one on the left of the fastest left-going wave, one between the two waves and one at the right of the fastest right-going wave. Therefore:

$$\begin{aligned}\int_{x_L}^{x_R} U(x,t+\Delta t)dx = &\int_{x_L}^{\Delta t V^-} U(x,t+\Delta t)dx + \int_{\Delta t V^-}^{\Delta t V^+} U(x,t+\Delta t)dx + \\ &+ \int_{\Delta t V^+}^{x_R} U(x,t+\Delta t)dx = \\ &= \int_{\Delta t V^-}^{\Delta t V^+} U(x,t+\Delta t)dx + (\Delta t V^- - x_L)U_L + \\ &+ (x_R - \Delta t V^+)U_R \end{aligned} \quad (3.108)$$

Using this equation in equation (3.107) and dividing both terms by $\Delta t(V^+ - V^-)$ finally one gets the expression for the average exact Riemann problem solution between the slowest and fastest wave at $t+\Delta t$, which is the definition for the HLLE intermediate state:

$$U^{\text{HLLE}} = \frac{1}{\Delta t(V^+ - V^-)} \int_{\Delta t V^-}^{\Delta t V^+} U(x,t+\Delta t)dx = \frac{V^+ U_R - V^- U_L + F_L - F_R}{V^+ - V^-}. \quad (3.109)$$

In order to get the corresponding numerical fluxes from those solutions, it is necessary to invoke the *Rankine-Hugoniot* condition: given a shock along $s(t)$ with speed $V = \frac{\mathrm{d}s(t)}{\mathrm{d}t}$, its fluxes are related with its states by

$$F(U(s_L,t)) - F(U(s_R,t)) = V(U(s_L,t)) - U(s_R,t). \quad (3.110)$$

Applying this condition to (3.105), between the left and the intermediate state, or between the intermediate and the right state, one obtains two equivalent expressions for the HLLE numerical fluxes:

$$\begin{aligned} F^{\text{HLLE}} &= F_L + V^-(U^{\text{HLLE}} - U_L) \\ F^{\text{HLLE}} &= F_R + V^+(U_R - U^{\text{HLLE}}). \end{aligned} \quad (3.111)$$

Substituting the expression found in (3.107), one founds:

$$F^{\text{HLLE}} = \frac{V^+ F_L - V^- F_R + V^+ V^- (U_R - U_L)}{V^+ - V^-}. \tag{3.112}$$

At this point it is necessary to be able to compute the minimum and the maximum wave speeds in order to get a numerical flux. In `GRHydro` this is achieved computing the maximum and the minimum between the analytically computed eigenvalues of the GRHD system of equations using the reconstructed states. The eigenvalues are [106]:

$$\lambda_0 = \alpha v^i - \beta^i (\text{triple}) \tag{3.113}$$

$$\lambda_\pm = \frac{\alpha}{1 - v^2 c_s^2} \left[v^i (1 - c_s^2) \pm c_s \sqrt{(1 - v^2)(\gamma^{ii}(1 - v^2 c_s^2) - v^i v^i (1 - c_s^2))} \right] - \beta^i, \tag{3.114}$$

where $c_s^2 = \frac{\partial p}{\partial \rho}$ is the sound speed.

3.2.3 Conservative to primitive conversion (`Con2Prim`)

At each step, it is necessary to recover primitive variables from the evolved conserved ones in order to be able to start the next time-evolution step, constructing the energy-momentum tensor and reconstructing hydrodynamical variables at cell interfaces, which cannot be done analytically. The procedure is analogue to the one used to convert from primitives to conservatives where a one-dimensional Newton-Raphson procedure to recover the unknown pressure is required.

The first step include the computation of the undensitised conserved variables:

$$\hat{D} = \frac{D}{\sqrt{\gamma}} = \rho W \tag{3.115}$$

$$\hat{S}_i = \frac{S_i}{\sqrt{\gamma}} = \rho h W^2 v_i \tag{3.116}$$

$$\hat{\tau} = \frac{\tau}{\sqrt{\gamma}} = \rho h W^2 - P - \hat{D}. \tag{3.117}$$

The two additional variables are introduced:

$$Q := \rho h W^2 = \hat{\tau} + \hat{D} + P \tag{3.118}$$

$$\hat{S}^2 := \gamma_{ij} \hat{S}^i \hat{S}^j = (\rho h W)^2 (W^2) - 1, \tag{3.119}$$

where $\hat{S}^2$ is known from the evolved variables and Q depends only on the unknown pressure P. Given these expressions, one can construct the primitive variables ρ and ϵ that only depend on P:

$$\rho = \frac{\hat{D}\sqrt{Q^2 - \hat{S}^2}}{Q} \tag{3.120}$$

$$\epsilon = \frac{\sqrt{Q^2 - \hat{S}^2} - PW - \hat{D}}{\hat{D}}, \tag{3.121}$$

and the Lorenz factor W can be written as:

$$W = \frac{Q}{\sqrt{Q^2 - \hat{S}^2}}. \tag{3.122}$$

The new density and specific energy density can be computed given an initial guess for the new pressure. Then, using the EOS, one can compute also a pressure value $P(\rho, \epsilon)$. Iterating the Newton-Raphson method, one can minimize the residual between the pressure value used to compute ρ and ϵ and the one obtained with the subsequent EOS call. For this method, it is required to know the derivatives of the pressure, in particular $\frac{\partial P}{\partial \rho}$ and $\frac{\partial P}{\partial \epsilon}$, which are given, again, by the EOS. The `Con2Prim` routines are then responsible to check if the resulting values are actually physical.

3.3 Initial data computation

The problem of generating accurate initial data for binary neutron stars in quasi-circular orbits is non-trivial, but is necessary for the fully dynamical evolution. For the simulations that will be displayed in chapter 4, it was used the only publicly available code for BNS initial data, the `LORENE` library [21, 22].

Binary neutron stars are believed to be in circular orbits prior to the merger, thanks to the circularization properties of the emitted gravitational radiation. They are also likely to be irrotational, since the viscous contribution is too weak and act on a time-scale that is too long respect to the gravitational radiation in order to be able to successfully synchronize stars spins with the orbital rotation. The starting point of the computation of initial data for such systems, is, therefore, the assumption of the existence of a *helicoidal* Killing vector, which, for an asymptotic inertial observer at rest respect to the binary system, takes the form

$$I = \frac{\partial}{\partial t} + \Omega \frac{\partial}{\partial \phi}. \tag{3.123}$$

This assumption implies that we are ignoring the outgoing gravitational radiation, and its backreaction on the binary dynamics. This is responsible for the lack of a radial component of the star velocity and for the small orbital eccentricity once the data are evolved (see section 4.1.1 of [35]). Another implication of the helicoidal symmetry is that it leads to a non-asymptotically flat spacetime. In order to avoid diverging metric coefficients at infinity, one should make appropriate approximations in the curvature evolution. A common approach that is used in the LORENE code and in most of the private code developed in the last years [118, 119], is the *Conformal Thin Sandwich* approach, based on the Wilson and Matthews scheme [120]. In the 3+1 formulation of general relativity presented in 3.1, the spatial metric is approximated as conformally flat:

$$\gamma_{ij} = A^2 \eta_{ij}. \tag{3.124}$$

This justification of this choice comes from the fact that it would be exact for spherically-symmetric spacetimes, and it is a good and commonly used approximation for constructing axisymmetric isolated neutron stars initial data, and it is a good description of BNS spacetime when the stars are far apart. Another simplification could be building the building a coordinate frame compatible with the helicoidal symmetry, where $I = \frac{\partial}{\partial t}$. The corotating shift is defined as:

$$\omega^i = \beta^i + \Omega \frac{\partial}{\partial \phi}. \tag{3.125}$$

Using the Killing equation

$$\nabla_\mu I_\nu + \nabla_\nu I_\mu = 0 \tag{3.126}$$

one can construct a relation for the extrinsic curvature K^{ij}:

$$\begin{aligned} K^{ij} &= -\frac{1}{2\alpha}\left(\nabla^i \beta^j + \nabla^j \beta^i\right) \\ &= -\frac{1}{2A^2\alpha}\left(\partial^i \omega^j + \partial^j \omega^i - \frac{2}{3}\eta^{ij}\partial_k \omega^k\right). \end{aligned} \tag{3.127}$$

Thanks to helicoidal symmetry, this relationship fixes all spatial components of the extrinsic curvature, which also means fixing equation (3.29) of the ADM formulation, leaving a free choice only for its trace K (which is fixed by the maximal slicing gauge condition). Considering the Hamiltonian and momentum constraints and the trace of the Einstein equation, one obtains five elliptic equation to be solved for the variables ω^i, A and α. In the LORENE code, the following variables are used instead:

$$\nu := \ln(\alpha) \tag{3.128}$$

$$\beta := \ln(\alpha A), \tag{3.129}$$

and finally the equations obtained are:

$$\nabla^2 \nu = 4\pi A^2 (e + S) + A^2 K^{ij} K_{ij} - \partial_i \nu \partial^i \beta \tag{3.130}$$

$$\nabla^2 \beta = 4\pi A^2 S + \frac{3}{4} A^2 K_{ij} K^{ij} - \frac{1}{2}(\partial_i \nu \partial^i \nu + \partial_i \beta \partial^i \beta) \tag{3.131}$$

$$\nabla^2 \omega^i + \frac{1}{3}\partial^i \partial_j \omega^j = -16\pi \alpha A^2 j^i + 2\alpha A^2 K^{ij} \partial_j (3\beta - 4\nu), \tag{3.132}$$

where all Laplacians are computed respect to the flat spatial metric. The remaining Einstein equations are not considered in this scheme, meaning that this is only an approximation of a true BNS spacetime.

The initial hydrodynamics of a BNS system is done trading the energy-momentum tensor and baryon number conservation with the following *uniformly canonical equations of motion*:

$$u^\mu(\nabla \times \mathbf{w})_{\mu\nu} = 0 \tag{3.133}$$

$$\nabla^\mu(\rho u_\mu) = 0 \tag{3.134}$$

where $w_\mu = hu_\mu$ is the comomentum 1-form and its exterior derivative

$$(\nabla \times \mathbf{w})_{\mu\nu} = \nabla_\mu w_\nu - \nabla_\nu w_\mu \tag{3.135}$$

is the vorticity two-form. A possible solution to (3.133) for which $(\nabla\times\mathbf{w})_{\mu\nu} = 0$ is the *potential flow*:

$$w_\mu = \nabla_\mu \psi. \tag{3.136}$$

This is the generalization of a Newtonian irrotational flow in general relativity. The helicoidal symmetry implies that $\mathcal{L}_I w = 0$ and using Cartan's identity this becomes:

$$I^\mu(\nabla \times \mathbf{w})_{\mu\nu} + \nabla^\mu(I^\nu w_\nu) = 0 \tag{3.137}$$

where $I^\nu w_\nu = \text{const}$ and is a constant of motion. Therefore, the fluid motion is completely determined by the potential ψ, which must satisfy equation (3.134):

$$\frac{\rho}{h}\nabla^\mu\nabla_\mu\psi + \nabla^\mu\psi\nabla_\nu\left(\frac{\rho}{h}\right) = 0 \tag{3.138}$$

In the 3+1 formulation of GR, this equation becomes the following elliptic Poisson-like equation on every hypersurface Σ_t:

$$\begin{aligned}\rho\partial_i\partial^i\psi + \psi^i\rho\partial_i\psi = -\frac{hW}{\alpha}\beta^i\partial_i\rho + \rho\Bigg[&\left(\partial^i\psi + \frac{hW}{\alpha}\beta^i\right)\partial_i \ln(h) + \\ &- \partial^i\psi\partial_i\alpha - \frac{\beta^i}{\alpha}\partial_i(hW)\Bigg] + K\rho hW.\end{aligned} \tag{3.139}$$

To conclude, BNS initial data are computed solving equations (3.130), (3.131), (3.132) and (3.139) using appropriate asymptotic flatness boundary conditions at large radii:

$$\alpha \to 1 \tag{3.140}$$

$$\psi \to 1 \tag{3.141}$$

$$\omega^i \to \omega \times \vec{r}. \tag{3.142}$$

In LORENE this is done using an iterative procedure, based on a multidomain spectral method. The methods and the numerical parameters chosen for the initial data that will be presented in 4 have already been discussed in [35].

3.4 Gravitational-wave signal extraction from simulations

For BNS system, the physical setting is different from the one of the simple linearized gravity described in section 2.3. In effect, the central source is made of compact objects that generate a strong gravitational field and a solution of full non-linear Einstein's equations are needed. Therefore, the quadrupole formula of equation (2.46), is not the best tool to compute the gravitational wave strain emitted by the simulated system, since it leads to a big uncertainty in the waves amplitude [121, 122]. The two most common techniques used to extract gravitational waves from numerical simulations are the Newmann-Penrose scalar Ψ_4, or the Regge-Wheeler-Zerilli (see [123, 124] for the details) theory of metric perturbations of the Schwarzschild spacetime.

The first technique is based on the Newman-Penrose (or Weyl) scalars, which are defined starting from the Weyl tensor [125]

$$C_{\alpha\beta\mu\nu} = R_{\alpha\beta\mu\nu} - g_{\alpha[\mu}R_{\nu]\beta} + g_{\beta[\mu}R_{\nu]\alpha} + \frac{1}{3}g_{\alpha[\mu}g_{\nu]\beta}R \tag{3.143}$$

and contracting it with an orthonormal null tetrad l^μ. n^μ, m^μ, $\bar{m}^\mu$, where $\bar{m}^\mu$ is the complex conjugate of m^μ and the following relations apply:

$$l^\mu l_\mu = n^\mu n_\mu = m^\mu m_\mu = 0 \tag{3.144}$$

$$m^\mu n_\mu = m^\mu l_\mu = 0 \tag{3.145}$$

$$l^\mu n_\mu = -1. \tag{3.146}$$

This tetrad is constructed starting from a orthonormal regular tetrad on Σ_t, based on spherical coordinates $(e_r)^i$, $(e_\theta)^i$, $(e_\phi)^i$. The direction along which the outgoing gravitational waves are propagated is along the surface radial coordinate r, for which the two-surfaces $r = t =$ const have area $4\pi r^2$. This is the radial Schwarzschild coordinate in a non-spinning background. Differently, the radial coordinate R of the coordinate system used in most cases in numerical relativity (selected using the gauge conditions in (3.44) and (3.45)) is not a surface radial coordinate, and asymptotically is close to the *isotropic* radial coordinate, linked with r by:

$$r = R\frac{1 + (M + a)}{2R}\frac{1 + (M - a)}{2R}, \tag{3.147}$$

where a is the Kerr parameter $a = J/M$ (which is equal to zero in the non-rotating limit). In this case M is the total ADM mass of the system and J is the total ADM angular momentum.

The most common choice for the null tetrad [126, 127] in numerical relativity, which is also implemented in the `WeylScalar4` thorn of the `Einstein`

`Toolkit` is:

$$\mathbf{l} := \frac{1}{\sqrt{2}}(\mathbf{e}_t - \mathbf{e}_R) \tag{3.148}$$

$$\mathbf{n} := \frac{1}{\sqrt{2}}(\mathbf{e}_t + \mathbf{e}_R) \tag{3.149}$$

$$\mathbf{m} := \frac{1}{\sqrt{2}}(\mathbf{e}_\theta - i\mathbf{e}_\phi) \tag{3.150}$$

Once the null tetrad is defined, the Newmann-Penrose scalars are:

$$\Psi_0 = -C_{\alpha\beta\mu\nu} n^\alpha m^\beta n^\mu m^\nu \tag{3.151}$$

$$\Psi_1 = -C_{\alpha\beta\mu\nu} n^\alpha l^\beta n^\mu l^\nu \tag{3.152}$$

$$\Psi_2 = -C_{\alpha\beta\mu\nu} n^\alpha m^\beta \bar{m}^\mu l^\nu \tag{3.153}$$

$$\Psi_3 = -C_{\alpha\beta\mu\nu} n^\alpha l^\beta \bar{m}^\mu l^\nu \tag{3.154}$$

$$\Psi_4 = -C_{\alpha\beta\mu\nu} l^\alpha \bar{m}^\beta l^\mu \bar{m}^\nu . \tag{3.155}$$

The most important is Ψ_4 since its asymptotic limit for $r \to \infty$ describes the gravitational radiation:

$$\Psi_4 = \ddot{h}_+ - i\ddot{h}_\times := \ddot{\bar{h}}, \tag{3.156}$$

where h is the complex gravitational wave strain $h = h_+ + ih_\times$ from now on. The numerical implementation that allows to obtain Ψ_4, computes the Newman-Penrose (NP) scalar in (3.155) in a spherical surface far from the sources and then expands it in spin-weighted spherical harmonics of weight -2:

$$\Psi_4(t, R, \theta, \phi) = \sum_{l=2}^{l_{\max}} \sum_{m=-l}^{l} \Psi_4^{lm}(t, R)_{-2}Y^{lm}(\theta, \phi). \tag{3.157}$$

This is done by the `Multipole` thorn in the `Einstein Toolkit`.

Thanks to the *peeling theorem*, the NP scalars have the property of falling off for $r \to \infty$ as r^{n-5} in asymptotically flat spacetimes For this reason, the results are often reported for $r\Psi_4$ (and consequently rh) since Ψ_4 falls off as $\frac{1}{r}$, which is necessary when comparing signals extracted at different radii. Another necessary operation is to express GW signals in function of the retarded time (the time respect to the one in which the signal reaches the "detector" sphere). In order to compute the retarded time, one makes the assumption that the metric far from the sources is approximately the Schwarzschild one, and obtains:

$$t_{\text{ret}} = t - R^* \tag{3.158}$$

$$R^* = R + 2M \log\left(\frac{R}{2M} - 1\right), \tag{3.159}$$

where M is the system ADM mass and R^* is known as the tortoise coordinate. All the GW results presented in this thesis are reported using the retarded time, unless otherwise is specified.

The two main difficulties in using a GW extraction method that is based on the Ψ_4 scalar, are the necessity of extrapolating the results to spatial infinity, for equation (3.156) to hold, and performing the double time integration to get gravitational wave strain (see section 3.4.1).

3.4.1 Integration of Ψ_4 signal

The simplest way of integrating the Ψ_4 signal to get GW strain is to numerically compute the double time integration, for instance with the trapezoidal rule, and then set the two unknown integration constant that comes from the calculations, fitting the resulting strain with a first order polynomial and subtracting it to the strain itself:

$$\bar{h}^{(0)}_{lm}(t,r) = \int_0^t dt' \int_0^{t'} dt" \Psi_4^{lm}(t", r) \tag{3.160}$$

$$\bar{h}_{lm}(t,r) = \bar{h}^{(0)}_{lm} - Q_1 t - Q_0, \tag{3.161}$$

where the natural interpretation of the fitted parameters is

$$Q_1 = \left.\frac{\partial \bar{h}}{\partial t}\right|_{t=0} \tag{3.162}$$

$$Q_0 = \bar{h}(t=0). \tag{3.163}$$

The important thing to note regarding equation (3.160) is that the integration starts from the coordinate time $t = 0$ and not from the retarded time $t_{\rm ret} = 0$. It was found that the "more natural" use of retarded time in the integration leads to oscillations in the first few milliseconds of the strain signal, which is in accordance with Appendix A of [128]. The reason of this behavior could be the lower values for the integration constants Q_0 and Q_1 when starting from $t = 0$, leading to lower values in the fit errors.

As shown with more details in [35], the integration procedure of equation (3.160) leads to the presence of unphysical oscillations and non-linear drifts in the resulting strain amplitude. As accurately documented in [129], this phenomenon was attributed to the presence of high-frequency noise aliased in the low-frequency Ψ_4 signal and amplified in the double integration process. A solution that has been adopted in [64], and was already proposed in [122], is to fit the integrated signal with higher-order polynomials, such as a second order one:

$$\bar{h}_{lm}(t,r) = \bar{h}^{(0)}_{lm} - Q_2 t^2 - Q_1 t - Q_0. \tag{3.164}$$

The additional constant Q_2 has no immediate physical interpretation, but it gets lower as the extraction radius increases, so a possible interpretation could be as a correction of finite-radius extraction errors. The process that has just been discussed, however, is satisfying only for the dominant strain component $h_{2,2}$, while it is not sufficient to treat the unphysical behaviors in the subdominant modes (see figure 3.1 of [35] for the explanation). For that reason, higher-order polynomials would be required, but this would not be justified from the mathematical point of view.

Chapter 4

What does the gravitational wave signal tell us about neutron stars?

After a long introduction on the subject of thesis thesis and a short overview on the numerical methods that have been used to perform numerical simulations of binary neutron stars, it is time to look at the features that BNS mergers highlights. All the following analyses are based on the numerical simulations that have been performed by the Parma numerical relativity group and presented in [36, 37, 38].

The general merger dynamics of a binary neutron star system can be divided into three phases:

1. The inspiral phase, where the two stars rotate fast one around the other, and their distance shrinks due to the loss of energy and angular momentum due to the emission of gravitational radiation. When the two stars are closer to the merger, the tidal deformation of each star due to the gravitational field of the companion becomes relevant, speeding up the GW phase evolution. For that reason, the GW signal emitted by BNS is significantly different from the black hole one, which can be predicted accurately using semi-analytical techniques based on post-Newtonian expansion. The analysis of the tidal effects of BNS in the inspiral phase is very important, because it brings a signature of the EOS, which influences the tidal deformability[130, 131, 132].

2. The merger phase, where the two stars finally come into contact, compressing matter and resulting in extremely complex hydrodynamical phenomena, such as Kevin-Helmoltz instability, which can strongly amplify magnetic fields, even if this would need an extremely high computational resolution in order to resolve it[133].

3. The post-merger phase, where the neutron star remnant during the merger evolves with a different phenomenology depending on its mass,

EOS and angular momentum distribution [32, 34]. The remnant star is bar-deformed, differential rotating, in the first part of this phase, then evolving into a more stable, uniformly rotating, configuration later. In particular, this phase of the merger dynamics can be subdivided into three more parts:

(a) The early post-merger phase(first ~ 10 ms after the merger), characterized by oscillational modes, interaction between the main quadrupolar mode and the quasi-radial oscillation of the remnant. The matter ejection due to the collision of the two stars is concentrated in this phase of the dynamics [37].

(b) The main post-merger phase, where the gravitational wave emission is dominated by the quadrupolar mode f_2, whose frequency depends on the mass and EOS of remnant.

(c) The late post-merger phase, where the star remnant configuration becomes almost axisymmetric, but still differentially rotating, convective instabilities may appear and trigger inertial modes for systems whose remnant lives long enough (more than ~ 50 ms after the merger). In this phase the main f_2 mode gets suppressed and the inertial modes are the only present [36, 38]. All the models that will be considered in 4.2 form a hyper massive neutron star after the merger that lives for some tens of milliseconds before eventually collapses into BH (see SLy, H4 and SFHo).

Figure 4.1 shows the plus polarization of the dominant mode (2,2) of the gravitational wave strain extracted from the numerical simulations performed in [37, 38] that have developed a long-living remnant after the merger. The method that have been used to obtain is the same reported in 3.4. The initial distance set for all the models considered in this work is 44.3 km and all the initial parameters have been summed up in 4.1. From that figure, one can clearly note that the gravitational wave signal is strongly related to the equation of state: the GW strain increases more quickly for the system with lower compactness (H4 and MS1) resulting in a shorter merger time, while the post-merger signal decreases depending on the remnant deformation and redistribution of the angular momentum. As the star approaches to a more axisymmetric state, some interesting features appear in the later stages of the post merger that will be discussed in 4.2.

Here we report the general settings used to run most of the numerical simulations that will be displayed in the following sections, which are an evolution of other previous works of the Parma group [64, 65, 66, 67, 36, 37, 38]. For standard resolution runs, the grid spacing that has been used for the simulations is $dx = 0.1875$ CU$=$ 277 m (see [64] for the discussion of the convergence properties of the code), otherwise the resolution is reported explicitly. As mentioned in the previous chapters, the simulations were performed using the

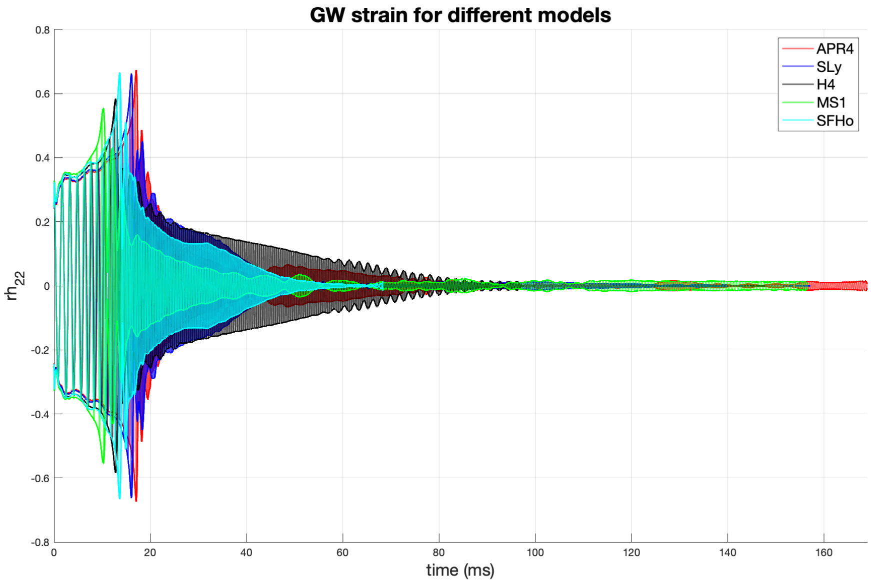

Figure 4.1: Plus polarization of the GW signal extracted from all the long-time simulations performed. The models refers to those reported in Table 4.1. Note that the signal is significantly different depending on the EOS considered.

`Einstein Toolkit` for the time evolution and the `LORENE` code for the initial data. In particular, the evolved variables were discretized on a Cartesian grid with 6 levels of fixed mesh refinement, each using twice the resolution of its parent level. The outermost face of the grid was set at $720 M_{\odot} \sim 1063$ km from the center. The choice for the numerical scheme of the metric is BSSN-OK 3.1.1 and the general relativistic hydrodynamics equations have been solved using the HRSC methods implemented by the thorn `GRHydro`. In particular, the HLLE Riemann solver(see section 3.2.2) and the fifth order reconstruction method WENO(see section 3.2.1) have been used. For the time evolution we used a fourth-order Runge-Kutta method. Moreover, for numerical reasons, the system is evolved on an external atmosphere set to $\rho = 6.1 \times 10^5$ g/cm^3 for the results presented in section 4.1, while an external atmosphere of one order of magnitude larger is employed in section 4.2.

4.1 The early post-merger phase: mass ejection and oscillational modes

Coalescing neutron stars that end up merging, generate an extremely violent phenomenon that does not only causes the emission of strong gravitational radiation, but also matter can be ejected during this phase. In order to take a deeper look, we considered 20 different models with equal mass (from 1.18

EOS	M	M_0	C	M_{ADM}	J_{ADM}	Ω_0 (krad/s)
APR4	1.276	1.400	0.166	2.528	6.577	1.767
SLy	1.281	1.400	0.161	2.538	6.623	1.770
H4	1.300	1.400	0.137	2.576	6.802	1.783
MS1	1.305	1.400	0.129	2.585	6.850	1.787
SFHo	1.300	1.418	0.161	2.569	6.700	1.781

Table 4.1: List of parameters for the initial models of the long-living simulations that have been performed. M is the gravitational mass, M_0 the baryon mass, and C the compactness of the individual stars. $M_{\rm ADM}$ is the ADM mass of the binary system and $J_{\rm ADM}$ its angular momentum, while Ω_0 is the angular velocity at the beginning of the simulations. All the quantities are expressed in terms of $M_\odot$, unless it is explicitly reported.

$M_\odot$, up to 1.42 $M_\odot$, for the heaviest SFHo model) and two (slightly) different version of the SFHo (see 2.2 for further details) equation of state, namely the SFHo and SFHo-HD EOS. The SFHo-HD one is based on the standard SFHo of [63] with the addition of Delta and Hyperons as in [134, 135]. All the parameters used for the initial data are reported in Table 4.2 and the piecewise approximation that have been done in this case is also reported in section 2.2.1. In particular, the thermal component of these models is parametrized using $\Gamma_{\rm th} = 1.8$.

4.1.1 Estimate of the ejected mass $M_{\rm ej}$ and the disk mass $M_{\rm disk}$

The estimate of the ejected mass was performed using the condition on the time component of the fluid four-velocity u_t to be $u_t < -1$ locally in order to determine if the matter is gravitationally unbounded or not, although it is not a sufficient condition [136]. The total unbounded mass on the grid was indeed computed using the previous condition (and not considering the part of the computational grid that correspond to the atmosphere) at each simulation time, and assuming the maximum of these values as the total ejected mass, denoted as $M_{\rm ej}$. Moreover, we estimated the disk mass $M_{\rm disk}$ as the total mass present in the computational grid having a density $\rho \leq 3.3\times10^{11}$ g/cm^3 and is bound (i.e. $u_t > -1$) 20 ms after merger. With this method, it is possible to make an estimate of the disk mass that is not yet unbound due to dynamical ejection. In table 4.3 we reported the values of both the dynamical ejected ($M_{\rm ej}$) and disk mass ($M_{\rm disk}$).

All the simulated models show a very similar behaviour. The main properties of the evolution are shown in figures 4.2 and 4.3. In particular, in figure 4.2 are shown the density of the expelled matter and its temperature at different times of the evolution just after merger. In figure 4.3 instead, we show the velocities and localization of the unbounded matter at the same

model	M	R	C	M_{ADM}	J_{ADM}	Ω_0 (krad/s)
SFHo-HD	1.18	11.166	0.156	2.340	5.783	1.713
SFHo-HD	1.20	11.133	0.159	2.379	5.945	1.725
SFHo-HD	1.22	11.100	0.162	2.419	6.092	1.736
SFHo-HD	1.24	11.067	0.165	2.451	6.257	1.747
SFHo-HD	1.26	11.034	0.169	2.490	6.427	1.759
SFHo-HD	1.28	11.002	0.171	2.530	6.597	1.770
SFHo-HD	1.30	10.970	0.175	2.570	6.771	1.781
SFHo	1.18	11.942	0.145	2.332	5.765	1.714
SFHo	1.20	11.939	0.148	2.372	5.926	1.725
SFHo	1.22	11.934	0.151	2.431	6.174	1.742
SFHo	1.24	11.929	0.153	2.450	6.258	1.748
SFHo	1.26	11.925	0.156	2.490	6.426	1.759
SFHo	1.28	11.919	0.159	2.529	6.597	1.770
SFHo	1.30	11.913	0.161	2.569	6.770	1.781
SFHo	1.32	11.907	0.164	2.608	6.945	1.791
SFHo	1.34	11.900	0.166	2.647	7.121	1.801
SFHo	1.36	11.893	0.169	2.687	7.299	1.812
SFHo	1.38	11.885	0.171	2.726	7.480	1.822
SFHo	1.40	11.877	0.174	2.776	7.663	1.832
SFHo	1.42	11.868	0.177	2.805	7.847	1.843

Table 4.2: List of the parameters of the initial data configurations for the models considered in the work presented in section 4.1. M is the gravitational mass, R the radius in km, and C the compactness of the individual stars. M_{ADM} and J_{ADM} are the ADM mass and angular momentum, Ω_0 is the initial angular velocity of the binary system at the beginning of the simulation. All the quantities are expressed in terms of $M_\odot$, unless it is explicitly reported.

model	M_{ej}(m$M_\odot$)	M_{disk}(m$M_\odot$)	E_{GW}(m$M_\odot$)	f_2(kHz)	t_{BH}(ms)
HD 118	12.99	12.92	25.42	3.71	3.82
HD 120	9.44	13.81	22.42	4.00	3.16
HD 122	4.29	8.34	6.06	-	1.91
HD 124	3.01	2.89	0.66	-	1.00
HD 126	0.74	2.45	0.20	-	0.79
HD 128	0.06	0.74	0.04	-	0.70
HD 130	0.04	0.71	0.01	-	0.59
SFHo 118	1.97	76.66	42.16	2.88	-
SFHo 120	2.09	71.72	43.87	2.90	-
SFHo 122	1.73	91.81	42.00	2.90	-
SFHo 124	1.82	65.58	52.98	2.96	-
SFHo 126	2.38	60.86	58.33	2.98	-
SFHo 128	3.15	112.24	50.33	3.05	-
SFHo 130	4.52	73.82	59.33	3.06	-
SFHo 132	6.01	88.87	67.29	3.18	25.75
SFHo 134	9.51	49.27	65.09	3.25	13.55
SFHo 136	16.24	30.71	58.76	3.40	9.42
SFHo 138	10.37	16.09	46.06	3.55	5.06
SFHo 140	4.17	6.45	22.39	-	2.13
SFHo 142	2.25	2.01	2.02	-	0.98

Table 4.3: Values of the ejected mass ($M_{\rm ej}$) and disk mass ($M_{\rm disk}$), energy emitted in GW in the post-merger phase ($E_{\rm GW}$), frequency of the main peak of the GW f_2 and the time to collapse to BH ($t_{\rm BH}$) for the models considered in this section. Here "HD" stands for "SFHo-HD" to avoid redundancy and the number after the EOS name represents the single star mass related to the model.

times considered in the previous figure. From these figures, we note that the dynamical ejection of matter occurs in three separated moments, which correspond to maximum density oscillations, becoming hotter ($T \sim 30$ MeV) and with outgoing velocities around $0.3c$.

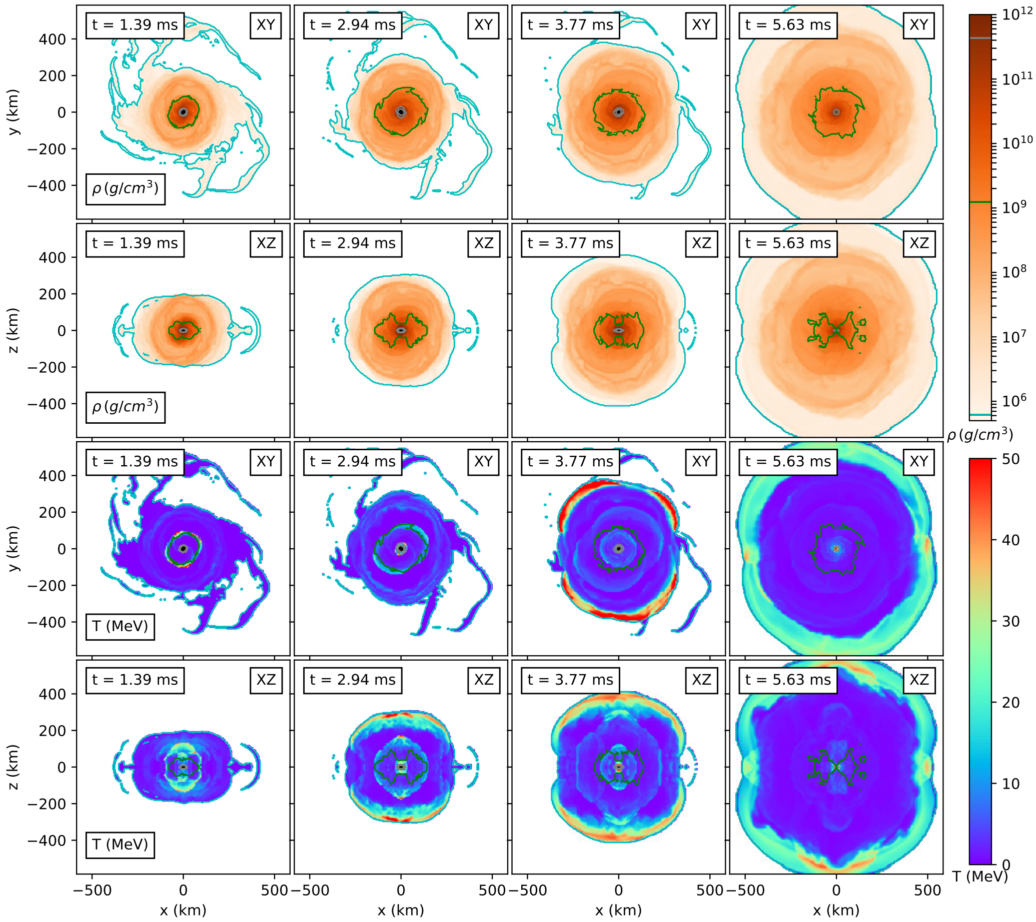

Figure 4.2: Snapshots of the density (ρ) and the temperature (T) profile in the XY and XZ plane at different times The profiles refers to the model described by the SFHo-HD EOS for model 118vs118. The colored lines refer to the density contour corresponding to the densities used for the polytropic approximation while the white region outside the solid cyan line are the region in which the density correspond to "atmosphere" and are not included in the computation.

In order to get a more precise estimate of the ejected mass, we used another technique based on the calculation of the flow of the material leaving a coordinate sphere surface with a given radius using the $u_t < -1$ condition. This is implemented by the `Outflow` thorn of the `Einstein Toolkit`, and we set different radii (from 65 CU≃96 km up to 700 CU≃1034 km) where the outflows are computed. In figure 4.4 the outflows of the SFHo-HD 118vs118

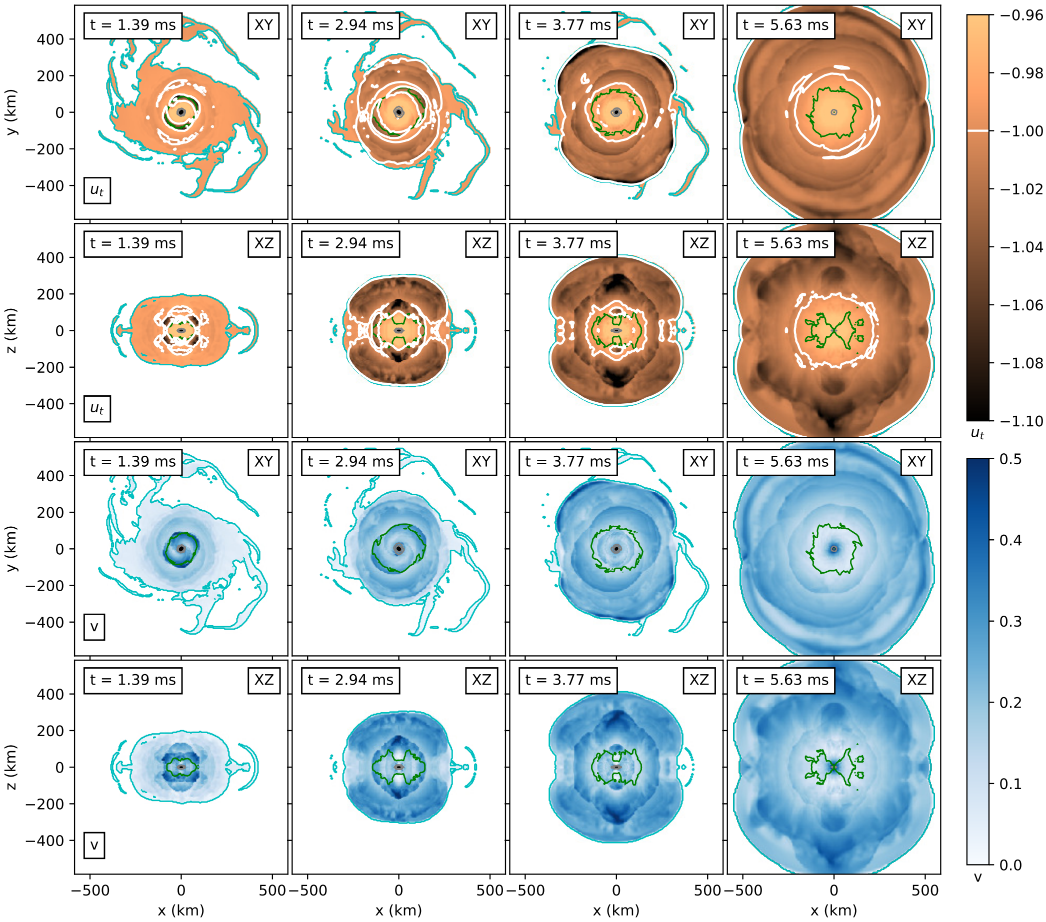

Figure 4.3: Snapshots of the XY and XZ projections of the time component of the fluid velocity (u_t) and the matter velocity (v) for the SFHo-HD 118vs118 model. The solid white line in the first two rows refers to the $u_t = -1$ condition, which defines the difference from bound and unbound matter. The times reported are relative to the merger time.

(left) and SFHo 136vs136 (right) models are displayed. Following the flow of the unbound matter during the evolution, we can make an estimate of the ejected mass by integrating on time, at each radius, the unbound matter flow. The total flows of unbound matter have been measured at coordinate radius 96, 220, 443, and 590 km and are (5.0, 10.7, 11.24, 11.45)m$M_{\odot}$respectively. It is evident that this procedure for computing the total ejected mass is very sensitive to the coordinate radius of the spherical surface used to compute the flow and this is a common property of all the simulated models. In particular, comparing the results obtained using this method with those obtained by considering the maximum of total unbound mass (see table 4.3 for the details) on the whole computational grid at a given time (black line of the lower panels in figure 4.4). We note that the difference between the estimates of

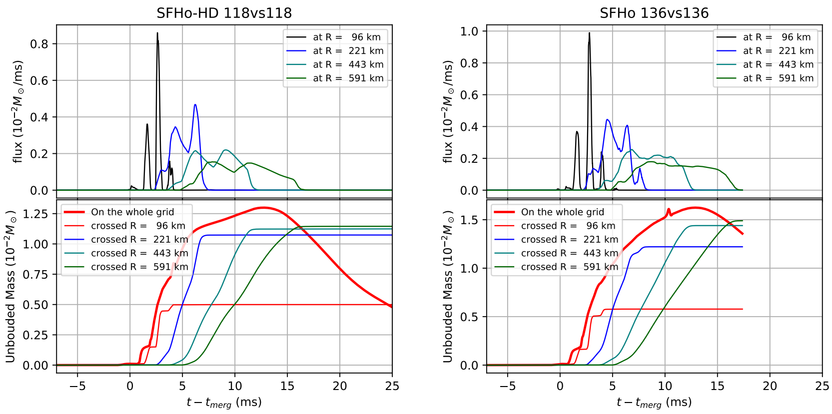

Figure 4.4: Plots of the material unbound, using the $u_t < -1$ condition, crossing coordinate spherical surfaces with different radii. In this figure, the outcome of four of them for the SFHo-HD model with mass of $1.18M_\odot$and for the SFHo model with mass of $1.36M_\odot$, in particular the ones corresponding to a radius of 65 CU$\simeq$96 km,150 CU$\simeq$221 km, 300 CU$\simeq$443 km and 400 CU$\simeq$591 km are reported. We observe that three peaks at the closest surface, corresponding to the "rebounds" of the hypermassive neutron star formed after the merger, are present. Those peaks become larger when crossing the farther surfaces due to the different velocities of the ejected material. Showing that these feature are common to the case of both the two EoSs considered here.

$M_{\rm ej}$ made with the two methods, is always less than about 20% and the two results get closer by increasing the extraction radius. From the lower panels of figure 4.4 we observe that most of the dynamically unbound mass is generated between 100 km and 200 km from the center of the remnant, and it is related to the three outbursts linked to the "bouncing" of the maximum density profile. This is more clear if we look at the upper panels of this figure, where the three outburst are highlighted by the red line of the closest extraction radius flux.

The same dynamics is associated to the mass ejection for all the considered models (except for those that directly collapse to BH and for which the mass ejection is suppressed). An interesting feature concerning the mass ejected is the maximum which is located at a value of $M_{\rm tot}$ (the sum of the single masses of the two stars of the system) slightly smaller than the value of $M_{\rm threshold}$, which is the first combination of masses that end up in a direct collapse to BH. In particular, the maximum is located at $2.72M_\odot$for the SFHo EOS, corresponding to an ejected mass of $\simeq 16 \times 10^{-3}\ M_\odot$, while for the SFHo-HD case, it is not possible to determine the maximum of the ejected mass, which anyway should be located below or close to $\sim 2.36M_\odot$. For this value, we have found an ejected mass of $\simeq 13 \times 10^{-3}\ M_\odot$, very close to the maximum of the SFHo EOS. From the values in table 4.3 it is clear that there is a very steep decay in the ejected mass as the total mass increases and the ejection is almost completely suppressed in the case of direct collapse to BH.

The values of the disk mass $M_{\rm disk}$ highlights another clear difference between the two EOS: in the case of SFHo-HD it is always $\leq 0.01M_{\odot}$, whereas for SFHo it can be an order of magnitude larger.

4.1.2 GW spectrum in the early post-merger

In figure 4.5 we note a striking feature in the GW spectrum for those models where $M_{\rm tot} \geq M_{\rm threshold}$: they do not display any post merger f_2 peak. This is related to the fact that, for these models, a direct (in less than 1 ms after the merger) collapse to BH occurs. The times of the collapse to black hole are reported in the last column of table 4.3. In the cases where a black hole forms in a delayed time after the merger, the spectrum is the same as the one discussed in [117, 32, 67] and references therein. Importantly, the frequency of the f_2 mode increases with the mass of the star, while its tidal parameters decreases. We also observe that secondary peaks are present in some cases, but their importance decreases as the total mass of the system is reduced.

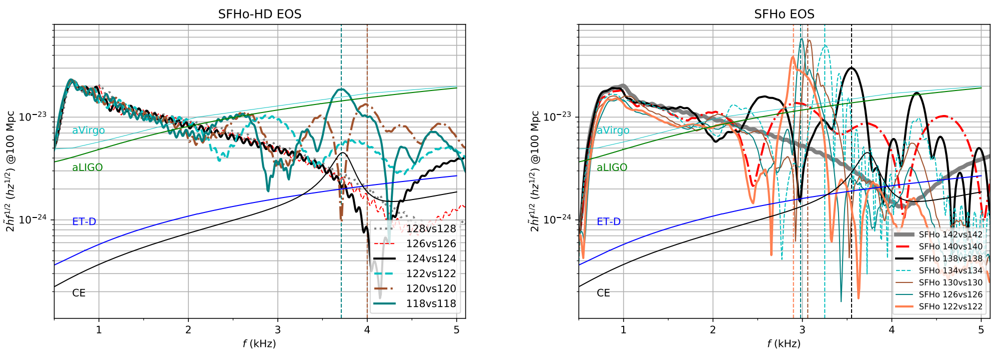

Figure 4.5: Spectrum of the GW signal for all the models considered. No post-merger peak is visible for the models with SFHo-HD EOS with total mass larger than $2.48M_{\odot}$and SFHo EOS with total mass larger than $2.84M_{\odot}$. In the case of models with SFHo EOS, when the total mass is $2.80M_{\odot}$just a marginal main f_2 peak is visible while all the less massive model show a distinct main f_2 post merger peak and two (of lower amplitudes) side peaks (forming a three peaks structure) that become less important as the total mass decrease.

The presence of a well defined f_2 peak in the spectrum could lead to a clear determination of some properties of the merger as well as of the EOS. In fact, this would be a precise signature of the fact that the system did not directly collapse to BH, encoding information on the properties of dense matter in the spectrum. For instance, the f_2 peak of a system of equal mass stars at total mass $M_{\rm tot} = 2.36M_{\odot}$is at frequency $f_2 = 3.71$ kHz or $f_2 = 2.88$ kHz if the

EOS is SFHo-HD or SFHo, respectively. Unfortunately, the amount of energy radiated by GW (see table 4.3) that would be available for mode detection is going to be at best of the order of $0.1 M_{\odot}$, so not enough for current generation detectors. However, this is going to be a distinct feature to be observed in the third generation detectors.

Secondary peaks in the post-merger phase

In the last paragraph, we were pointing out that in some case, additional peaks were visible in the GW spectrum for those models that did not directly collapse to BH. In this section we consider the same SFHo 130vs130 model at standard resolution ($dx \simeq 277$ m) and also the SLy 14vs14 and APR4 14vs14 (whose parameters are summed up in table 4.1) that will be an argument of the discussion in section 4.2.In table 4.4 we report the frequencies of such modes that have been labeled as f_1 and f_3, following the notation of [34], and in figure 4.6 we show a "zoomed" picture of the moment where the three modes (f_1, f_2,f_3) are all visible. These plots show a portion of the time-frequency analysis that has been performed on these models using the continuous wavelet transform (CWT) method, that will be discussed in section 4.2.3.

The nature of these secondary peaks that appear just after the merger have been discussed in [34, 32]. The hypothesis that was brought up in [32] was that the modes f_1 and f_3 are a nonlinear combination of the main f_2 mode and the quasi-radial oscillation of the remnant, as described in [29], which is the reason why the labels $2-0$ and $2+0$ are used for these modes.

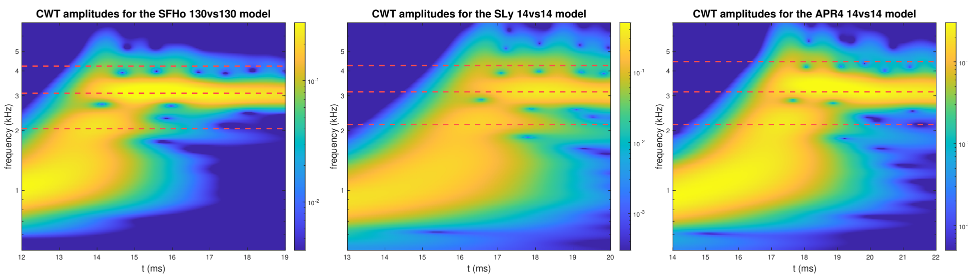

Figure 4.6: Continuous wavelet transform (CWT) scalogram (discussion in section 4.2.3 details around the merger for the SFHo, APR4 and SLy models. The red dashed lines refers to the f_1 (lower), f_2 (middle), and f_3 (upper) modes. The yellow colored regions of the figures represent the areas where the module of the coefficients of the CWT are larger.

As one can note from the data in table 4.4, the frequencies of these two modes can be obtained by subtracting (or adding) the value of the frequency of the quasi-radial oscillation f_0 to the main f_2 mode. The frequencies of the f_{2-0} (or f_1) and f_{2+0} (or f_3) can be extracted both from the GW spectrum or from the module of the coefficients of the CWT, as in figure 4.6, where the post-merger modes are highlighted with the dashed red lines. On the other

model	f_0(kHz)	τ_0(ms)	f_1(kHz)	τ_1(ms)	f_3(kHz)	τ_3(ms)	f_2(kHz)
SFHo	1.07	1.93	2.05	1.23	4.23	2.40	3.09
APR4	1.11	1.15	2.15	1.02	4.46	1.35	3.14
SLy	1.02	1.93	2.15	1.33	4.26	1.87	3.14

Table 4.4: Damping time of the secondary peaks (f_1 and f_3) visible in the GW spectrum for the SFHo 130vs130 model, the SLy 14vs14 and APR4 14vs14, compared to the quasi-oscillational mode (f_0) one. The damping times τ have been labeled in the same way as the modes.

hand, the value of the f_0 frequency has been obtained fitting the oscillating part of the minimum of the lapse function with a quadratic trial function with a superimposed damped oscillation, as in [64]:

$$\alpha_{\min} = a_2 t^2 + a_1 t + a_0 + A_0 e^{-\frac{t}{\tau}} \sin\left(2\pi f_0 t + \phi_0\right). \tag{4.1}$$

That method allows us to obtain the damping time of the quasi-radial mode τ, which now can be compared to the one of the f_{2-0} and f_{2+0} modes. In order to make this comparison, we computed also the damping times of f_{2-0} and f_{2+0} by fitting the descending part of the CWT amplitude at the mode frequency using a decaying exponential of the type $A = A_0 e^{-t/\tau}$. At this point, we noticed that for both the quasi-radial mode and the secondary peaks of the post-merger GW spectrum, the damping times are comparable.

4.2 The late post-merger phase: convective instabilities and inertial modes

To obtain reliable theoretical models of postmerger GW emission can only nonlinear, general relativistic numerical simulations represent the way to do it. As we mentioned a the beginning of the chapter, such numerical simulations of BNS mergers show that the outcome depends on the component masses and EOS (see [15, 16, 17, 18] for reviews). If the initial masses of the stars are large enough, prompt collapse to BH is the likely outcome, whereas the system may show a delayed collapse (or even no collapse) otherwise. In these cases, the resulting object may be either a hypermassive neutron star (HMNS), where differential rotation and thermal gradients temporarily supports the remnant, or even a supramassive neutron star, when the mass is small enough to be supported by uniform rotation. In both cases, the result is a sufficiently long-living remnant, which can produce a large amount of high-frequency (∼kHz) gravitational radiation. While HMNS may avoid collapse for tens up to hundreds of milliseconds, supramassive neutron stars can avoid collapse on much longer timescales, which are set by magnetic dipole radiation. Additional mechanism of GW emission may become relevant at such long timescales, such as the Chandrasekhar-Friedman-Schutz (CFS) instability [137, 138], shear instabilities [139, 140, 141], or convective instabilities in rotating stars with non-barotropic EOS [81].

The simulations that are considered in this section follow the same prescriptions that have been used in the previous section, with the exception of the thorns for the mass ejection estimate, and in [64, 65, 66, 67]. The only difference in this case is the use of the $\pi-$symmetry to reduce the computational cost of a factor 2. This allows to push the limit of the simulated time to > 100 ms, where the last 100 ms corresponds to the post-merger phase. We considered here four different EOS, namely APR4, SLy, H4 and MS1, using a spatial resolution of $dx = 277$m as the standard resolution, while for the SLy EOS we also performed a high-resolution run using a grid spacing of $dx = 185$m (denoted as SLy HR). For these models, also a low-resolution (LR) run was performed at $dx = 368$m that will be discussed in appendix A.

4.2.1 GW spectrum evolution

From figure 4.1 we note that the overall behaviour for the first phase (inspiral and merger) of the binary system is similar for each model, including the SFHo one which is not discussed in this section, except for the time of the merger, until the two stars form a bar-deformed remnant, as in [64]. We also observe that a delayed collapse to black hole occurs in the case of SLy at ~ 124 ms and H4 at ~ 84 ms, whereas for the APR4 and MS1 EOS the remnant do not collapse to BH in the entire simulation time ~ 150 ms.

The evolution of the GW amplitude for the SLy EOS (blue line) shows a relatively slow decay up to 20 ms after merger, which is due to both nonlinear hydrodynamics and GW emission. This is followed by a second phase of a faster decay, which lasts up to 65 ms after the merger, where the emission of gravitational radiation is almost ceased and the remnant has become nearly axisymmetric. After that phase, at around 65 ms after merger, a small revival of the GW emission is visible (see [36] and the following section for further details).

For the MS1 EOS, the initial decay of GW emission lasts for about 40 ms after merger and it is followed by several episodes of revival of GW emission until 100 ms after merger. At later times of the evolution, the remnant radiates GW almost at a single frequency and at constant amplitude. This behaviour would be expected in the case of a specific unstable mode saturation at maximum amplitude, due to the balance between the energy gained by the instability and the energy radiated.

For the GW strain of the H4 EOS showed in 4.1, the decay of the GW amplitude is almost linear for the most part of the time period up to 80 ms, when the remnant ends up collapsing to BH. However, at around 45 ms after merger, a modulation appears in the amplitude evolution, indicating the presence of a secondary frequency (we will discuss its interpretation in the following section).In the case of the APR4, we also note a similar late-time revival of GW emission (more than 60 ms after the merger).In addition, we noticed a strong revival at around 25 ms after merger.

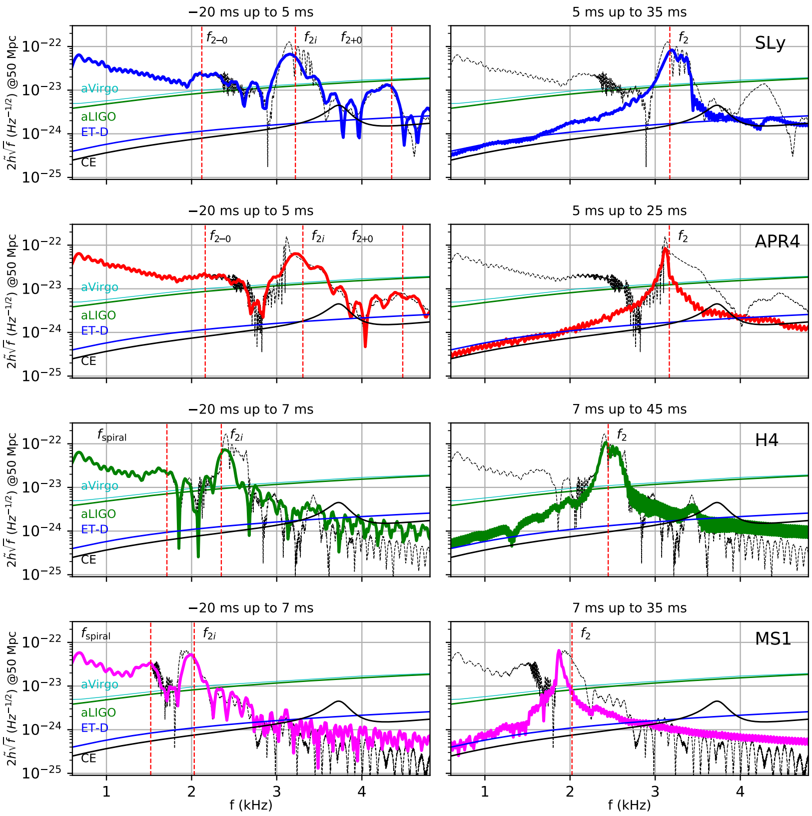

Figure 4.7: GW spectra of the four models (each row refers to a specific EOS) considered at 50 Mpc with optimal orientation. First row is the SLy model, second row APR4, third row H4 and MS1 at the bottom. The thin-dashed black lines represent the full spectra, whereas the colored lines refers to the time window specified at the top of each frame, in order to emphasize the contribution of the dominant spectral components at different times. The solid lines in the background represent the design sensitivities of Advanced Virgo [25], Advanced LIGO [24], Einstein Telescope[142], and Cosmic Explorer [143].

In order to understand the nature of this phenomena we look at figure 4.9, where we show the rotational profile $\Omega/2\pi$ versus the coordinate radius r for all four models at 40 ms (left panel) and the specific case of the APR4 at different times (right panel). In particular, we note that the differentially rotating remnant has a non trivial rotational profile and also the temperature profile (which is shown for the case of the SLy model in figure 4.11), in which the temperature has an off-center maximum, presenting a cold core and an outer hot ring inside the 10 km radius. This kind of thermal profile is in agreement

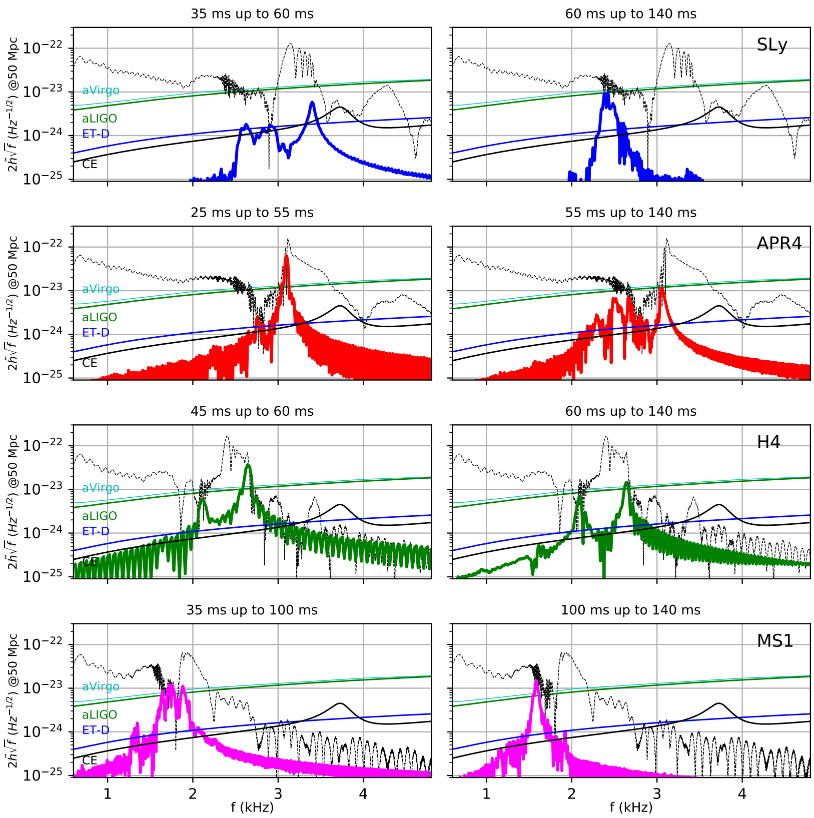

Figure 4.8: Same plots of figure 4.7 but for the following time intervals referring to the latest phase of the post-merger.

with the literature when similar assumptions are made [144, 145, 146], and only in the case of strong viscosity different thermal profile are observed [147]. The remnant may be subject to a variety of instabilities, such as the dynamical bar-mode instability (see [148, 149, 23] and references therein), and the aforementioned CFS and shear instabilities that can develop in the case of differentially rotating stars. In addition to this list, in section 4.2.2 we discuss the possibility of the excitation of additional modes in the post-merger phase for a sufficiently long-living remnant. In figure 4.9 we mark the pattern speed frequency of the $m = 2$ modes, which is calculated as half the GW frequency, with the horizontal dashed lines. In left panel of this figure we note that at 40 ms, only the APR4 and MS1 models are in corotation with the mode pattern speed. Right panel of figure 4.9 focuses on the APR4 case at different time showing the pattern speed of the main $m = 2$ $f-$mode at 1.55 kHz, and the excited mode at the start of its excitation at 1.35 kHz and at the end at 1.26 kHz. It is interesting to observe that the revival amplitude of the $m = 2$ $f-$mode at 25 ms after merger coincides with the corotation between the mode and the HMNS in a small region. This phenomenon is possible only when the convective instability of a small region of the star and the corotation occur at the same time. In figure 4.15, in effect, a very small region of the remnant presents $A_r > 0$ at 25 ms, and angular momentum from the rotation of the star is injected into the main $f-$mode.

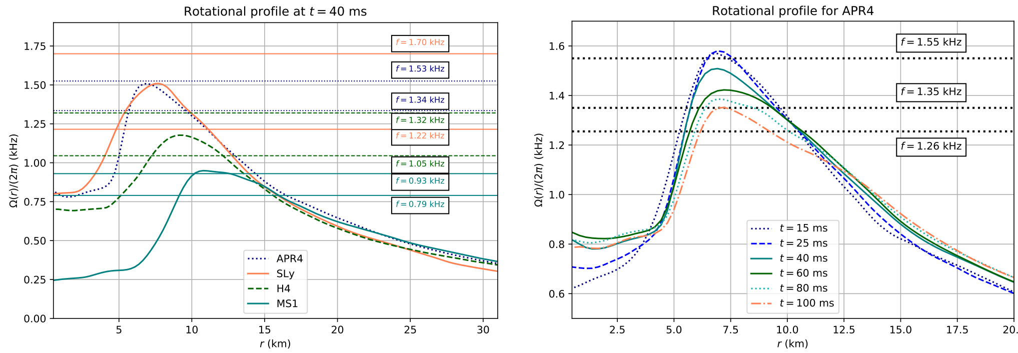

Figure 4.9: Left panel: Rotational profile $\Omega/2\pi$ vs. coordinate radius r for all the models at $t = 40$ ms. The pattern speed frequencies of the two main $m = 2$ modes for each model are marked by the horizontal lines. Right panel: Rotational profiles $\Omega/2\pi$ vs. coordinate radius r for the APR4 EOS at different times after merger. The pattern speed of the main $f-$mode (1.55 kHz) and the main excited mode at the start (1.35 kHz) and at the end of the evolution (1.26 kHz) are marked by the horizontal lines.

In order to take a more in-depth look at the GW features of these four models, we present in figure 4.7 and 4.8 the GW spectra at different time-windows (the discussion on this choice will be in section 4.2.2) of the APR4, SLy, H4, and MS1 EOS. These figures, show the scaled PSD $2\tilde{h}\sqrt{f}$ (where $\tilde{h}$ is the Fourier transform of h) of the GW signal for an optimally aligned source at 50 Mpc. Each row refers to a different model and, for every frame, the thin-dashed black lines correspond to the full spectrum computed on the entire simulation time (i.e. $t - t_{\mathrm{merger}} \in [-20, 140]$ ms), while the colored line to the one computed in the chosen time window. We did not apply any windowing function to the Fourier transform in order to achieve a clearer separation of the contribution to the spectra. This led to the appearance of some artifacts in the FFT due to the finite size of the time intervals. In the first column, which roughly corresponds to the early post-merger phase, of figure 4.7, the vertical red lines mark the initial position of the frequency f_{2i} of the dominant $m = 2$ f-mode and for the subdominant peaks f_{2-0} and f_{2+0} (for the APR4 and SLy), that have already been discussed in section 4.1.2, and also f_{spiral} for the the H4 and MS1 EOS. These peaks can be obtained from the GW spectrum, but also the ESPRIT Prony algorithm [67, 35].

The second column of figure 4.7 correspond to the intermediate phase of the post-merger, where the dominant f_2 mode is the only mode present. The red dashed lines here mark the frequency of the $m = 2$ f-mode and we noticed that the position can remain very close to its initial one f_{2i} or it can display a secular time variation.

A common feature of all models is the fact that the $m = 2$ f-mode (f_2) dominates the full spectra in the EOS-dependent frequency range $\sim 2 - 3.5$ kHz. On the other hand, when moving to later time intervals, the dominant peaks in the spectra begin to change. In effect, in the time interval $t - t_{\text{merger}} \in [60, 140]$ ms, the spectrum is dominated by a peak of frequency ~ 2.38 kHz in the case of the SLy EOS and below 2 kHz for the MS1 EOS. For the APR4 model several nearby lower-frequency peaks contributing to the GW spectrum are present instead.

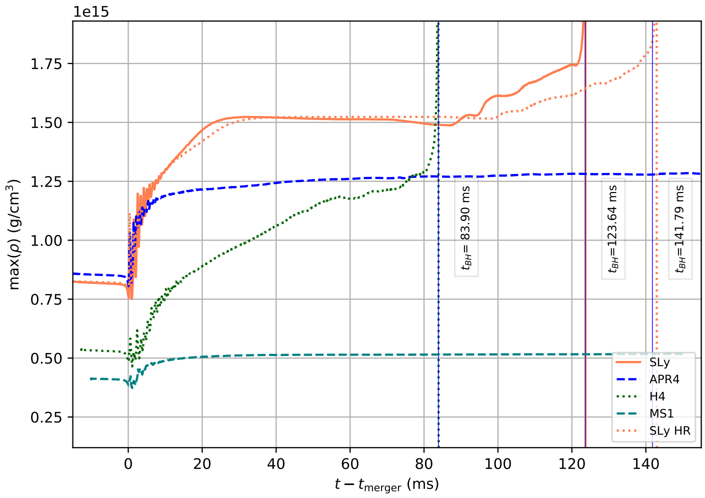

Figure 4.10: Maximum density as a function of time for all the four models simulated, including the high-resolution variant of the SLy EOS.

The spectra of the intermediate post-merger phase for the SLy EOS (5 ms to 35 ms) and the H4 EOS (7 ms to 45 ms) are consistent with the Prony's method results that will be discussed in section 4.2.2, where for these models the dominant f_2 frequency is subject to a slow drift in higher frequencies. In fact, the remnant experiences an almost steady drift to higher maximum densities (see figure 4.10) in this time period. It is known from [150] that the frequency of the fundamental fluid modes of a star scale as the square root of the average density. It is important to note that the remnant for these two models have a mass relatively close to the threshold mass for collapse to BH, which is the case of the SLy EOS and H4 EOS. In figure 4.7 and 4.8 it is shown also the design sensitivity of Advanced Virgo [25], Advanced LIGO [24], and the next generation of detectors Einstein Telescope [142], Cosmic Explorer [143]. We found that in all cases there is sufficient power in the lower-frequency modes to render them potentially observable by third-generation detectors as ET-D and CE. In particular, the signal to noise ratios for optimal use of matched filtering techniques for the signals displayed in figure 4.8 are ~ 1.3 and ~ 3.5 for SLy, ~ 9.1 and ~ 3.7 for APR4, ~ 11.6 and ~ 5.1 for H4, ~ 9.7 and

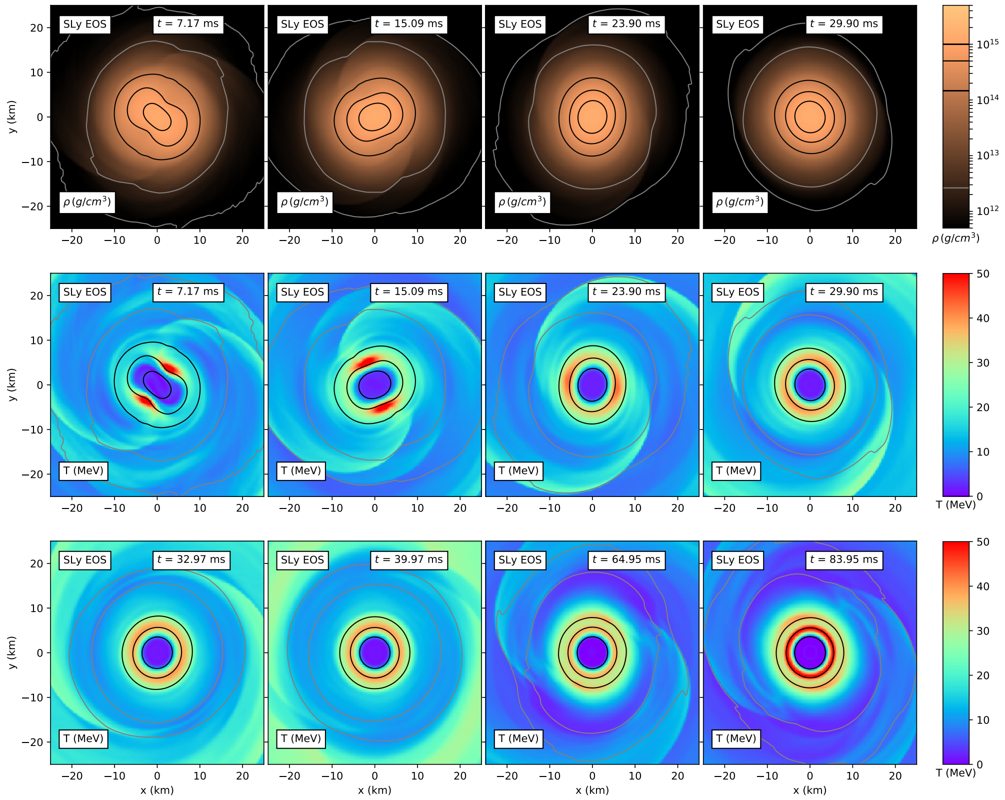

Figure 4.11: Snapshots of the density and temperature on the equatorial plane (XY) for the SLy EOS at different times relative to the merger.

$\sim$ 8.3 for MS1 EOS, respectively for the case of the Cosmic Explorer. The S/N ratios for the Einstein Telescope-D then are $\sim$ 1.2 and $\sim$ 2.5 for SLy, $\sim$ 8.0 and $\sim$ 2.9 for APR4, $\sim$ 8.7 and $\sim$ 3.7 for H4, $\sim$ 6.4 and $\sim$ 5.5 for MS1 EOS. We observe that the S/N ratio is significantly higher in the first $\sim$ 40 ms after merger in any case, while it becomes almost two orders of magnitude smaller when the lower-frequency modes appear.

4.2.2 Mode analysis using Prony's method and convective instability

The dynamics of BNS systems can be neatly captured with time-frequency techniques that can display the evolution of the GW emission also in its frequency, as in figure 4.12, where the h_{22} component of the spherical harmonic decomposition is shown. On top of each spectrogram (computed using FFT, we will discuss in section 4.2.3 its CWT alternative) we also superimpose with thick grey lines the time evolution of the frequency of the main active modes of the remnant. This procedure is done using the ESPRIT Prony's method, which is discussed in detail in [67, 35]. In the lower half of each panel, we report the amplitudes of the main active mode found with Prony's method.

We already observed that the H4 and SLy models collapse to BH after 84 ms and 124 ms, respectively, whereas APR4 and MS1 models do not show a collapse to BH in the entire time simulated. As expected, the dominant mode in the early-to-intermediate post-merger phase is the $m = 2$ $f-$mode, with a frequency above 3 kHz for SLy and APR4, about 2.5 kHz for H4, and below 2 kHz for MS1. In all four cases, this mode is characterized by a decaying amplitude over this time interval. In particular, distinct lower-frequency modes appear in the evolution, at $t - t_{\rm merger} \sim 35$ ms for the SLy and MS1, ~ 45 ms for the H4, and ~ 55 ms for APR4. At late times, this type of GW emission becomes dominant over the initial $m = 2$ $f-$mode.

Looking closer at the result of Prony's analysis of the behaviour of the post-merger signal for each EOS we observe:

- For the SLy EOS the early post-merger phase lasts up to 5 ms after merger (we also see oscillations in the maximum density, as in figure 4.10, and transient GW emission due to secondary peaks as discussed in section 4.1.2). After this time, the main $m = 2$ $f-$mode is the only significant oscillation mode, which also presents frequency changes at a constant rate of $\sim 1.6 \times 10^{-2}$ kHz/ms until ~ 20 ms, when the frequency becomes almost constant. The amplitude decay of the $m = 2$ $f-$mode is slower in the first 20 ms than in the $20 - 60$ ms time interval, and after this time, the mode has practically faded away. An additional mode appears at ~ 37 ms with a frequency of ~ 2.93 kHz alongside the main $f-$mode. In the first 8 ms from its appearance, this new mode's amplitude has grown almost an order of magnitude, and then rapidly collapses. Following this phase, between 45 ms and 60 ms a new phase of excitation, saturation and destruction of a lower-frequency mode at ~ 2.7 kHz occurs. The last phase of the evolution (from 60 ms to 110 ms) consists in the presence of a single dominant mode at ~ 2.5 kHz at nearly constant amplitude. We note that the saturation amplitude is comparable for all these modes, but in order to define whether it is the same mode or different modes that appear requires a more detailed mode analysis.

- For the APR4 EOS we note that the early post-merger phase ends at ~ 3.4 ms. At this point, only the main $m = 2$ $f-$mode at ~ 3.1 kHz is present, remaining constant up to ~ 25 ms, but constantly decaying in amplitude. At this time, we observe a small glitch in the frequency, which almost remains constant up to ~ 54 ms, but with a considerable growth in amplitude in a short time span that is due to the corotation phenomenon discussed in section 4.2.1. The main $f-$mode remains visible up to ~ 100 ms even if the damping rate becomes larger than in the previous phase. At ~ 54 ms an additional mode at a frequency of ~ 2.70 kHz appears. Despite its frequency remains practically constant during the 54-100 ms time window, its amplitude shows rapid variations which can be interpreted as episodes of excitation-saturation-destruction. In the following time interval (between $\sim$ 105 ms and $\sim$ 120 ms), another episode takes place a the same frequency, but with a higher saturation amplitude that remains constant for a longer time. After that time interval we observe a few more episodes at a smaller frequency. Between $\sim$ 98 ms and $\sim$ 105 ms we noticed that a mode with smaller frequency ($\sim$ 2 kHz) appears, but we cannot exclude that this could be an artifact of Prony's method.

- The early post-merger phase of the H4 model end at $\sim$ 6.7 ms, when only one mode is present. The initial frequency of this mode is $\sim$ 2.37 kHz and changes constantly with a rate of $\sim 7.1 \times 10^{-3}$ kHz/ms up to $\sim 46ms$ after merger, when it becomes constant at a frequency of $\sim$ 2.64 kHz. During this time, the damping of the amplitude is constant. We observe the appearance of a second mode at $\sim$ 46 ms at a lower frequency of $\sim$ 2.11 kHz. This mode rises in amplitude on a dynamical timescale, saturates in a short time and remains nearly constant until the BH formation at $\sim$ 84 ms.

- For the MS1 model the early post merger phase ends at $\sim$ 6.7 ms, when only one mode is active at a frequency of $\sim$ 1.88 kHz. This mode remains practically constant up to $\sim$ 35 ms, with an amplitude that decay constantly. From $\sim$ 35 ms to $\sim$ 100 ms we observe several episodes of excitation-saturation-destruction of a lower-frequency mode. The final episode takes place at $\sim$ 100 ms, when the lower-frequency mode maintains a nearly constant (but slightly decreasing) frequency, $f \sim 1.55$ kHz, and a nearly constant saturation amplitude.

In order to better identify the difference of the various oscillation modes, we have also performed the FFT transform in time segments of 5 ms (we use the central time of the time window as the label) of the density distribution and extracted the Fourier amplitude at selected frequencies (in [151, 29] it is discussed its correlation with the mode eigenfunction). Figure 4.13 and 4.14 confirm that the modes that are clearly recognizable using Prony's method are actually excited modes, since the eigenfunction shape changes from the typical $m = l = 2$ one that is visible in the left column of each frame. In some case, as in the MS1 model for instance, a nodal line far from the center in the low-density envelope may be visible in the $m = 2$ $f-$mode. This is not a surprising feature for rapidly rotating differentially rotating stars, since the rotational forces can modify the structure of the eigenfunction in the low-density regions (see [151]).

The low-frequency modes that appear in the post-merger phase have the characteristics of inertial modes. They have the right frequency range, with the dominant mode having always a frequency smaller than the maximum

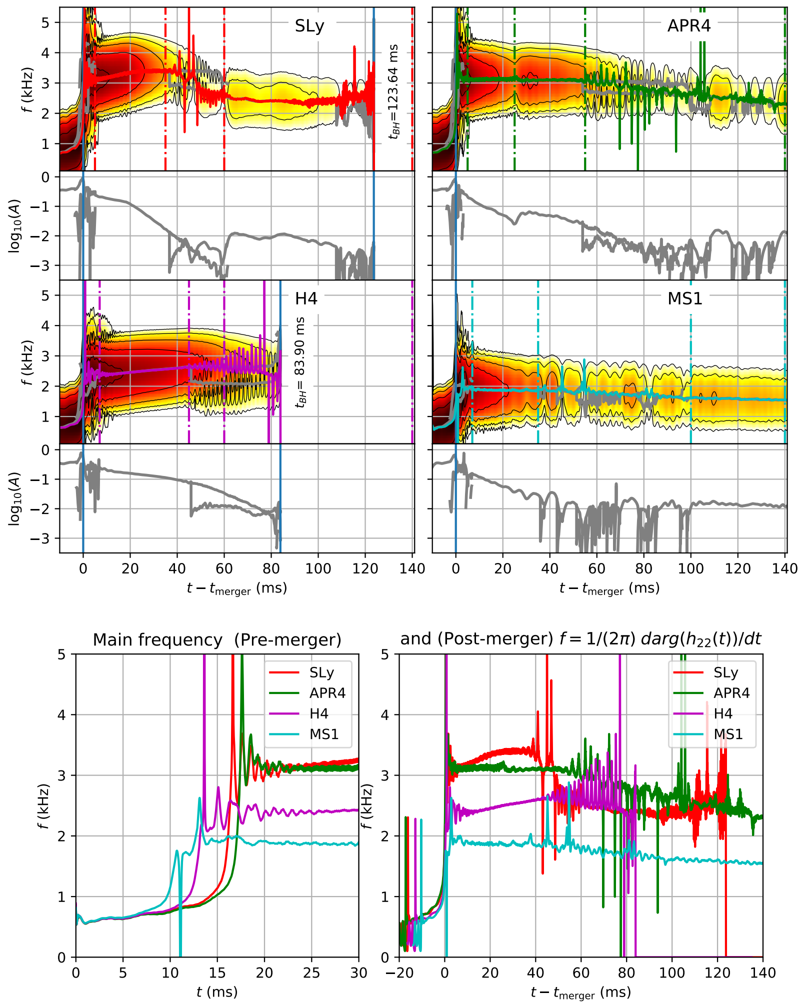

Figure 4.12: Picture of the time-frequency spectrograms of the $m = l = 2$ component of the GW strain for all four models. The top four panels show the superposition of the time-frequency spectrograms, represented by the colored region (darker is higher), and the main active modes recognized using ESPRIT Prony's method, represented by the thick gray lines. The bottom of these four panels show the amplitudes of the active modes in arbitrary units. The two bottom panels show the main frequency of the $f-$mode before (left) and during the entire evolution (right). The colored lines in these figures have also been superimposed on the upper 4 frames. The time of the collapse to BH for the SLy and H4 models is explicitly reported with the respect of the time of the merger.

rotational frequency of the star. The eigenfunction of excited modes shows a peak in the low-density outer regions of the remnant, presenting more nodal lines than the quadrupole mode. Moreover, in the case of rapidly rotating stars, inertial modes can be axial-led (reducing to axial $r-$modes in the limit of slow rotation) or polar-led (reducing to $g-$modes) [152, 153]. The latter are also called *gravito-inertial* modes. Since the nature of these modes comes from convective instability (see the next paragraph for the detailed discussion) in the outer layers of the remnant it is likely that at least some (or most) of the inertial modes observed are polar-led, i.e. gravito-inertial modes.

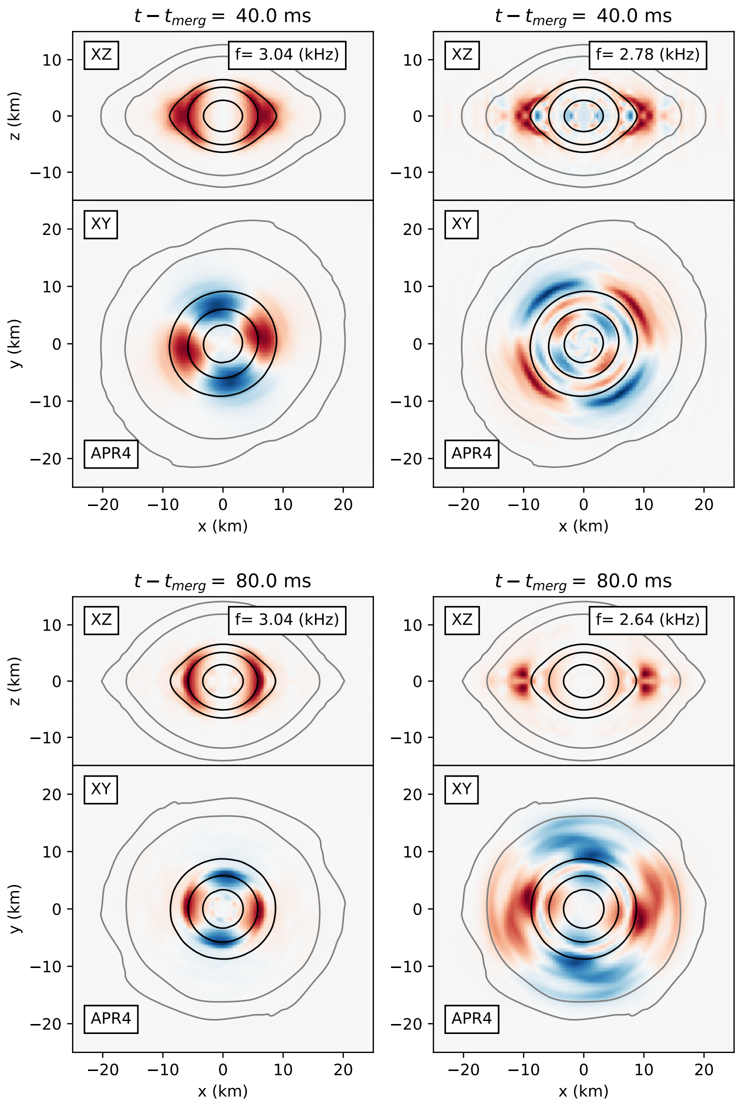

Figure 4.13: Density eigenfunctions in the XY and XZ plane of the APR4 model at 40 ms (top) and 80 ms (bottom). The black and gray lines are the isocontours of the rest-mass density. In the left column of each frame it is shown the $m = 2$ $f-$mode and the right one corresponds to an inertial mode. Each panel is normalized to the maximum value of the density eigenfunctions.

We just mentioned that the inertial modes that we observe in the late phase of the post-merger phase of our BNS simulations are due to convective instabilities in the outer regions of the remnant. In order to identify local

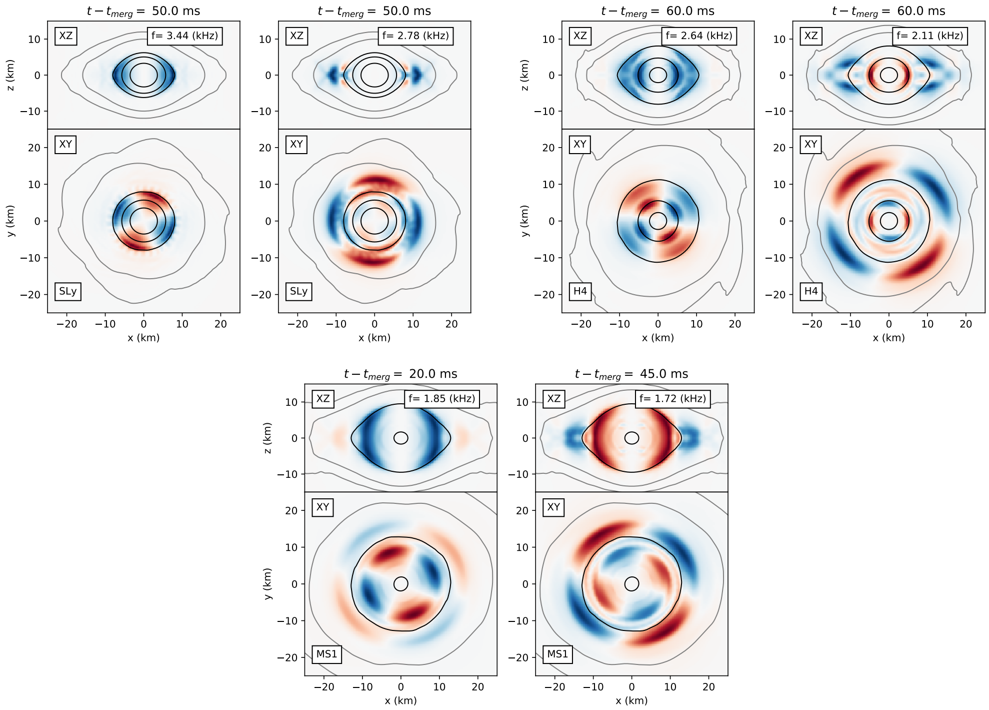

Figure 4.14: Density eigenfunctions in the XY and XZ plane of the SLy model (top-left), H4 (top-right), MS1 (bottom).

convective instabilities, we compute the Schwarzschild discriminant A_α as

$$a_\alpha = \frac{1}{\epsilon + p}\nabla_\alpha \epsilon - \frac{1}{\Gamma_1 p}\nabla_\alpha p, \tag{4.2}$$

where

$$\Gamma_1 := \frac{\epsilon + p}{p}\left(\frac{\mathrm{d}p}{\mathrm{d}\epsilon}\right)_s = \left(\frac{\mathrm{d}\ln p}{\mathrm{d}\ln \rho}\right)_s \tag{4.3}$$

is the adiabatic index around a pseudo-barotropic equilibrium. Therefore, regions where $A_\alpha < 0$ are convectively stable, while where $A_\alpha > 0$ the star is convectively *unstable*. Therefore, we computed A_r in the equatorial plane at different times and we report the results in figure 4.15. Here, the darker regions corresponds to $A_r > 0$, each row represents a different equation of state and the columns are the different times at which the Schwarzschild discriminant is computed.

In first row of figure 4.15 we observe that for the SLy model the remnant is stable up to $\sim$ 35 ms as the GW spectrum is dominated by the main $m = 2$ $f-$mode. After $\sim$ 39 ms a convective unstable ring appear in the outer layer of the ring, which is visible also in the second panel of the third row of figure 4.11. This coincides with the first appearance of inertial modes. The convective unstable ring has expanded after $\sim$ 65 ms to the lower-density regions of the remnant and appears fragmented, which is in correspondence with the strong growth of an inertial mode at 2.38 kHz. The amplitude of the mode remains almost constant, while the convective unstable regions keep expanding until the remnant finally collapses to BH.

In the second row of figure 4.15, where the Schwarzschild discriminant of the H4 model is displayed, the situation is slightly different from the case of the SLy EOS. At around ~ 32 ms we note some unstable regions in the outer layer, which are due to the hot spots (similar to that visible in figure 4.11 in the case of SLy) generated by the shock heating produced during the merger. The unstable ring appears at ~ 45 ms after the merger, located just outside the core, and corresponds to the growth of the inertial mode with frequency 2.11 kHz. The unstable regions expand, becoming fragmented at a later time, while the amplitude of the inertial mode continue to grow until the collapse to BH.

The third row of figure 4.15 shows the evolution of the Schwarzschild discriminant for the APR4 model. At first glance, it appears to be similar to the case of the SLy EOS, but the crucial difference is in the first panel of this row. Although the entire remnant appears to be stable an additional mode is active at ~ 35 ms, as it has already been discussed. The reason why an excited mode is active despite no instability is visible at this time, is the presence of a corotating region as it is shown in figure 4.9. Then, the APR4 model behaves similarly to the SLy one, where the convectively unstable ring forms a few milliseconds before the appearance of the inertial modes. Then, the expansion of the unstable regions to to lower density envelope of the remnant, leads to the growth in amplitude of such modes.

The last row of figure 4.15 displays the Schwarzschild discriminant of the MS1 model. We note that convectively unstable regions are present in the post-merger remnant from earlier times than the other three models. For this model, the mechanism of excitation-saturation-destruction of a lower-frequency inertial mode already starts earlier than the ones shown in this figure.

What we notice in our simulations is that convection excites specific, global inertial modes. This is not an unexpected behaviour [153, 154, 155, 156]. We observe that the inertial modes are excited when the temperature profile in the remnant has become nearly axisymmetric (see figure 4.11), and by that time, the amplitude of the peak $m = 2$ $f-$mode has diminished. On the other hand, the initial strongly non-axisymmetric temperature pattern (two hot spots around the deformed core) does not seem to lead to the excitation of global modes.

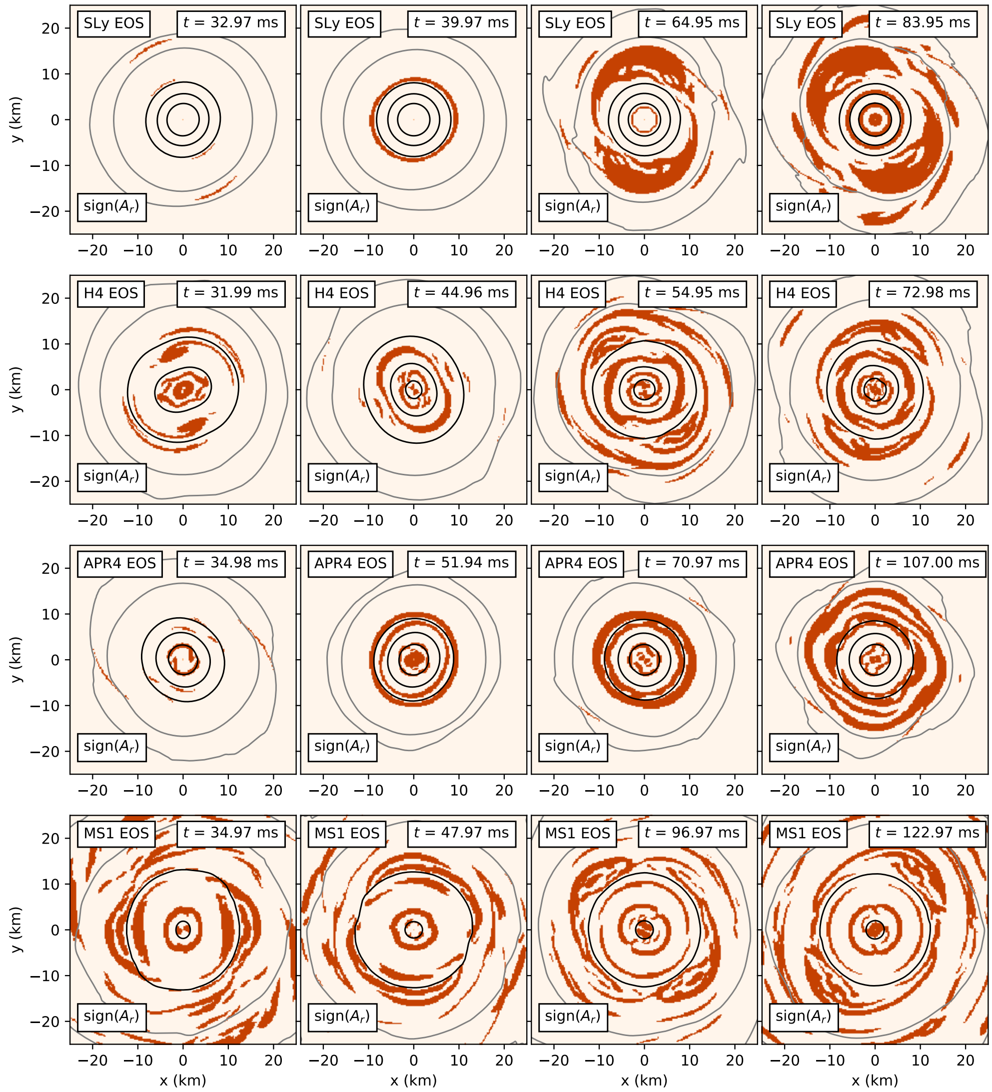

Figure 4.15: Snapshots of the Schwarzschild discriminant A_r in the equatorial plane. Each row corresponds to a different EOS model and each column to a different time (relative to the merger). Darker regions indicate that $A_r > 0$, which corresponds to convective instability (see text for details).

4.2.3 Time-frequency analysis using the continuous wavelet transform

In the previous section we presented the results of the time-frequency analysis of the gravitational wave signal extracted from our numerical simulations using the ESPRIT Prony's method. However, this method has the limit of creating a lot of artifacts that make frequencies hard to recognize, as in the case of the MS1 EOS, and it is not consistent in computing the modes amplitude.

For that reason, we tested an alternative method to perform time-frequency analysis that is the continuous wavelet transform (CWT). This method, like the Fourier transform, uses inner products to measure the similarity between a signal and an analyzing function, but is based on a *wavelet* as the analyzing function ψ, instead of a complex exponential. In the following paragraph we will make a short introduction (see [39] and references therein for all the details) to this method, and presenting some preliminary result using the GW signal extracted from the simulations already discussed in previous sections.

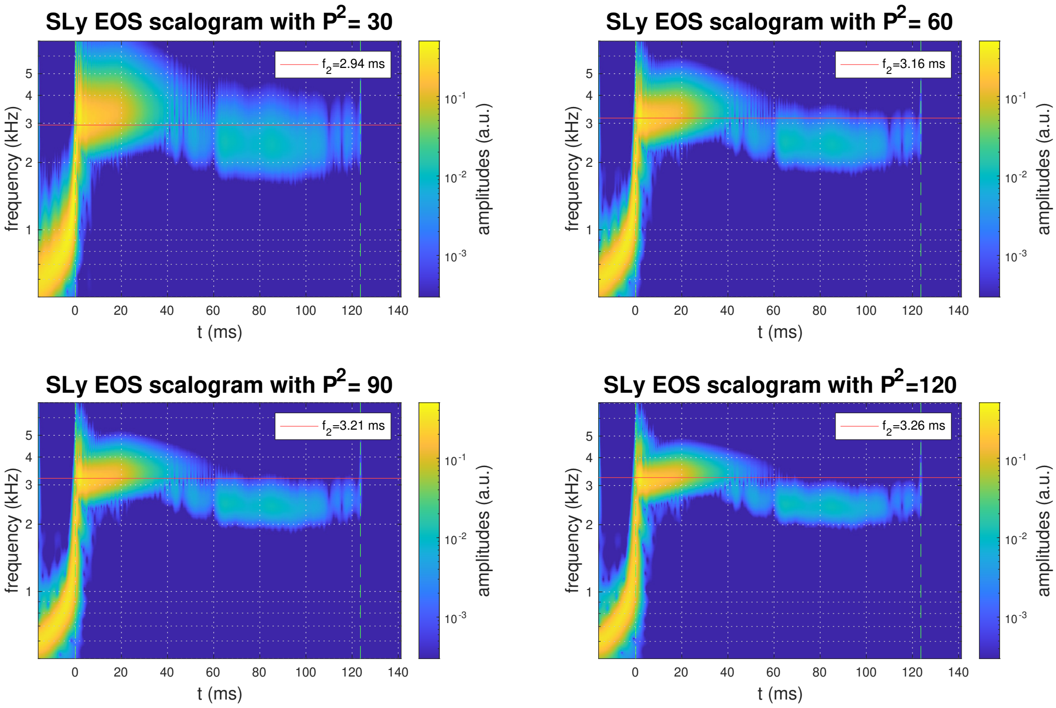

Figure 4.16: CWT of the SLy model at different values of the time-bandwith P^2. Green vertical lines mark the merger time and the time to collapse to BH, while the red horizontal line indicate the value of the main $m = 2$ $f-$mode discussed in the previous section. Yellow regions corresponds to higher values of the transform coefficients.

The continuous wavelet transform of a signal $x(t)$ is defined, in a similar way to the Fourier transform, as:

$$W_\psi(t,s) \equiv \int_{-\infty}^{\infty} \frac{1}{s^n}\psi^*\left(\frac{\tau - t}{s}\right) x(\tau) d\tau, \tag{4.4}$$

where s is the scale parameter, t is the position parameter, n is the scale normalization parameter (which is set to 1 in our case as in [39]), and ψ^* refers to the complex conjugate of the wavelet ψ. The scale parameter s is the one the regulates the stretching or dilatation of the wavelet ψ, selecting the frequency range of the wavelet: e. g. a high value of s means that the wavelet is more stretched and with low frequency.

To answer the more practical question of *which wavelet to use for a particular application*, it has been shown in [39] that the generalized Morse wavelets [157, 158, 159] are a suitable choice that unify all other wavelets that are currently known. The definition of this wavelet in the frequency domain is:

$$\psi_{\beta,\gamma}(\omega) = \int_{-\infty}^{\infty} \psi_{\beta,\gamma}(t) e^{-i\omega t} dt = U(\omega) a_{\beta,\gamma} \omega^{\beta} e^{-} \omega^{\gamma}, \tag{4.5}$$

where $a_{\beta,\gamma}$ is a normalization constant, $U(\omega)$ is the unit step function, and β and γ are the two parameters controlling the wavelet form. The decision of what wavelet to use is greatly simplified by examining the roles of β and γ in modifying the wavelet form. Varying the values of β and γ, the generalized Morse wavelet can take on a wide variety of forms, in addition to the scaling factor s which dilates or compresses a given wavelet. The frequency-domain wavelets obtain a maximum value at the *peak frequency* $\omega_{\beta,\gamma} \equiv \left(\frac{\beta}{\gamma}\right)^{1/\gamma}$, which is determined by the frequency at which the derivative of $\psi_{\beta,\gamma}(\omega)$ vanishes. Another key parameter is the rescaled second derivative of the frequency-domain wavelet evaluated at its peak frequency:

$$P^2_{\beta,\gamma} \equiv -\frac{\omega^2_{\beta,\gamma} \psi''_{\beta,\gamma}(\omega_{\beta,\gamma})}{\psi_{\beta,\gamma}(\omega_{\beta,\gamma})} = \beta\gamma. \tag{4.6}$$

In [159] it is shown that $\frac{P^2_{\beta,\gamma}}{\pi}$ is the number of oscillations at the peak frequency that fit within the central window of the time-domain. This is why $P_{\beta,\gamma}$ is also called the *duration* of the wavelet.

This method for time-frequency analysis of a signal is implemented by MATLAB signal processing tool in the *cwt* command, with the only difference that the scale parameter s is defined as 2^{ν}, where ν is the number of *voices per octave* and can be set by the user. At this point it is necessary to make a choice for β, γ and ν in order to be able to run the cwt command. Figure 4.17 shows the effect of the scale parameter on the CWT, where for a lower value corresponds a low resolution scalogram of the CWT coefficients. In effect, a low value of ν means that the wavelet is stretched, resulting in a very low precision in time and frequency, since the signal contains modes at fairly high frequencies. For that reason the optimal choice for our purpose is $\nu = 48$, which is also the maximum value for the type of Morse wavelet that we used.

Once we fixed the only parameter we need for the transform, P^2 (see equation (4.6)) and γ were the parameters left open to define the Morse wavelet function. First, the choice for γ was due to the discussion made in [159], where the Morse wavelet with $\gamma = 3$ (namely the Airy wavelet) was found to be the most Gaussian, most time/frequency concentrated, and symmetric of the family of Morse wavelets with integer γ. For that reason, this choice is the best for general purpose applications. At this point, P^2, which is also called *time-bandwith*, needs to be chosen accordingly since we are working on

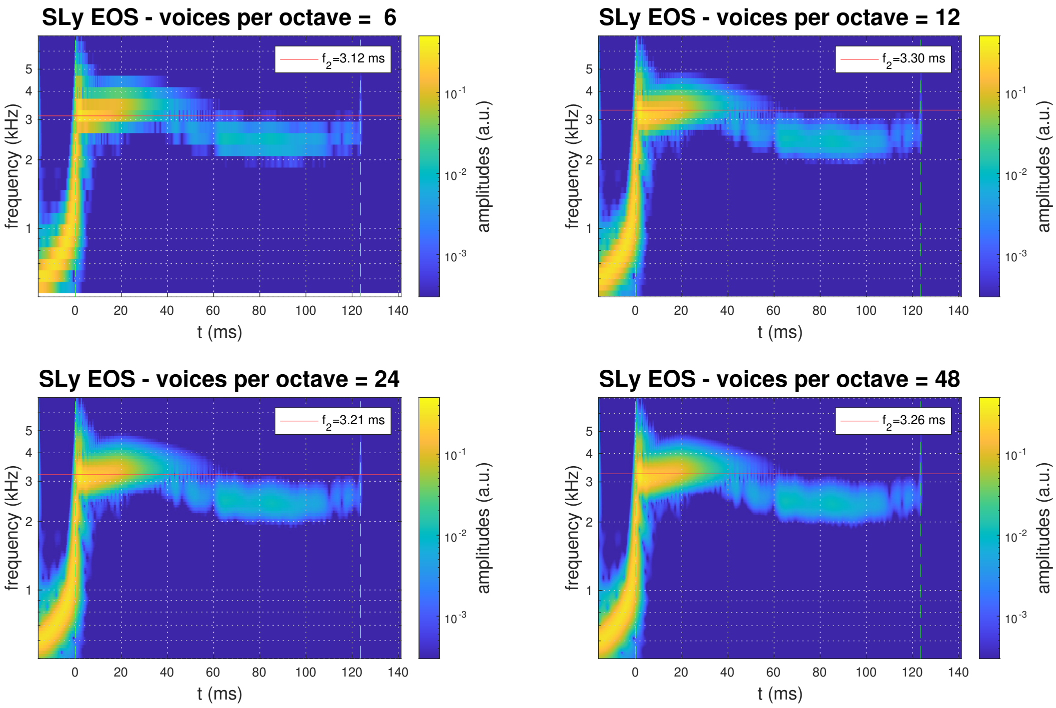

Figure 4.17: CWT of the SLy model at different values of the voices per octave ν. Green vertical lines mark the merger time and the time to collapse to BH, while the red horizontal line indicate the value of the main $m = 2$ $f-$mode discussed in the previous section. Yellow regions corresponds to higher values of the transform coefficients.

high frequency signals with small, rapid variations in their mode frequency. In figure 4.16 it is shown the effect of changing the time-bandwidth P^2 on the CWT coefficients. We observe that for a smaller value of P^2 the yellow area around the main $m = 2$ $f-$mode is significantly wider, and the frequency that is found using this method is smaller. Since the CWT method is a windowed technique for time-frequency analysis (like the short time Fourier transform), setting a smaller window in which the wavelet can oscillate means reducing its ability to resolve frequency changes. For that reason, the best choice is the highest value shown in figure 4.16.

Figure 4.18 shows the time-frequency analysis of the four models studied in this section using the CWT method, instead of the STFT or Prony's method. It is clear that while mode recognition is not as simple as in the Prony's method case, the overall dynamics of the GW signal is well reproduced and the inertial modes are clearly recognizable. In effect, in figure 4.18 the pink lines represent the mode analysis made using Prony's method, which perfectly fits the information retrieved using the CWT one. Moreover, since for Prony's method one cannot recover information on the amplitude of the modes in a reliable manner, this method provides a simple tool to identify the amplitude of a mode and follow its evolution.

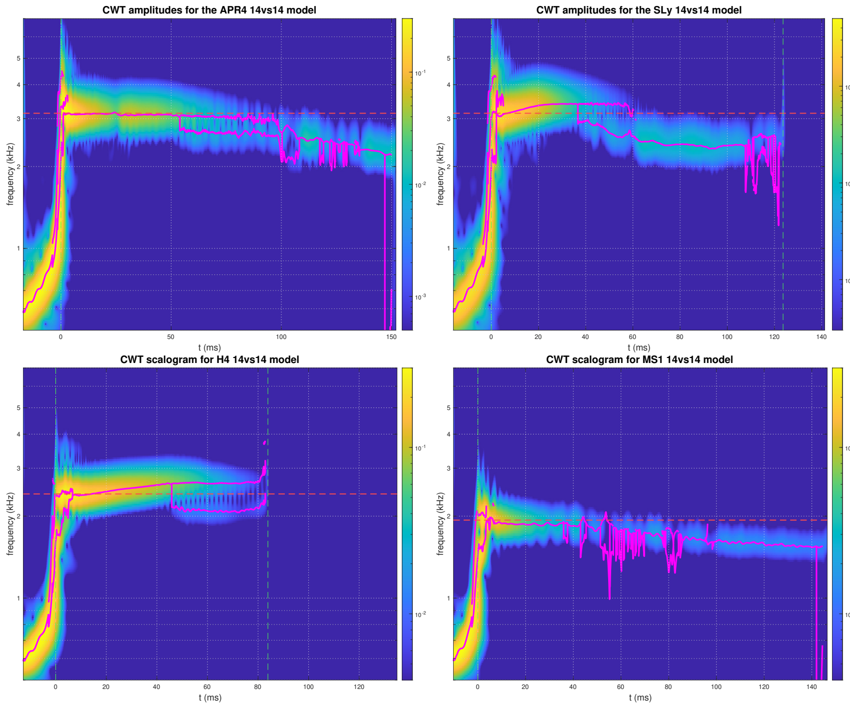

Figure 4.18: Continuous wavelet transform scalogram with $\gamma = 3$, $P^2 = 120$ for the four model discussed in this section. Horizontal red line indicates the main $m = 2$ $f-$mode, whereas vertical green lines refers to the merger time and the time to collapse to BH (if present) relative to the merger time. The pink lines represent the mode analysis made using Prony's method as presented in 4.2.2 and, in particular, 4.12.

4.2.4 Overview of the GW signature of all the simulations run by the Parma group

In the previous sections of this chapter, many binary neutron star systems that could be either long-living after the merger or collapsing to black hole at earlier times were presented, as it was the case for some system of 4.1.2. Here, we gathered all the simulations run by the Parma group also in [67] and we used the same methods of section 4.2.2 and 4.2.3 in order to draw a more general picture of the gravitational wave signature of the post-merger phase.

This set of BNS mergers simulations includes both the long-living equal mass models that have already been presented in this work, and different combination of total mass for the SLy EOS as well as unequal mass models for SLy, APR4, H4 and MS1 EOS at the spatial grid resolution of $dx = 369\,\mathrm{m}$. The parameters of these BNS systems can be found in table V of [67]. To this set, it was added the SFHo 1.30vs1.30 model of [37] since also a run at $dx = 369\,\mathrm{m}$ resolution was available.

Figure 4.19 shows the full spectra of the models described in [67], using a FFT technique and plotting the power spectral density of the signal for an

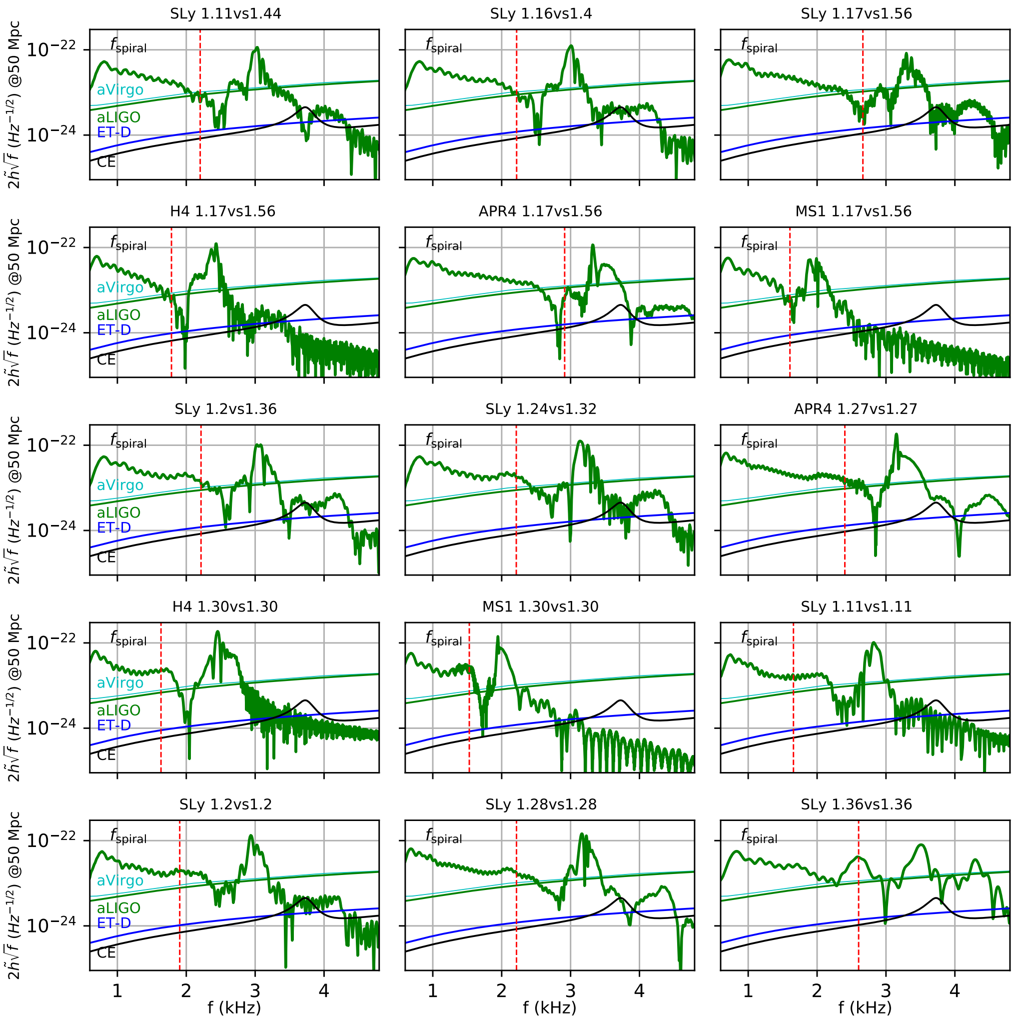

Figure 4.19: Full spectra of the models presented in [67], where the power spectral density of the signal is considered at 50 Mpc with optimal orientation. The frequency of the spiral mode $f_{\rm spiral}$ is highlighted by the dashed red line, while the labeled solid lines represent the design sensitivities of Advanced Virgo, Advanced LIGO, Einstein Telescope, and Cosmic Explorer, as in figure 4.7 and 4.8.

observer at 50 Mpc at optimal orientation, as in figure 4.7 and 4.8. We observe that all the spectra present (at least) a major peak in the $2-3.5$ kHz range due to the main quadrupolar mode, f_2, which is the dominant mode in the post-merger phase. In the case of the model with SLy EOS and total mass of $2.72M_\odot$(SLy 1.36vs1.36) we note that the peaks of the f_{2-0} and f_{2+0} modes are clearly recognizable, which is due to the fact that the remnant collapses to BH just ~ 7 ms after merger. On the other hand, the contribution at lower frequencies represents the dynamics of the (late) inspiral and merger of the binary neutron star systems, where the spiral deformed remnant rotates at

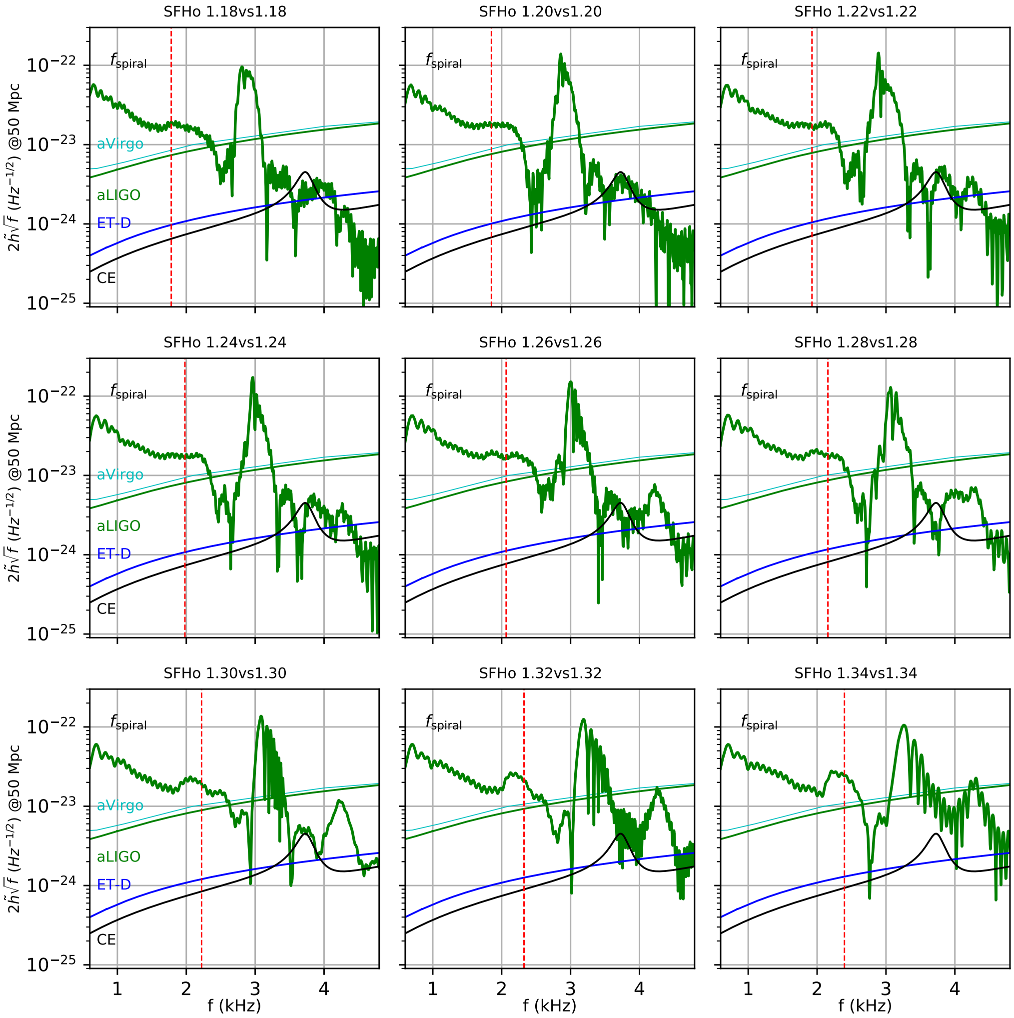

Figure 4.20: Full spectra of the GW signal of the SFHo models of [37] that live more than 10 ms after merger , where the power spectral density of the signal is considered at 50 Mpc with optimal orientation. The frequency of the spiral mode $f_{\rm spiral}$ is highlighted by the dashed red line, while the labeled solid lines represent the design sensitivities of Advanced Virgo, Advanced LIGO, Einstein Telescope, and Cosmic Explorer, as in figure 4.7 and 4.8.

a defined frequency $f_{\rm spiral}$ (red dashed line). Although, in most cases, this value cannot be detected directly by the spectrum of the GW signal, it can be computed using the universal relation proposed in [32]:

$$f^U_{\rm spiral} = 6.16 - 82.1 \cdot C + 358 \cdot C^2, \tag{4.7}$$

where C is the ratio M/R, or the *compactness* of the star. An alternative is given in [34]:

$$f^T_{\mathrm{spiral}} = 3.58 - 8.68 \cdot C + 174 \cdot C^2 \tag{4.8}$$
$$- 2.34 \cdot M + 0.99 \cdot M^2 - 13.0 \cdot C \cdot M. \tag{4.9}$$

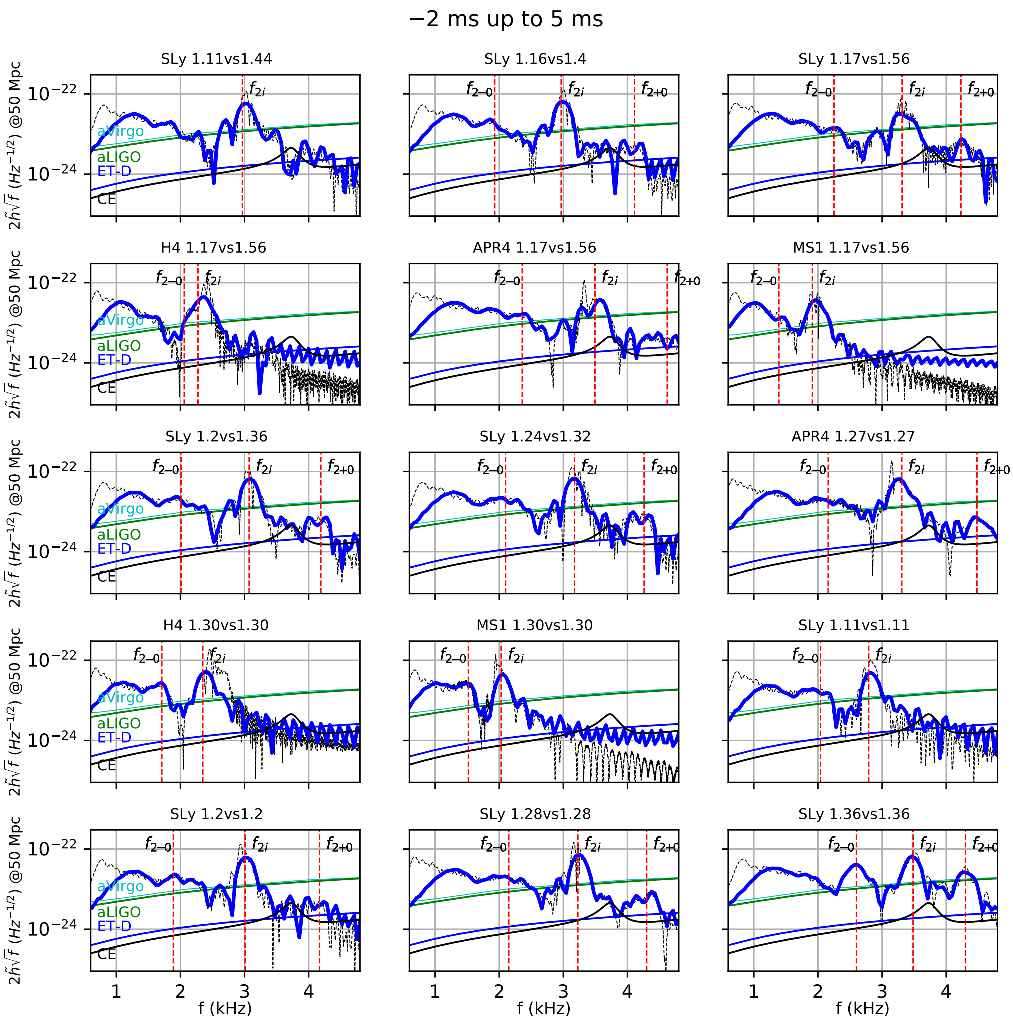

Figure 4.21: Spectrum of the GW signal of the models in [67] in the $[-2, 5]$ ms time window relative to the merger time of each model. The black dashed line in the background refers to the full spectrum, as in 4.19. Vertical dashed red lines represent the main f-mode, f_{2i}, and the subdominant f_{2-0} and f_{2+0} modes, where present.

In figure 4.21 the spectra of these models have been computed only in the time window $[-2, 5]$ ms in order to highlight the properties of the GW signal at the merger. In effect, we observe that in any case, the frequency associated to the dominant quadrupolar mode f_2, which is labeled as f_{2i} in this first phase of the merger dynamics, is visible. In most of the models shown in

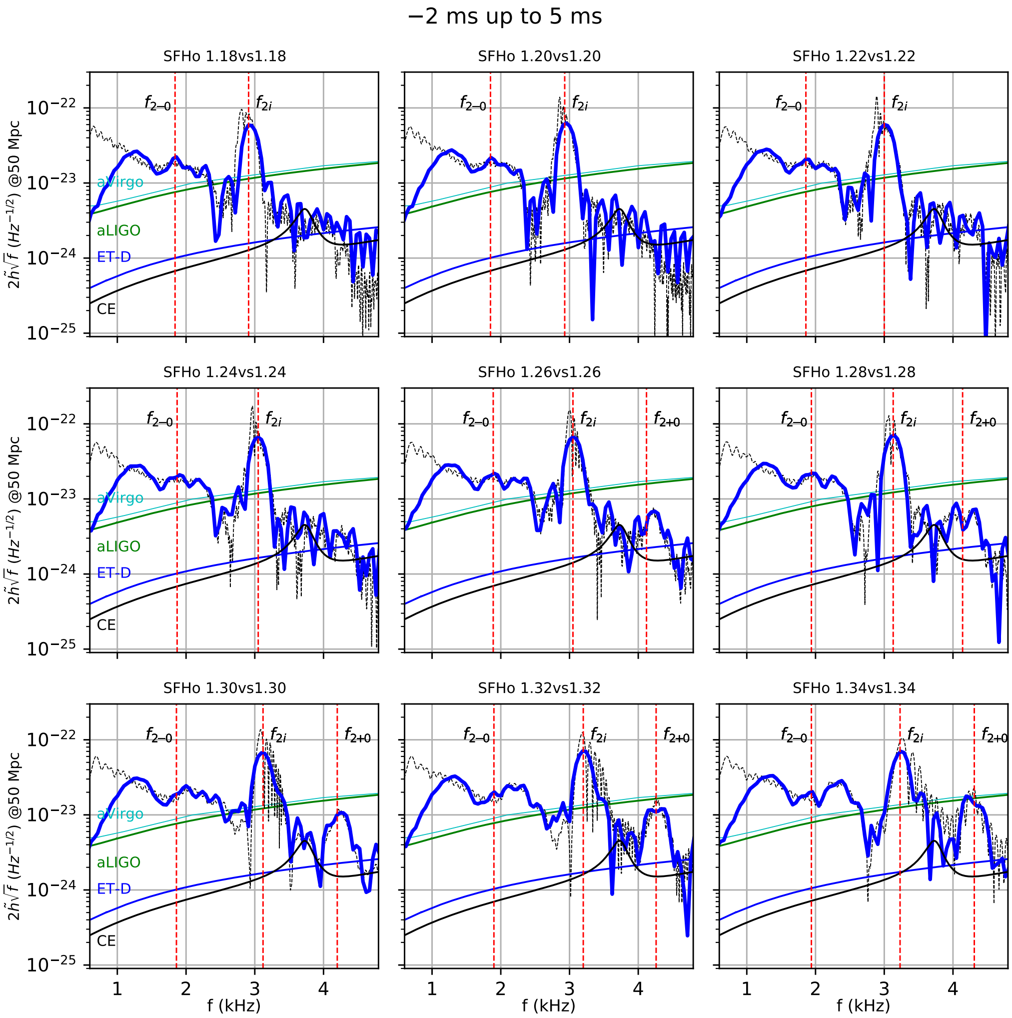

Figure 4.22: Spectrum of the GW signal of the SFHo models of [37] that live more than 10 ms after merger in the $[-2, 5]$ ms time window relative to the merger time of each model. The black dashed line in the background refers to the full spectrum, as in 4.19. Vertical dashed red lines represent the main f-mode, f_{2i}, and the subdominant f_{2-0} and f_{2+0} modes, where present.

this figure, we also note that the peaks related to the interaction between the quadrupolar and the quasi-radial oscillation f_{2-0} and f_{2+0} can be recognized. However, in the case of extremely unequal masses or low compactness (H4 a.17vs1.56, MS1 1.17vs1.56, H4 1.30vs1.30, MS1 1.30vs1.30), these peaks are not clearly visible and can be confused with the one associated with the spiral deformation of the regions around the double-core structure. As for the case of $f_{\rm spiral}$, the frequencies of these modes can also be computed using universal relations. In [32], the predictions of the unified model also include:

$$f^U_{\rm peak} = 2.33 - 28.1 \cdot C + 199 \cdot C^2 \tag{4.10}$$
$$f^U_{2-0} = 5.95 - 88.3 \cdot C + 392 \cdot C^2. \tag{4.11}$$

In [34] it is also introduced a relations that allows to compute f_1, or f_{2-0}:

$$f^T_1 = -22.07 + 466.62 \cdot C - 3131.63 \cdot C^2 + 7210.01 \cdot C^3. \tag{4.12}$$

The most recent proposal of a relations between the mode frequencies f_1 and f_2, and the compactness C has been given in [160]:

$$f^R_1 = -35.17 + 727.99 \cdot C - 4858.54 \cdot C^2 + 10989.88 \cdot C^3, \tag{4.13}$$
$$f^R_2 = -3.12 + 51.90 \cdot C - 89.07 \cdot C^2. \tag{4.14}$$

From the analysis of the following time window of the GW spectra in figure 4.23, we observe three crucial aspects:

1. the peaks associated to the interaction between the main quadrupolar mode and the quasi-radial oscillations are not present;
2. the frequency of the main f-mode, f_2, is slightly (of the order of 10^2 Hz) shifted towards the higher frequencies;
3. in the case of extremely unequal mass models, a secondary peak in the $1.5 - 2$ kHz range is clearly recognizable.

The first point has already been explained in detail in section 4.1.2 and it is basically due to the fact that these interaction modes between the quadrupolar mode and the quasi-radial oscillations live just a few milliseconds after merger (damping time ≤ 3 ms). The second one was observed also in section 4.2.2, for the long-living remnants, and is even more clear in figure 4.25, where the results of the analysis made using Prony's method are overlapped to the CWT scalogram of the GW signal. In fact, both the red lines and the maximum of the CWT amplitude slightly increase with time for all the models considered in [67]. The third point becomes extremely clear in figure 4.25 for models SLy 1.17vs1.56 at ~ 1.66 kHz, APR4 1.17vs1.56 at ~ 1.70 kHz, and in figure 4.23 for H4 1.17vs1.56 at ~ 1.71 kHz. In fact, we observe a lighter band (=larger amplitude) below the yellow one, in the frequency range $[1.5, 2]$ kHz, which does not correspond to the one associated with the f_{2-0} mode. This peculiarity of unequal mass models, especially those with extreme mass ratios and larger compactness, can be explained by the shape of the remnant, which is indeed not axisymmetric and spirally deformed. For that reason, the $f_{\rm spiral}$ mode remains stronger throughout all this first phase of the post-merger dynamics and could also be observed by third generation detectors like Einstein Telescope and Cosmic Explorer.

Models	f_2	f_0	f_1	f_{2i}	f_3	f_1^{CWT}	f_{2i}^{CWT}	f_3^{CWT}	f_{peak}^U	f_{spiral}^U	f_{2-0}^U	f_1^T	f_{spiral}^T	f_1^R	f_2^R
SLy 1.11vs1.11	2.852	1.311	2.04	2.791		2.05	2.891		2.257	1.657	1.241	1.641	2.041	1.657	2.360
SLy 1.20vs1.20	2.964	1.311	1.89	3.009	4.17	1.85	3.073	4.10	2.598	1.905	1.531	1.798	2.176	1.804	2.664
SLy 1.28vs1.28	3.172	1.178	2.15	3.227	4.30	2.08	3.390	4.60	2.957	2.215	1.887	1.966	2.333	1.958	2.921
SLy 1.36vs1.36	3.506	0.933	2.60	3.483	4.30	2.58	3.450	4.28	3.358	2.603	2.329	2.211	2.521	2.210	3.156
SLy 1.11vs1.44	2.998	1.267		2.967		1.96	3.073		2.943	2.202	1.872	1.959	2.332	1.951	2.911
SLy 1.16vs1.40	2.984	1.245	1.93	2.967	4.11	1.83	3.030	4.28	2.959	2.217	1.890	1.968	2.336	1.960	2.922
SLy 1.20vs1.36	3.047	1.200	2.01	3.072	4.19	1.96	3.001	4.41	2.956	2.214	1.886	1.966	2.333	1.958	2.920
SLy 1.24vs1.32	3.131	1.178	2.10	3.175	4.26	2.02	3.164	4.54	2.953	2.212	1.883	1.965	2.331	1.957	2.919
APR4 1.17vs1.56	3.317	1.133	2.36	3.494	4.62	2.37	3.708		3.657	2.914	2.681	2.449	2.756	2.478	3.305
SLy 1.17vs1.56	3.270	1.022	2.25	3.312	4.23	2.24	3.303		3.418	2.665	2.399	2.256	2.559	2.258	3.188
H4 1.17vs1.56	2.370	1.022	2.06	2.274			2.370		2.443	1.785	1.391	1.730	1.758	1.743	2.535
MS1 1.17vs1.56	1.902	1.422	1.39	1.913		1.43	1.993		2.171	1.606	1.179	1.594	1.539	1.606	2.271
APR4 1.27vs1.27	3.166	1.267	2.16	3.307	4.48	2.00	3.210	4.67	3.155	2.403	2.101	2.078	2.513	2.069	3.043
H4 1.30vs1.30	2.448	1.023	1.71	2.349		1.75	2.440		2.218	1.633	1.212	1.620	1.674	1.635	2.320
MS1 1.30vs1.30	2.023	1.089	1.52	2.031		1.52	2.081		2.024	1.530	1.087	1.494	1.506	1.489	2.100
SFHo 1.30vs1.30	3.164	1.066	2.02	3.136	4.29	2.02	3.210	4.47	1.895	2.964	2.222	1.970	2.303	1.962	2.927

Table 4.5: Summary of the gravitational wave signature for all the models taken into consideration in this work at a spatial grid resolution of $dx = 369$ m. f_0, f_2, f_1, f_{2i}, f_3 are the values extracted from the spectra made with the Fourier transform, whereas the ones with the superscript *CWT* refers to the frequencies extracted from the CWT scalogram (see figure 4.25), and U (see eqs. (4.9) and (4.11)), T (see eqs. (4.9) and (4.12)), R (see eqs. (4.14)) to different universal relations proposed in the literature.

Models	f_2	f_0	f_1	f_{2i}	f_3	f_1^{CWT}	f_{2i}^{CWT}	f_3^{CWT}	f_{peak}^U	f_{spiral}^U	f_{2-0}^U	f_1^T	f_{spiral}^T	f_1^R	f_2^R
SFHo 1.18vs1.18	2.803	0.984	1.84	2.913		1.80	2.943		2.690	1.980	1.616	1.838	2.179	1.840	2.736
SFHo 1.20vs1.20	2.842	0.964	1.85	2.931		1.73	2.986		2.530	1.851	1.468	1.768	2.115	1.778	2.610
SFHo 1.22vs1.22	2.881	1.166	1.86	3.005		1.78	3.029		2.624	1.926	1.555	1.809	2.161	1.815	2.686
SFHo 1.24vs1.24	2.956	1.149	1.87	3.052		1.78	3.073		2.689	1.979	1.616	1.838	2.179	1.840	2.736
SFHo 1.26vs1.26	3.022	1.141	1.89	3.056	4.12	1.85	3.029	4.22	2.789	2.065	1.715	1.884	2.228	1.881	2.809
SFHo 1.28vs1.28	3.102	1.089	1.94	3.134	4.14	1.94	3.164	4.16	2.893	2.157	1.820	1.934	2.280	1.927	2.880
SFHo 1.30vs1.30	3.135	1.085	1.86	3.120	4.20	1.99	3.118	4.35	2.964	2.222	1.895	1.970	2.303	1.962	2.927
SFHo 1.32vs1.32	3.250	1.062	1.90	3.201	4.26	2.11	3.164	4.35	3.074	2.324	2.012	2.030	2.358	2.021	2.996
SFHo 1.34vs1.34	3.373	1.017	1.94	3.238	4.31	2.14	3.210	4.35	3.149	2.396	2.094	2.074	2.384	2.074	3.041

Table 4.6: Summary of the gravitational wave signature for the SFHo models of [37] that live at least 10 ms after merger. The simulations have a spatial grid spacing of $dx = 277$ m. Frequencies are obtained the same way as in table 4.5

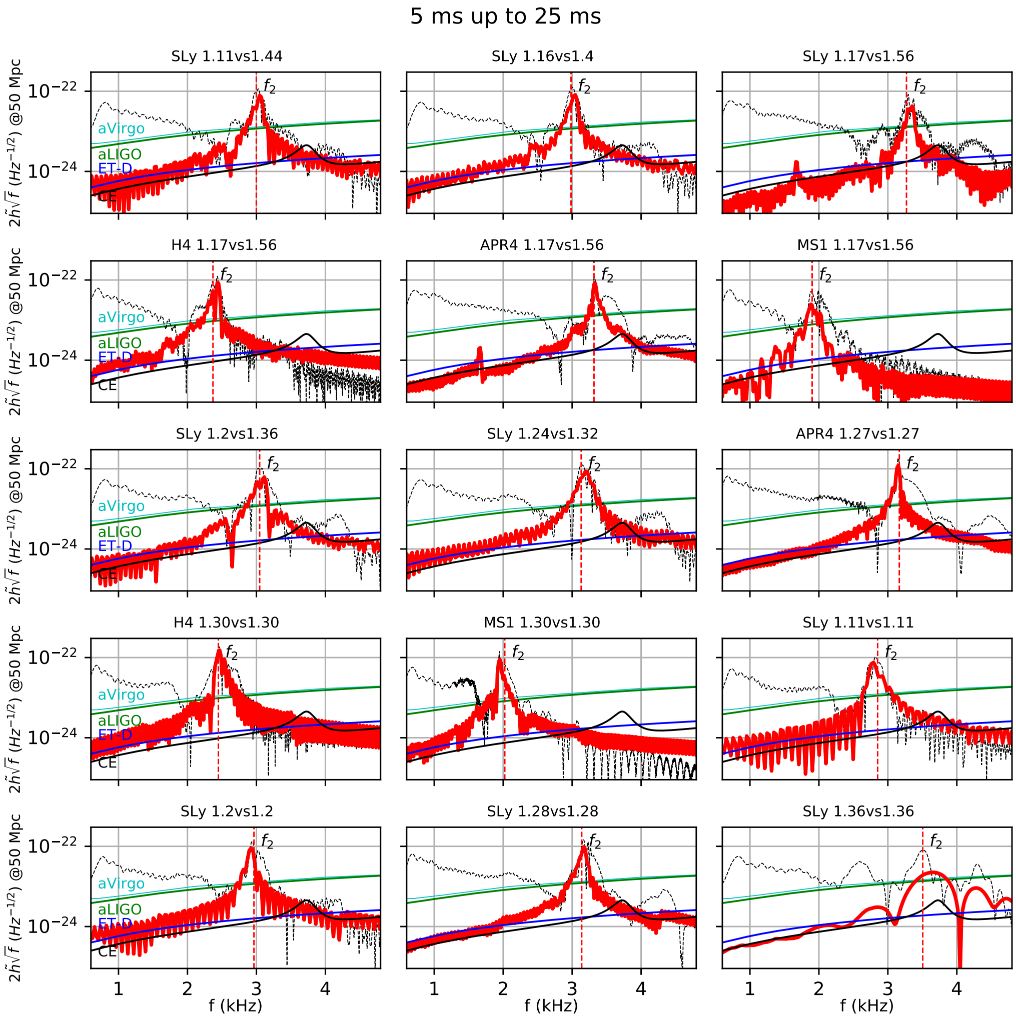

Figure 4.23: Spectrum of the GW signal of the models in [67] in the $[5, 25]$ ms time window relative to the merger time of each model. The black dashed line in the background refers to the full spectrum, as in 4.19. Vertical dashed red lines represent the main f-mode f_2.

The results of this analysis are then summarized in table 4.5. In this table, we included the values obtained by the analysis of the FFT spectrum (f_0, f_2, f_1, f_{2i}, f_3), those extracted from the CWT amplitudes (f_1^{CWT}, f_2^{CWT},f_3^{CWT}), those computed using the relations of [32] (U superscript), [34] (T superscript) and [160] (R superscript). In the appendix of [67] the authors noted that the predictions of the universal relations differ from the measured values of about $10 - 15\%$, showing overall agreement for each model, including the SFHo 1.30vs1.30 one that has been discussed in the previous sections. The modes frequencies identified using the continuous wavelet transform are in agreement both with the models predictions and those measured using FFT, with differences of $\sim 10\%$. However, due to the poor resolution of the CWT

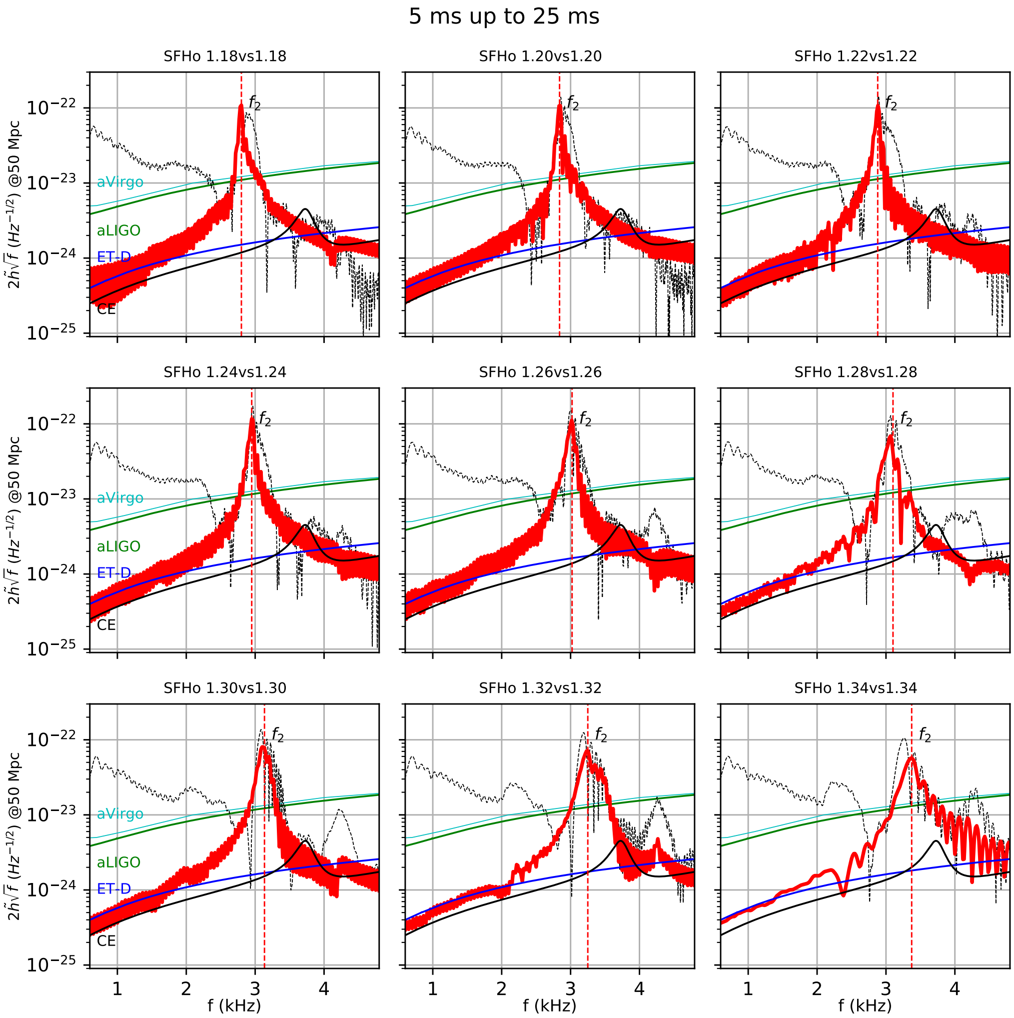

Figure 4.24: Spectrum of the GW signal of the SFHo models of [37] that live more than 10 ms after merger in the $[5, 25]$ ms time window relative to the merger time of each model. The black dashed line in the background refers to the full spectrum, as in 4.19. Vertical dashed red lines represent the main f-mode, f_{2i}, and the subdominant f_{2-0} and f_{2+0} modes, where present.

in the frequency domain for higher frequencies, it was not always possible to identify f_{2+0}, especially for the models with extreme mass ratios. In fact, this mode appears to be 2 up to 10 times weaker than f_{2-0}, revealing what could be a limit for this time-frequency technique.

The same procedure has been applied to the models presented in section 4.1 and also in [37], considering only the case of the SFHo EOS with total mass from $2.36M_{\odot}$up to $2.68M_{\odot}$at the spatial grid resolution of $dx = 277\,\mathrm{m}$. The choice of these models is justified by the fact that these are the only models whose remnant live longer than 10 ms after merger, in order to look at the

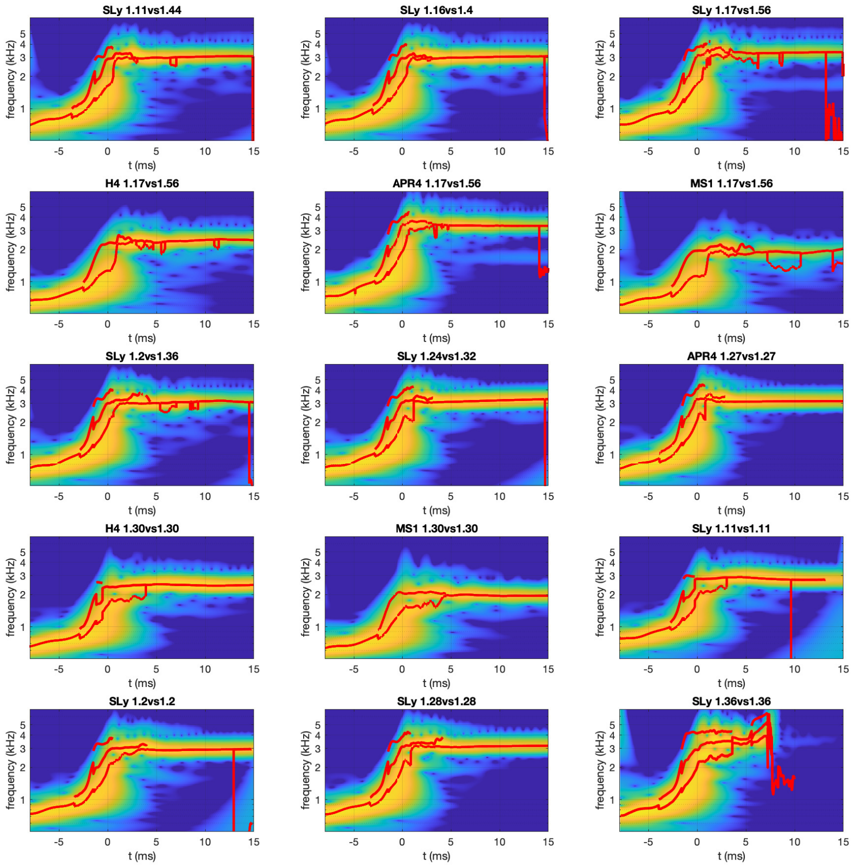

Figure 4.25: Continuous wavelet transform scalogram with $\gamma = 3$, $P^2 = 120$ of the models discussed in [67]. The red line represents the mode analysis made using Prony's method.

post-merger dynamics as well. The full spectra of this set of simulations is displayed in figure 4.20, where also the dashed red line represents $f_{\rm spiral}$, which is computed using (4.7). Figures 4.22 and 4.24 show the same spectra, but referring only to specific time windows, i.e. $[-2, 5]$ ms and $[5, 25]$ ms respectively. In this case we note that as the frequency peaks related to f_{2-0}, f_{2i}, f_{2+0}, and f_2 are visible (dashed red lines), also a small peak at the same frequency of $f_{\rm spiral}$ can be identified near f_{2-0} at a slightly higher frequency (just 0.1 kHz higher). Moreover, in figure 4.24 we observe that for the models with total mass $2.60M_{\odot}$and $2.64M_{\odot}$the f_{2+0} mode is still active, since a small peak at $\sim$ 4.2 kHz is still recognizable. The CWT picture (see figure 4.26) and the Prony analysis of the GW signal of this set of simulations confirms this behavior for the heavier systems. The detailed look at all the features of the post-merger characteristics of the GW signal of such systems is given by

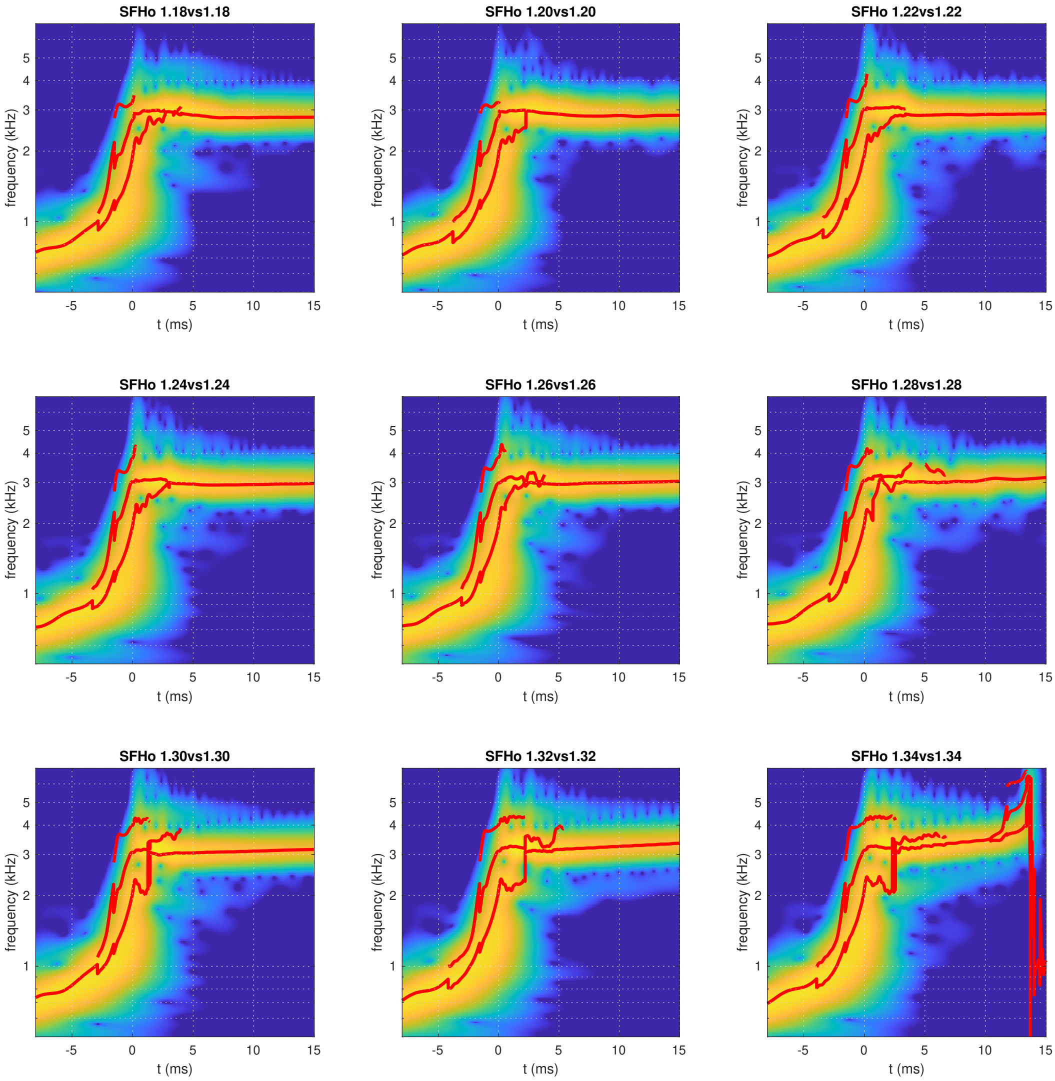

Figure 4.26: Continuous wavelet transform scalogram with $\gamma = 3$, $P^2 = 120$ of the models with SFHo EOS discussed in [37] that live at least 10 ms after merger. The red line represents the mode analysis made using Prony's method.

table 4.6, where all the data taken from the GW analysis and the predictions of the proposed relations are reported. Here we observe that even at this spatial resolution the difference between the values identified using the FFT spectra and the CWT scalogram have at worst a 10% discrepancy. On the other hand, the relations in [32, 34, 160] used to compute frequencies seems to improve as compactness increases (see also table 4.5), especially for f^U_{2-0}, which in the case of SFHo 1.20vs1.20 has a 30% difference from the measured value.

Chapter 5

Conclusions

The work presented in this thesis focuses on the physical properties of neutron stars through the study of the gravitational waves signal during the post-merger phase, in order to extract the signature of the signal that will be detected by the next generation of GW detectors (Einstein Telescope and Cosmic Explorer). To achieve this goal, an extensive set of numerical simulations of binary neutron star mergers was performed. The gravitational-waves signal was analyzed during all the three phases of the systems' evolution, but a particular focus was put in the post-merger phase, where, in case the system does not promptly collapse to black hole, important information on the thermal and rotational properties of the star can be retrieved.

The main results obtained in this work are:

A clear division of the post-merger phase into three separated steps: the early post-merger, where oscillational modes appears and matter is dynamically ejected; the intermediate post-merger where the dynamics of the remnant is led only by the mass and EOS depending f_2 mode; the late post-merger phase, where convective instability regions of the remnant trigger inertial modes.

The first part of this work had the focus to study the features of binary neutron star systems in the early stages of the post-merger using a wide set of numerical simulations of equal mass systems that could either end up directly collapsing to black hole or forming a hypermassive neutron star remnant. It has been shown that matter is dynamically ejected from the neutron star system during the collision of the two objects and its quantity depend on the system's equation of state and total mass, as well as for the disk mass once the black hole is formed. In particular, systems that directly collapsed to black hole showed a drastically reduced matter ejection and disk mass. During this phase of the post-merger, the gravitational wave signal can also show secondary peaks in the spectrum that have been found to be a nonlinear combination of the main quadrupolar mode and the quasi-radial one. The results that have been presented in this work are in agreement with the existing literature.

The second part of this work was focused on the investigation of the physical properties of neutron stars in the intermediate to late phase of the merger, which needed long-time simulations of systems that formed a long-living remnant. The four models that have been studied with that purpose, including two cases of delayed collapse to black hole (more than $\sim$ 80 ms after the merger), showed that the dominant mode of the intermediate post-merger phase is the $m = 2$ $f-$mode, which is the only mode contributing to GW emission in this phase even if with decaying amplitude.In some particular case, also a phenomenon of corotation of the mode with the remnant occurs, leading to a strong revival in the GW emission in the intermediate phase of the evolution. In a later phase, convective unstable regions start to grow in the outer layers of the remnant, leading to the excitation of inertial modes via a mechanism of excitation-saturation-destruction in most cases. The latest stages of the simulated time are characterized only by the inertial modes which become the only cause of gravitational wave emission. The frequencies of this inertial modes are expected to be detectable by third generation detectors like Einstein Telescope and Cosmic Explorer, which will help to broaden the knowledge on neutron star physics.

The last part of this work was mainly focused on improving the methods used to perform the time-frequency analysis of the gravitational wave signal, especially for the mode analysis on the inertial modes. Preliminary studies on the use of the continuous wavelet transform as a useful tool for investigating the features of GW signal has been done, resulting in good agreement with the previous results. Also, this method proved to be significantly faster (in the order of seconds) than Prony's method (in the order of minutes/hours, depending on the simulation's resolution). This technique, together with Prony's method and the classic FFT, was then used to perform the analysis of all the BNS models performed by the Parma group and some common properties have been discovered. It was pointed out that the modes associated to the interaction between the quadrupole and the quasi-radial oscillation disappear after a few milliseconds after merger. Also, unequal mass models, in particular for extreme mass ratios, presented a spiral mode even at later times after merger in the range of $[1.5, 2]$ kHz that it was not recognizable using just Prony's method.

Acknowledgements

I wish to acknowledge the help received during these three years (and some extra time) of Ph.D. studies, which has been fundamental for the development of this thesis.
First and foremost, I must thank my supervisor, Prof. Roberto De Pietri, for accepting me in his research group since my Master's thesis, supporting me during these years and teaching me a lot about the physics of neutron stars and the computational aspects of these astrophysical objects, and for guiding me during the not-so-easy process of this Ph.D. I could not have asked for a better guidance and a better person to support me during these years, from my Master's thesis to this Ph.D.. I should also thank him for giving me the opportunity to participate to schools and conferences, such as the GR22-AMALDI13 in 2019, which was a once-in-a-lifetime opportunity for me.
I also must thank Alessandra Feo, Frank Löffler, Nikolaos Stergioulas, José Antonio Font, Alessandro Drago, Giuseppe Pagliara and Silvia Traversi, whose contribution to the results presented in this thesis was fundamental.
I thank INFN for giving me the financial support to travel to conferences and schools and mainly for giving me the opportunity to work on the MARCONI cluster at CINECA, without which this work would not exists.
I want to thank all the people that I met during these years of school and conferences for teaching me a lot and pushing my limits.
I special thank goes to Emilio, Alberto, Simone, Valentina, Silvio, Silvia, Andrea and Fabiana, that spent with me their time in Parma and were a fundamental presence also during bad times.
I also want to thank all the university basketball team of the final phase of the national championship in L'Aqulia, since they probably helped me achieve the highest results in sports that I could have ever had achieved in my life.
Finally, I want to thank Giulia, who is a new arrival in my life, for helping me a lot during the first lockdown due to the COVID pandemic and supporting me every minute during the process of writing of this thesis.

Appendix A

Comparison of simulations at different resolutions

The accuracy of the simulations that have been discussed in this thesis and the convergence of the code has already been discussed in [64]. In this appendix we make a comparison among the long-term evolution of the four models using different resolutions: $dx = 368$ m, $dx = 277$ m and $dx = 185$ m for the SLy EOS, and $dx = 368$ m and $dx = 277$ m for the APR4, H4 and MS1 EOS models.

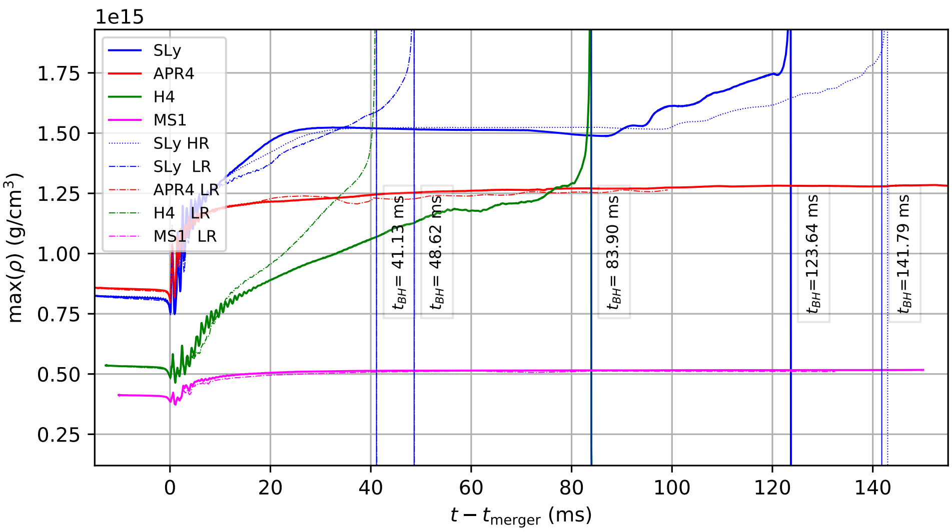

Figure A.1: Picture of the evolution of the maximum density as in figure 4.10 at different resolutions for each model. *LR* refers to $dx = 368$ m and *HR* refers to $dx = 185$ m.

Figure A.2 shows the spectrogram and Prony's analysis for the SLy model at three different resolutions, where the central one is the one reported for every simulation discussed in chapter 4. The data shown in this figure show that the appearance of the convective instabilities, and the excitation of inertial modes, which are associated to this phenomenon (see section 4.2.2), happens at somewhat later times as the resolution is increased. Similarly, the black hole formation occurs at later times as the grid spacing decreases, as discussed in [64]. Also, we observe only one episode of excitation-saturation-destruction at $dx = 368$ m, while three (instead of two) at $dx = 277$ m. The fact that at the lowest resolution, this mode is immediately suppressed is due to the collapse to BH, which occurs a lot earlier than at standard and high resolution thanks to the smaller numerical dissipation. For the highest resolution ($dx = 185$ m), the inertial mode appears somewhat later and at a slightly higher frequency than for $dx = 277$ m and $dx = 368$ m since the smallest dissipation leads to a slightly different hydrodynamical evolution. However, the resolution does not strongly affect the frequency of the main $f-$mode.

In figure A.3 we show the spectrogram and Prony's analysis for the other three models, namely APR4, H4 and MS1, at different resolutions. For these models the highest resolution is not available due to the computational cost of such high resolution simulations. We note that the overall behaviour is similar to the SLy case for both the mode evolution and the collapse to BH, in the case of the H4 model. For the APR4 model, we observe that the frequencies of the visible modes are slightly lower at low resolution, while the inertial modes appear somewhat earlier in the evolution, surviving until the end. For the H4 case, the collapse to BH does not allow inertial modes to appear. The MS1 model show a similar behaviour as the APR4 case, since the inertial modes appear earlier in the evolution and survive throughout the entire evolution.

In figure A.1 we report the data for the maximum density evolution for all the resolution considered in this appendix. We note that a significantly different behaviour is visible only for those models which collapse to BH, where the numerical dissipation plays an important role in the preservation of the angular momentum. In effect, at low resolution the models collapse to BH significantly earlier than at standard resolution. However, the qualitative features between the resolutions remain the same.

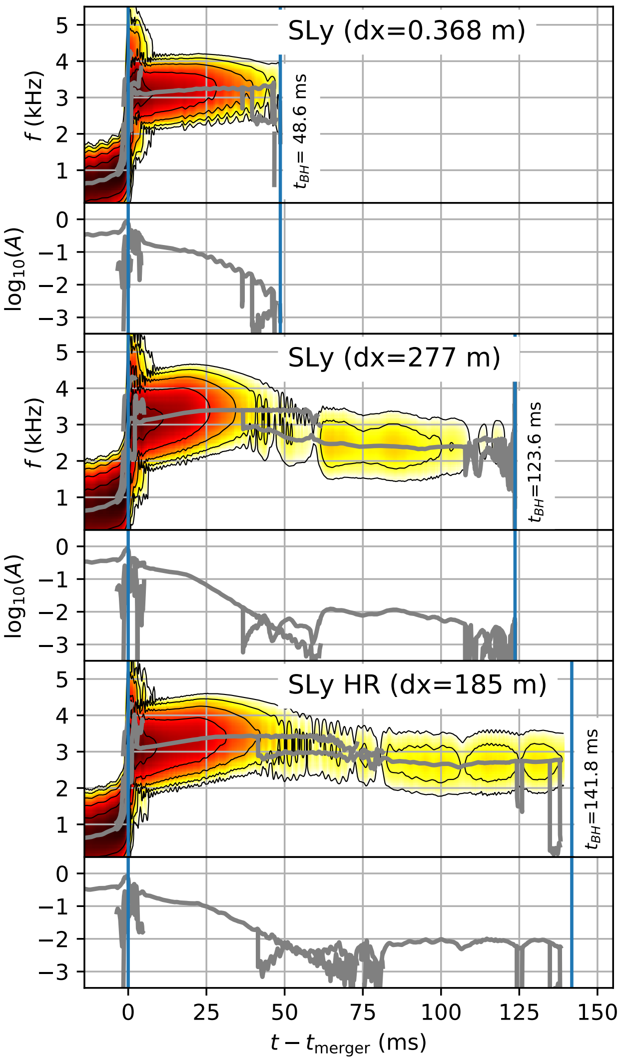

Figure A.2: Comparison among the time-frequency analysis of the SLy model using Prony's method at different resolutions. Top panel refers to the resolution $dx = 0.25$ CU, middle panel to $dx = 0.1875$ and bottom panel to $dx = 0.125$.

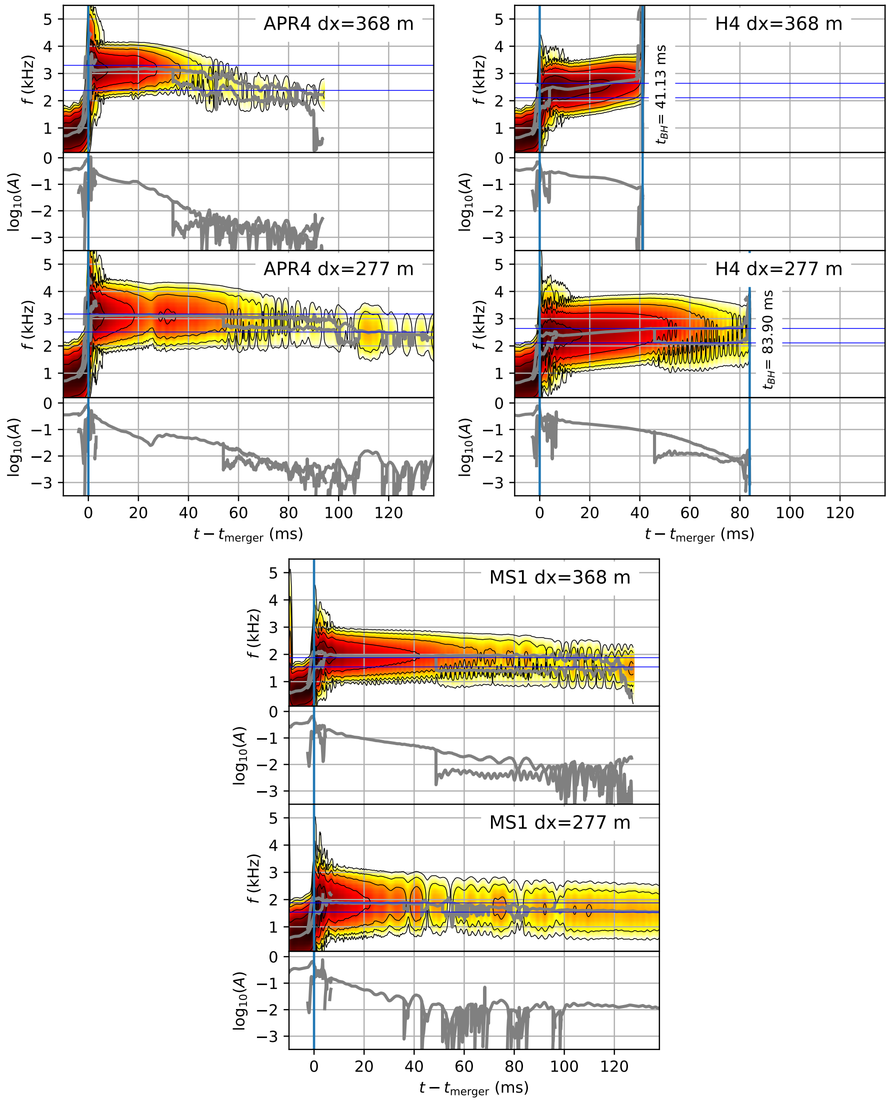

Figure A.3: Same as figure A.2 for the APR4 (top-left), H4 (top-right) and MS1 (bottom) models. Resolutions are reported in each panel.

Bibliography

[1] B. P. Abbott *et al.*, “Binary black hole mergers in the first advanced ligo observing run,” *Phys. Rev. X*, vol. 6, p. 041015, Oct 2016.

[2] B. P. Abbott *et al.*, “Observation of gravitational waves from a binary black hole merger,” *Phys. Rev. Lett.*, vol. 116, p. 061102, Feb 2016.

[3] R. o. Abbott, “Gw190521: A binary black hole merger with a total mass of 150 $M_{\odot}$,” *Phys. Rev. Lett.*, vol. 125, p. 101102, Sep 2020.

[4] B. P. Abbott *et al.*, “Multi-messenger observations of a binary neutron star merger,” *The Astrophysical Journal*, vol. 848, p. L12, oct 2017.

[5] B. P. Abbott *et al.*, “Prospects for observing and localizing gravitational-wave transients with advanced ligo and advanced virgo,” *Living Reviews in Relativity*, vol. 19, no. 1, p. 1, 2016.

[6] B. Abbott *et al.*, “Gravitational Waves and Gamma-rays from a Binary Neutron Star Merger: GW170817 and GRB 170817A,” *Astrophys. J. Lett.*, vol. 848, no. 2, p. L13, 2017.

[7] D. Kasen, B. Metzger, J. Barnes, E. Quataert, and E. Ramirez-Ruiz, “Origin of the heavy elements in binary neutron-star mergers from a gravitational wave event,” *Nature*, vol. 551, p. 80, 2017.

[8] B. Abbott *et al.*, “A gravitational-wave standard siren measurement of the Hubble constant,” *Nature*, vol. 551, no. 7678, pp. 85–88, 2017.

[9] E. Pian *et al.*, “Spectroscopic identification of r-process nucleosynthesis in a double neutron star merger,” *Nature*, vol. 551, pp. 67–70, 2017.

[10] B. Abbott *et al.*, “GW170817: Observation of Gravitational Waves from a Binary Neutron Star Inspiral,” *Phys. Rev. Lett.*, vol. 119, no. 16, p. 161101, 2017.

[11] B. Abbott *et al.*, “GW170817: Measurements of neutron star radii and equation of state,” *Phys. Rev. Lett.*, vol. 121, no. 16, p. 161101, 2018.

[12] B. Abbott *et al.*, “Properties of the binary neutron star merger GW170817,” *Phys. Rev. X*, vol. 9, no. 1, p. 011001, 2019.

[13] A. Bauswein and N. Stergioulas, “Spectral classification of gravitational-wave emission and equation of state constraints in binary neutron star mergers,” *J. Phys. G*, vol. 46, no. 11, p. 113002, 2019.

[14] L. Baiotti, “Gravitational waves from neutron star mergers and their relation to the nuclear equation of state,” *Prog. Part. Nucl. Phys.*, vol. 109, p. 103714, 2019.

[15] M. D. Duez, “Numerical relativity confronts compact neutron star binaries: a review and status report,” *Class. Quant. Grav.*, vol. 27, p. 114002, 2010.

[16] J. A. Faber and F. A. Rasio, “Binary Neutron Star Mergers,” *Living Rev. Rel.*, vol. 15, p. 8, 2012.

[17] V. Paschalidis, “General relativistic simulations of compact binary mergers as engines for short gamma-ray bursts,” *Class. Quant. Grav.*, vol. 34, no. 8, p. 084002, 2017.

[18] L. Baiotti and L. Rezzolla, “Binary neutron star mergers: a review of Einstein’s richest laboratory,” *Rept. Prog. Phys.*, vol. 80, no. 9, p. 096901, 2017.

[19] T. W. Baumgarte, S. L. Shapiro, and M. Shibata, “On the maximum mass of differentially rotating neutron stars,” *Astrophys. J. Lett.*, vol. 528, p. L29, 2000.

[20] G. B. Cook, S. L. Shapiro, and S. A. Teukolsky, “Spin-up of a Rapidly Rotating Star by Angular Momentum Loss: Effects of General Relativity,” *The Astrophysical Journal*, vol. 398, p. 203, Oct. 1992.

[21] E. Gourgoulhon, P. Grandclement, K. Taniguchi, J.-A. Marck, and S. Bonazzola, “Quasiequilibrium sequences of synchronized and irrotational binary neutron stars in general relativity: 1. Method and tests,” *Phys. Rev. D*, vol. 63, p. 064029, 2001.

[22] S. Bonazzola, E. Gourgoulhon, and J.-A. Marck, “Numerical models of irrotational binary neutron stars in general relativity,” *Phys. Rev. Lett.*, vol. 82, pp. 892–895, 1999.

[23] F. Loffler *et al.*, “The Einstein Toolkit: A Community Computational Infrastructure for Relativistic Astrophysics,” *Class. Quant. Grav.*, vol. 29, p. 115001, 2012.

[24] J. Aasi *et al.*, “Advanced LIGO,” *Class. Quant. Grav.*, vol. 32, p. 074001, 2015.

[25] F. Acernese *et al.*, "Advanced Virgo: a second-generation interferometric gravitational wave detector," *Class. Quant. Grav.*, vol. 32, no. 2, p. 024001, 2015.

[26] B. P. Abbott *et al.*, "Search for Post-merger Gravitational Waves from the Remnant of the Binary Neutron Star Merger GW170817," *Astrophys. J. Lett.*, vol. 851, no. 1, p. L16, 2017.

[27] B. Abbott *et al.*, "Search for gravitational waves from a long-lived remnant of the binary neutron star merger GW170817," *Astrophys. J.*, vol. 875, no. 2, p. 160, 2019.

[28] M. Shibata and K. Uryu, "Gravitational waves from the merger of binary neutron stars in a fully general relativistic simulation," *Prog. Theor. Phys.*, vol. 107, p. 265, 2002.

[29] N. Stergioulas, A. Bauswein, K. Zagkouris, and H.-T. Janka, "Gravitational waves and nonaxisymmetric oscillation modes in mergers of compact object binaries," *Mon. Not. Roy. Astron. Soc.*, vol. 418, p. 427, 2011.

[30] A. Bauswein and H.-T. Janka, "Measuring neutron-star properties via gravitational waves from binary mergers," *Phys. Rev. Lett.*, vol. 108, p. 011101, 2012.

[31] A. Bauswein, H. Janka, K. Hebeler, and A. Schwenk, "Equation-of-state dependence of the gravitational-wave signal from the ring-down phase of neutron-star mergers," *Phys. Rev. D*, vol. 86, p. 063001, 2012.

[32] A. Bauswein and N. Stergioulas, "Unified picture of the post-merger dynamics and gravitational wave emission in neutron star mergers," *Phys. Rev. D*, vol. 91, no. 12, p. 124056, 2015.

[33] L. Lehner, S. L. Liebling, C. Palenzuela, O. Caballero, E. O'Connor, M. Anderson, and D. Neilsen, "Unequal mass binary neutron star mergers and multimessenger signals," *Class. Quant. Grav.*, vol. 33, no. 18, p. 184002, 2016.

[34] L. Rezzolla and K. Takami, "Gravitational-wave signal from binary neutron stars: a systematic analysis of the spectral properties," *Phys. Rev. D*, vol. 93, no. 12, p. 124051, 2016.

[35] F. Maione, *Gravitational-wave signal from binary neutron star merger simulations with different equation of state and mass ratio.* PhD thesis, Parma U., 2017.

[36] R. De Pietri, A. Feo, J. A. Font, F. Löffler, F. Maione, M. Pasquali, and N. Stergioulas, "Convective Excitation of Inertial Modes in Binary Neutron Star Mergers," *Phys. Rev. Lett.*, vol. 120, no. 22, p. 221101, 2018.

[37] R. De Pietri, A. Drago, A. Feo, G. Pagliara, M. Pasquali, S. Traversi, and G. Wiktorowicz, "Merger of compact stars in the two-families scenario," *Astrophys. J.*, vol. 881, no. 2, p. 122, 2019.

[38] R. De Pietri, A. Feo, J. A. Font, F. Löffler, M. Pasquali, and N. Stergioulas, "Numerical-relativity simulations of long-lived remnants of binary neutron star mergers," *Phys. Rev. D*, vol. 101, no. 6, p. 064052, 2020.

[39] J. M. Lilly and S. C. Olhede, "Generalized morse wavelets as a superfamily of analytic wavelets," *IEEE Transactions on Signal Processing*, vol. 60, no. 11, pp. 6036–6041, 2012.

[40] J. M. Lattimer and M. Prakash, "The physics of neutron stars," *Science*, vol. 304, no. 5670, pp. 536–542, 2004.

[41] B. D. Lackey, M. Nayyar, and B. J. Owen, "Observational constraints on hyperons in neutron stars," *Phys. Rev. D*, vol. 73, p. 024021, Jan 2006.

[42] S. Weissenborn, I. Sagert, G. Pagliara, M. Hempel, and J. Schaffner-Bielich, "Quark matter in massive compact stars," *The Astrophysical Journal*, vol. 740, p. L14, sep 2011.

[43] J. R. Oppenheimer and G. M. Volkoff, "On massive neutron cores," *Phys. Rev.*, vol. 55, pp. 374–381, Feb 1939.

[44] R. C. Tolman, "Static solutions of einstein's field equations for spheres of fluid," *Phys. Rev.*, vol. 55, pp. 364–373, Feb 1939.

[45] B. K. Harrison, K. S. Thorne, M. Wakano, and J. A. Wheeler, *Gravitation theory and gravitational collapse.* Chicago (Ill.) : University of Chicago press, 1965.

[46] A. Burrows, "Supernova explosions in the universe," *Nature*, vol. 403, pp. 727–733, 2000.

[47] H. A. Bethe and J. R. Wilson, "Revival of a stalled supernova shock by neutrino heating," *ApJ*, vol. 295, pp. 14–23, Aug. 1985.

[48] C. D. Ott, E. Abdikamalov, P. Mösta, R. Haas, S. Drasco, E. P. O'Connor, C. Reisswig, C. A. Meakin, and E. Schnetter, "General-relativistic simulations of three-dimensional core-collapse supernovae," *The Astrophysical Journal*, vol. 768, p. 115, apr 2013.

[49] F. Hanke, B. Müller, A. Wongwathanarat, A. Marek, and H.-T. Janka, "SASI activity in three-dimensional neutrino-hydrodynamics simulations of supernova cores," *The Astrophysical Journal*, vol. 770, p. 66, may 2013.

[50] P. Mösta, S. Richers, C. D. Ott, R. Haas, A. L. Piro, K. Boydstun, E. Abdikamalov, C. Reisswig, and E. Schnetter, "Magnetorotational core-collapse supernovae in three dimensions," *The Astrophysical Journal*, vol. 785, p. L29, apr 2014.

[51] P. Mösta, C. D. Ott, D. Radice, L. F. Roberts, E. Schnetter, and R. Haas, "A large-scale dynamo and magnetoturbulence in rapidly rotating core-collapse supernovae," *Nature*, vol. 528, pp. 376–379, Dec 2015.

[52] C. D. Ott, "The gravitational-wave signature of core-collapse supernovae," *Classical and Quantum Gravity*, vol. 26, p. 063001, feb 2009.

[53] V. Ferrari, G. Miniutti, and J. A. Pons, "Gravitational waves from newly born, hot neutron stars," *Monthly Notices of the Royal Astronomical Society*, vol. 342, pp. 629–638, 06 2003.

[54] G. F. Burgio, V. Ferrari, L. Gualtieri, and H.-J. Schulze, "Oscillations of hot, young neutron stars: Gravitational wave frequencies and damping times," *Phys. Rev. D*, vol. 84, p. 044017, Aug 2011.

[55] J. Fuller, H. Klion, E. Abdikamalov, and C. D. Ott, "Supernova seismology: gravitational wave signatures of rapidly rotating core collapse," *Monthly Notices of the Royal Astronomical Society*, vol. 450, pp. 414–427, 04 2015.

[56] J. A. Pons, S. Reddy, M. Prakash, J. M. Lattimer, and J. A. Miralles, "Evolution of proto–neutron stars," *The Astrophysical Journal*, vol. 513, pp. 780–804, mar 1999.

[57] G. Camelio, L. Gualtieri, J. A. Pons, and V. Ferrari, "Spin evolution of a proto-neutron star," *Phys. Rev. D*, vol. 94, p. 024008, Jul 2016.

[58] P. Haensel, A. Potekhin, and D. Yakovlev, *Neutron stars 1: Equation of state and structure*, vol. 326. New York, USA: Springer, 2007.

[59] F. Douchin and P. Haensel, "Inner edge of neutron star crust with SLY effective nucleon-nucleon interactions," *Phys. Lett. B*, vol. 485, pp. 107–114, 2000.

[60] F. Douchin and P. Haensel, "A unified equation of state of dense matter and neutron star structure," *Astronomy and Astrophysics*, vol. 380, pp. 151–167, Dec. 2001.

[61] A. Akmal, V. R. Pandharipande, and D. G. Ravenhall, “Equation of state of nucleon matter and neutron star structure,” *Phys. Rev. C*, vol. 58, pp. 1804–1828, Sep 1998.

[62] H. Mueller and B. D. Serot, “Relativistic mean field theory and the high density nuclear equation of state,” *Nucl. Phys. A*, vol. 606, pp. 508–537, 1996.

[63] A. W. Steiner, M. Hempel, and T. Fischer, “Core-collapse supernova equations of state based on neutron star observations,” *Astrophys. J.*, vol. 774, p. 17, 2013.

[64] R. De Pietri, A. Feo, F. Maione, and F. Löffler, “Modeling Equal and Unequal Mass Binary Neutron Star Mergers Using Public Codes,” *Phys. Rev. D*, vol. 93, no. 6, p. 064047, 2016.

[65] F. Maione, R. De Pietri, A. Feo, and F. Löffler, “Binary neutron star merger simulations with different initial orbital frequency and equation of state,” *Class. Quant. Grav.*, vol. 33, no. 17, p. 175009, 2016.

[66] A. Feo, R. De Pietri, F. Maione, and F. Löffler, “Modeling Mergers of Known Galactic Systems of Binary Neutron Stars,” *Class. Quant. Grav.*, vol. 34, no. 3, p. 034001, 2017.

[67] F. Maione, R. De Pietri, A. Feo, and F. Löffler, “Spectral analysis of gravitational waves from binary neutron star merger remnants,” *Phys. Rev. D*, vol. 96, p. 063011, 2017.

[68] A. W. Steiner, M. Prakash, J. M. Lattimer, and P. J. Ellis, “Isospin asymmetry in nuclei and neutron stars [review article],” *Physics Reports*, vol. 411, pp. 325–375, June 2005.

[69] P. B. Demorest, T. Pennucci, S. M. Ransom, M. S. E. Roberts, and J. W. T. Hessels, “A two-solar-mass neutron star measured using Shapiro delay,” *Nature*, vol. 467, pp. 1081–1083, Oct. 2010.

[70] A. W. Steiner, J. M. Lattimer, and E. F. Brown, “The Equation of State from Observed Masses and Radii of Neutron Stars,” *Astrophys. J.*, vol. 722, pp. 33–54, 2010.

[71] M. Hempel, T. Fischer, J. Schaffner-Bielich, and M. Liebendorfer, “New Equations of State in Simulations of Core-Collapse Supernovae,” *Astrophys. J.*, vol. 748, p. 70, 2012.

[72] K. Hebeler, J. M. Lattimer, C. J. Pethick, and A. Schwenk, “Constraints on neutron star radii based on chiral effective field theory interactions,” *Phys. Rev. Lett.*, vol. 105, p. 161102, Oct 2010.

[73] A. W. Steiner and S. Gandolfi, "Connecting neutron star observations to three-body forces in neutron matter and to the nuclear symmetry energy," *Phys. Rev. Lett.*, vol. 108, p. 081102, Feb 2012.

[74] J. M. Lattimer and Y. Lim, "CONSTRAINING THE SYMMETRY PARAMETERS OF THE NUCLEAR INTERACTION," *The Astrophysical Journal*, vol. 771, p. 51, jun 2013.

[75] M. B. Tsang, Y. Zhang, P. Danielewicz, M. Famiano, Z. Li, W. G. Lynch, and A. W. Steiner, "Constraints on the density dependence of the symmetry energy," *Phys. Rev. Lett.*, vol. 102, p. 122701, 2009.

[76] A. W. Steiner, J. M. Lattimer, and E. F. Brown, "THE NEUTRON STAR MASS-RADIUS RELATION AND THE EQUATION OF STATE OF DENSE MATTER," *The Astrophysical Journal*, vol. 765, p. L5, feb 2013.

[77] I. Tews, T. Krüger, K. Hebeler, and A. Schwenk, "Neutron matter at next-to-next-to-next-to-leading order in chiral effective field theory," *Phys. Rev. Lett.*, vol. 110, no. 3, p. 032504, 2013.

[78] J. S. Read, B. D. Lackey, B. J. Owen, and J. L. Friedman, "Constraints on a phenomenologically parameterized neutron-star equation of state," *Phys. Rev. D*, vol. 79, p. 124032, 2009.

[79] L. Rezzolla and O. Zanotti, *Relativistic Hydrodynamics.* 2013.

[80] F. Douchin and P. Haensel, "A unified equation of state of dense matter and neutron star structure," *Astron. Astrophys.*, vol. 380, p. 151, 2001.

[81] G. Camelio, T. Dietrich, M. Marques, and S. Rosswog, "Rotating neutron stars with nonbarotropic thermal profile," *Phys. Rev. D*, vol. 100, no. 12, p. 123001, 2019.

[82] A. Einstein, "Approximative Integration of the Field Equations of Gravitation," *Sitzungsber. Preuss. Akad. Wiss. Berlin (Math. Phys.)*, vol. 1916, pp. 688–696, 1916.

[83] R. A. Hulse and J. H. Taylor, "Discovery of a pulsar in a binary system.," *Astrophysical Journal*, vol. 195, pp. L51–L53, Jan. 1975.

[84] C. W. Misner, K. Thorne, and J. Wheeler, *Gravitation.* San Francisco: W. H. Freeman, 1973.

[85] C. Runge, "Ueber die numerische auflösung von differentialgleichungen," *Mathematische Annalen*, vol. 46, pp. 167–178, Jun 1895.

[86] W. Kutta, "Beitrag zur näherungsweisen integration totaler differentialgleichungen," *Z. Math. Phys.*, vol. 46, 1901.

[87] M. J. Berger and J. Oliger, "Adaptive Mesh Refinement for Hyperbolic Partial Differential Equations," *J. Comput. Phys.*, vol. 53, p. 484, 1984.

[88] E. Schnetter, S. H. Hawley, and I. Hawke, "Evolutions in 3-D numerical relativity using fixed mesh refinement," *Class. Quant. Grav.*, vol. 21, pp. 1465–1488, 2004.

[89] M. Campanelli, C. Lousto, P. Marronetti, and Y. Zlochower, "Accurate evolutions of orbiting black-hole binaries without excision," *Phys. Rev. Lett.*, vol. 96, p. 111101, 2006.

[90] J. G. Baker, J. Centrella, D.-I. Choi, M. Koppitz, and J. van Meter, "Gravitational wave extraction from an inspiraling configuration of merging black holes," *Phys. Rev. Lett.*, vol. 96, p. 111102, 2006.

[91] F. Pretorius, "Evolution of binary black hole spacetimes," *Phys. Rev. Lett.*, vol. 95, p. 121101, 2005.

[92] R. Arnowitt, S. Deser, and C. W. Misner, "Republication of: The dynamics of general relativity," *General Relativity and Gravitation*, vol. 40, pp. 1997–2027, Sep 2008.

[93] E. Gourgoulhon, *3+1 Formalism in General Relativity.* Springer, 2012.

[94] T. W. Baumgarte and S. L. Shapiro, "On the numerical integration of Einstein's field equations," *Phys. Rev. D*, vol. 59, p. 024007, 1999.

[95] M. Shibata and T. Nakamura, "Evolution of three-dimensional gravitational waves: Harmonic slicing case," *Phys. Rev. D*, vol. 52, pp. 5428–5444, 1995.

[96] T. Nakamura, K. Oohara, and Y. Kojima, "General Relativistic Collapse to Black Holes and Gravitational Waves from Black Holes," *Prog. Theor. Phys. Suppl.*, vol. 90, pp. 1–218, 1987.

[97] O. Sarbach, G. Calabrese, J. Pullin, and M. Tiglio, "Hyperbolicity of the BSSN system of Einstein evolution equations," *Phys. Rev. D*, vol. 66, p. 064002, 2002.

[98] G. Nagy, O. E. Ortiz, and O. A. Reula, "Strongly hyperbolic second order Einstein's evolution equations," *Phys. Rev. D*, vol. 70, p. 044012, 2004.

[99] C. Bona, J. Masso, E. Seidel, and J. Stela, "A New formalism for numerical relativity," *Phys. Rev. Lett.*, vol. 75, pp. 600–603, 1995.

[100] M. Alcubierre, B. Bruegmann, P. Diener, M. Koppitz, D. Pollney, E. Seidel, and R. Takahashi, "Gauge conditions for long term numerical black hole evolutions without excision," *Phys. Rev. D*, vol. 67, p. 084023, 2003.

[101] J. Brown, P. Diener, O. Sarbach, E. Schnetter, and M. Tiglio, "Turduckening black holes: An Analytical and computational study," *Phys. Rev. D*, vol. 79, p. 044023, 2009.

[102] S. Husa, I. Hinder, and C. Lechner, "Kranc: A Mathematica application to generate numerical codes for tensorial evolution equations," *Comput. Phys. Commun.*, vol. 174, pp. 983–1004, 2006.

[103] M. Alcubierre, G. Allen, B. Bruegmann, T. Dramlitsch, J. A. Font, P. Papadopoulos, E. Seidel, N. Stergioulas, W.-M. Suen, and R. Takahashi, "Towards a stable numerical evolution of strongly gravitating systems in general relativity: The Conformal treatments," *Phys. Rev. D*, vol. 62, p. 044034, 2000.

[104] P. Mösta, B. C. Mundim, J. A. Faber, R. Haas, S. C. Noble, T. Bode, F. Löffler, C. D. Ott, C. Reisswig, and E. Schnetter, "GRHydro: A new open source general-relativistic magnetohydrodynamics code for the Einstein Toolkit," *Class. Quant. Grav.*, vol. 31, p. 015005, 2014.

[105] L. Anton, O. Zanotti, J. A. Miralles, J. M. Marti, J. M. Ibanez, J. A. Font, and J. A. Pons, "Numerical 3+1 general relativistic magnetohydrodynamics: A Local characteristic approach," *Astrophys. J.*, vol. 637, pp. 296–312, 2006.

[106] J. A. Font, "Numerical Hydrodynamics and Magnetohydrodynamics in General Relativity," *Living Rev. Rel.*, vol. 11, p. 7, 2008.

[107] J. M. Marti, J. M. Ibanez, and J. A. Miralles, "Numerical relativistic hydrodynamics: Local characteristic approach," *Phys. Rev. D*, vol. 43, pp. 3794–3801, 1991.

[108] J. M. Martí and E. Müller, "Numerical hydrodynamics in special relativity," *Living Reviews in Relativity*, vol. 6, p. 7, Dec 2003.

[109] F. Banyuls, J. A. Font, J. M. Ibanez, J. M. Marti, and J. A. Miralles, "Numerical $\{3+1\}$ general relativistic hydrodynamics: A local characteristic approach," *The Astrophysical Journal*, vol. 476, pp. 221–231, feb 1997.

[110] S. K. Godunov, "A difference method for numerical calculation of discontinuous solutions of the equations of hydrodynamics," *Mat. Sb. (N.S.)*, vol. 47(89), pp. 271–306, 1959.

[111] P. Colella and P. R. Woodward, "The Piecewise Parabolic Method (PPM) for Gas Dynamical Simulations," *J. Comput. Phys.*, vol. 54, pp. 174–201, 1984.

[112] A. Suresh and H. Huynh, "Accurate monotonicity-preserving schemes with runge–kutta time stepping," *Journal of Computational Physics*, vol. 136, no. 1, pp. 83 – 99, 1997.

[113] X.-D. Liu, S. Osher, and T. Chan, "Weighted essentially non-oscillatory schemes," *Journal of Computational Physics*, vol. 115, no. 1, pp. 200 – 212, 1994.

[114] G.-S. Jiang and C.-W. Shu, "Efficient implementation of weighted eno schemes," *Journal of Computational Physics*, vol. 126, no. 1, pp. 202 – 228, 1996.

[115] A. Harten, P. D. Lax, and B. van Leer, "On upstream differencing and godunov-type schemes for hyperbolic conservation laws," *SIAM Review*, vol. 25, pp. 35–61, 1983.

[116] B. Einfeldt, "On godunov-type methods for gas dynamics," *SIAM Journal on Numerical Analysis*, vol. 25, pp. 294–318, 1988.

[117] K. Takami, L. Rezzolla, and L. Baiotti, "Spectral properties of the post-merger gravitational-wave signal from binary neutron stars," *Phys. Rev. D*, vol. 91, no. 6, p. 064001, 2015.

[118] T. Dietrich, N. Moldenhauer, N. K. Johnson-McDaniel, S. Bernuzzi, C. M. Markakis, B. Brügmann, and W. Tichy, "Binary Neutron Stars with Generic Spin, Eccentricity, Mass ratio, and Compactness - Quasi-equilibrium Sequences and First Evolutions," *Phys. Rev. D*, vol. 92, no. 12, p. 124007, 2015.

[119] A. Tsokaros, K. Uryū, and L. Rezzolla, "New code for quasiequilibrium initial data of binary neutron stars: Corotating, irrotational, and slowly spinning systems," *Phys. Rev. D*, vol. 91, no. 10, p. 104030, 2015.

[120] J. R. Wilson and G. J. Mathews, *Relativistic hydrodynamics.*, pp. 306–314. 1989.

[121] A. Nagar, J. A. Font, O. Zanotti, and R. De Pietri, "Gravitational waves from oscillating accretion tori: Comparison between different approaches," *Phys. Rev. D*, vol. 72, p. 024007, 2005.

[122] L. Baiotti, S. Bernuzzi, G. Corvino, R. De Pietri, and A. Nagar, "Gravitational-Wave Extraction from Neutron Stars Oscillations: Comparing linear and nonlinear techniques," *Phys. Rev. D*, vol. 79, p. 024002, 2009.

[123] F. J. Zerilli, "Effective potential for even parity Regge-Wheeler gravitational perturbation equations," *Phys. Rev. Lett.*, vol. 24, pp. 737–738, 1970.

[124] V. Moncrief, "Gravitational perturbations of spherically symmetric systems. I. The exterior problem.," *Annals Phys.*, vol. 88, pp. 323–342, 1974.

[125] N. T. Bishop and L. Rezzolla, "Extraction of Gravitational Waves in Numerical Relativity," *Living Rev. Rel.*, vol. 19, p. 2, 2016.

[126] M. Campanelli and C. O. Lousto, "Second order gauge invariant gravitational perturbations of a Kerr black hole," *Phys. Rev. D*, vol. 59, p. 124022, 1999.

[127] M. Campanelli, B. J. Kelly, and C. O. Lousto, "The Lazarus project. II. Space-like extraction with the quasi-Kinnersley tetrad," *Phys. Rev. D*, vol. 73, p. 064005, 2006.

[128] T. Damour, A. Nagar, M. Hannam, S. Husa, and B. Bruegmann, "Accurate Effective-One-Body waveforms of inspiralling and coalescing black-hole binaries," *Phys. Rev. D*, vol. 78, p. 044039, 2008.

[129] C. Reisswig and D. Pollney, "Notes on the integration of numerical relativity waveforms," *Class. Quant. Grav.*, vol. 28, p. 195015, 2011.

[130] K. Hotokezaka, K. Kyutoku, H. Okawa, and M. Shibata, "Exploring tidal effects of coalescing binary neutron stars in numerical relativity. II. Long-term simulations," *Phys. Rev. D*, vol. 91, no. 6, p. 064060, 2015.

[131] K. Hotokezaka, K. Kyutoku, Y.-i. Sekiguchi, and M. Shibata, "Measurability of the tidal deformability by gravitational waves from coalescing binary neutron stars," *Phys. Rev. D*, vol. 93, no. 6, p. 064082, 2016.

[132] T. Damour, A. Nagar, and L. Villain, "Measurability of the tidal polarizability of neutron stars in late-inspiral gravitational-wave signals," *Phys. Rev. D*, vol. 85, p. 123007, 2012.

[133] K. Kiuchi, P. Cerdá-Durán, K. Kyutoku, Y. Sekiguchi, and M. Shibata, "Efficient magnetic-field amplification due to the Kelvin-Helmholtz instability in binary neutron star mergers," *Phys. Rev. D*, vol. 92, no. 12, p. 124034, 2015.

[134] A. Drago, A. Lavagno, G. Pagliara, and D. Pigato, "Early appearance of Δ isobars in neutron stars," *Phys. Rev. C*, vol. 90, no. 6, p. 065809, 2014.

[135] G. Burgio, A. Drago, G. Pagliara, H.-J. Schulze, and J.-B. Wei, "Are Small Radii of Compact Stars Ruled out by GW170817/AT2017gfo?," *Astrophys. J.*, vol. 860, no. 2, p. 139, 2018.

[136] L. Rezzolla, L. Baiotti, B. Giacomazzo, D. Link, and J. A. Font, "Accurate evolutions of unequal-mass neutron-star binaries: properties of the torus and short GRB engines," *Class. Quant. Grav.*, vol. 27, p. 114105, 2010.

[137] S. Chandrasekhar, "Solutions of two problems in the theory of gravitational radiation," *Phys. Rev. Lett.*, vol. 24, pp. 611–615, 1970.

[138] J. Friedman and B. F. Schutz, "Secular instability of rotating Newtonian stars," *Astrophys. J.*, vol. 222, p. 281, 1978.

[139] A. L. Watts, N. Andersson, H. R. Beyer, and B. F. Schutz, "The oscillation and stability of differentially rotating spherical shells: the normal mode problem," *Mon. Not. Roy. Astron. Soc.*, vol. 342, p. 1156, 2003.

[140] A. Watts, N. Andersson, and D. Jones, "The nature of low T/—W— dynamical instabilities in differentially rotating stars," *Astrophys. J. Lett.*, vol. 618, p. L37, 2005.

[141] G. Corvino, L. Rezzolla, S. Bernuzzi, R. De Pietri, and B. Giacomazzo, "On the Shear Instability in Relativistic Neutron Stars," *Class. Quant. Grav.*, vol. 27, no. 11, p. 114104, 2010.

[142] M. Punturo *et al.*, "The Einstein Telescope: A third-generation gravitational wave observatory," *Class. Quant. Grav.*, vol. 27, p. 194002, 2010.

[143] B. P. Abbott *et al.*, "Exploring the Sensitivity of Next Generation Gravitational Wave Detectors," *Class. Quant. Grav.*, vol. 34, no. 4, p. 044001, 2017.

[144] W. Kastaun, R. Ciolfi, and B. Giacomazzo, "Structure of Stable Binary Neutron Star Merger Remnants: a Case Study," *Phys. Rev. D*, vol. 94, no. 4, p. 044060, 2016.

[145] M. Hanauske, K. Takami, L. Bovard, L. Rezzolla, J. A. Font, F. Galeazzi, and H. Stöcker, "Rotational properties of hypermassive neutron stars from binary mergers," *Phys. Rev. D*, vol. 96, no. 4, p. 043004, 2017.

[146] M. Shibata and K. Taniguchi, "Merger of binary neutron stars to a black hole: disk mass, short gamma-ray bursts, and quasinormal mode ringing," *Phys. Rev. D*, vol. 73, p. 064027, 2006.

[147] M. Shibata and K. Kiuchi, "Gravitational waves from remnant massive neutron stars of binary neutron star merger: Viscous hydrodynamics effects," *Phys. Rev. D*, vol. 95, no. 12, p. 123003, 2017.

[148] L. Baiotti, R. De Pietri, G. M. Manca, and L. Rezzolla, "Accurate simulations of the dynamical barmode instability in full General Relativity," *Phys. Rev. D*, vol. 75, p. 044023, 2007.

[149] R. De Pietri, A. Feo, L. Franci, and F. Löffler, "Neutron Star instabilities in full General Relativity using a $\Gamma = 2.75$ ideal fluid," *Phys. Rev. D*, vol. 90, no. 2, p. 024034, 2014.

[150] K. D. Kokkotas and B. G. Schmidt, "Quasinormal modes of stars and black holes," *Living Rev. Rel.*, vol. 2, p. 2, 1999.

[151] N. Stergioulas, T. A. Apostolatos, and J. A. Font, "Nonlinear pulsations in differentially rotating neutron stars: Mass - shedding - induced damping and splitting of the fundamental mode," *Mon. Not. Roy. Astron. Soc.*, vol. 352, p. 1089, 2004.

[152] K. H. Lockitch, J. L. Friedman, and N. Andersson, "The Rotational modes of relativistic stars: Numerical results," *Phys. Rev. D*, vol. 68, p. 124010, 2003.

[153] K.-K. Zhang and F. H. Busse, "On the onset of convection in rotating spherical shells," *Geophysical & Astrophysical Fluid Dynamics*, vol. 39, no. 3, pp. 119–147, 1987.

[154] M. J. Gutiérrez *et al.*, "The TRAPSENSOR Facility: an Open-Ring 7-Tesla Penning Trap for Laser-Based Precision Experiments," *New J. Phys.*, vol. 21, no. 2, p. 023023, 2019.

[155] F. H. BUSSE and R. SIMITEV, "Inertial convection in rotating fluid spheres," *Journal of Fluid Mechanics*, vol. 498, p. 23–30, 2004.

[156] K. Zhang and X. Liao, *Theory and Modeling of Rotating Fluids: Convection, Inertial Waves and Precession*. Cambridge Monographs on Mechanics, Cambridge University Press, 2017.

[157] I. Daubechies and T. Paul, "Time-frequency localisation operators-a geometric phase space approach: II. the use of dilations," *Inverse Problems*, vol. 4, pp. 661–680, aug 1988.

[158] S. C. Olhede and A. T. Walden, "Generalized morse wavelets," *IEEE Transactions on Signal Processing*, vol. 50, no. 11, pp. 2661–2670, 2002.

[159] J. M. Lilly and S. C. Olhede, "Higher-order properties of analytic wavelets," *IEEE Transactions on Signal Processing*, vol. 57, no. 1, pp. 146–160, 2009.

[160] S. Bose, K. Chakravarti, L. Rezzolla, B. S. Sathyaprakash, and K. Takami, "Neutron-star Radius from a Population of Binary Neutron Star Mergers," *Phys. Rev. Lett.*, vol. 120, no. 3, p. 031102, 2018.